RELATIONSHIP BETWEEN LIGHTNING FLASH RATES AND RADAR OBSERVATIONS FROM COLORADO AND AUSTRALIA

by

Jesse James Ryan

and

Steven A. Rutledge

Department of Atmospheric Science

Colorado State University

Fort Collins, CO 80523

Research Supported by

National Oceanic and Atmospheric Administration

under Grant NA76GP0370

Summer 1999

Atmospheric Science Paper No. 681

ABSTRACT

RELATIONSHIP BETWEEN LIGHTNING FLASH RATES AND RADAR OBSERVATIONS FROM COLORADO AND AUSTRALIA

Relationships between lightning flash rates and radar observations were examined for two regions; northeastern Colorado and Darwin, Australia. Five case studies from Colorado were analyzed using observational data from: the CSU-CHILL multiparameter radar, the ONERA VHF lightning interferometer, a field change meter and the National Lightning Detection Network. Three case studies from tropical Australia were analyzed using data from: the C-POL BMRC/NCAR multiparameter radar, a field change meter and an Advanced Lightning Detection Finder network. For each case, parameters such as peak echo height (H), storm area (A), and storm volume (V) were computed using different radar reflectivity and temperature thresholds. Storm areas and volumes were computed above the altitude of various temperature thresholds. Cloud echo-top height (H_0) was defined as the peak height using the 0 dBZ reflectivity threshold.

Correlations existed between H, A, and V, and the total lightning flash rate on a majority of the cases, and were strongest when higher reflectivity and colder temperature thresholds were used. An increased correlation between H, A, and V, and total flash rate for high reflectivity (> 20 dBZ) thresholds was noted for storms which contained broad areas of stratiform precipitation. Since stronger correlations were found between total flash rate and the product of A and V (AV) than between the total flash rate and H^5, this study suggests that significant error can be introduced by assuming that the horizontal scale of a thunderstorm charge generation is comparable to the vertical scale. In addition, we show that AV and H^5 at high reflectivities (> 20 dBZ) are both better correlated to total flash rate than H_0^5, a parameter commonly used as a predictor for lightning flash rates in modeling studies.

The ratio of intracloud (IC) to cloud-to-ground (CG) lightning was also analyzed for each case. This ratio was subsequently compared to cold cloud thickness (CCTh), defined as the distance

between cloud top and the environmental freezing level. The relationships between IC/CG ratio and CCTh were similar to prior research, except for storms with high (> 40) IC/CG ratios.

Jesse James Ryan
Department of Atmospheric Science
Colorado State University
Fort Collins, CO 80523
Spring 1999

ACKNOWLEDGEMENTS

I would like to thank my advisor Prof. Steven Rutledge for his excellent support. I would also like to thank my committee members Prof. Jeff Collet and Prof. R. Steve Robinson. In addition, I gratefully acknowledge the following persons for providing support, data sets, and/or assistance: Dr. James Dye (NCAR), Dr. Thomas Matejka (NOAA/NSSL), Martin Venticinque (NCAR), Jody Williams (NCAR), Jennifer Williams, Dr. Pierre Laroche (ONERA), and Eric Defer (ONERA). A cheerful thanks to those from the Australian BMRC: Dr. Tom Keenan, Ken Glasson, Ross Christmas, Jim Core and Peter Powers. I would also like to thank the CSU-CHILL radar staff for their assistance during and after the STERAO-A project. I also thank all of those in the Radar Meteorology Group for their support and assistance.

This research was supported by the National Oceanic and Atmospheric Administration, under Grant NA76GP0370.

TABLE OF CONTENTS

LIST OF TABLES

Table Caption Page

LIST OF FIGURES

CHAPTER 1

INTRODUCTION

1.1 Background motivation

Among the tropospheric sources of nitrogen oxides, the estimate of the fixation of molecular nitrogen by lightning is far from certain. The other emission sources of nitrogen oxides to the troposphere include fossil fuel combustion (including aircraft emissions), biomass burning, stratospheric mixing and soil microbial emissions (see Table 1.1). The estimates of lightning fixation of nitrogen range from 2 to 200 Tg yr^{-1} (e.g. Lawrence et al., 1995, Liaw et al., 1990), although the average estimates fall between 5 and 25 Tg yr^{-1} (Levy et al., 1996, Price and Penner, 1997b, Wang et al., 1998).

Table 1.1 Estimates of NO_x Emissions from Various Sources

Source Type	Source Amount (Tg yr-1)	Source Uncertainty (%)
Fossil Fuel Combustion	22[ab]	33%[ab]
Biomass Burning	6[ab]	200%[ab]
Soil Emissions	6[ab]	100%[ab]
Lightning	8[cd]	200+%[cd]
Other Source	4[ab]	50%[ab]
Total Sources	46	95+%

[a] Penner et al. 1991; [b] Logan 1983; [c] Lawrence et al. 1995; [d] Price and Penner 1997b

Nitrogen oxides in the troposphere react in the basic photochemical cycle (see Table 1.2) with ozone and OH radicals. In low NO_x environments, ozone is destroyed; conversely, in high NO_x environments, the greenhouse-gas ozone is produced.

Table 1.2 NO_x in the Basic Photochemical Cycle

High NO_x regime	**Low NO_x Regime**
$NO_2 + h\nu \rightarrow O + NO$	$HO_2\cdot + O_3 \rightarrow OH\cdot + 2O_2$
$O + O_2 + M \rightarrow O_3 + M$	$OH\cdot + CO \rightarrow H\cdot + CO_2$
$OH\cdot + CO \rightarrow H\cdot + CO_2$	$H\cdot + O_2 + M \rightarrow HO_2\cdot + M$
$H\cdot + O_2 + M \rightarrow HO2\cdot + M$	
$HO_2\cdot + NO \rightarrow OH\cdot + NO_2$	
NET: $CO + 2O_2 + h\nu \rightarrow CO_2 + O_3$	NET: $CO + O_3 \rightarrow CO_2 + O_2$

A possible positive feedback to global warming is the production of ozone from an increase in global lightning (Sinha and Toumi, 1997). In addition to links to climate change, NO_x plays an important role in the oxidizing capacity of the troposphere. The capacity to break down Volatile Organic Carbon species (VOC) and CO depends indirectly on nitrogen oxide concentrations. Due to the short lifetime of the NO_x species, its concentration can have wide spatial and temporal variations depending upon its sources. Since the lightning source of NO_x (LNO_x) has such a wide spatial and temporal variations (e.g. Orville and Spencer, 1979), understanding its effect is complicated. Thus, a strong understanding of the sources of NO_x is essential to correctly assessing the resulting chemistry. Since LNO_x is emitted directly into the free troposphere, LNO_x contributes more NO_x to the budget of the free troposphere than a source of the same magnitude emitted within the boundary layer. We define the efficiency of a NO_x source as its contribution to the concentration in the free troposphere divided by the source strength. Thus, LNO_x has a higher efficiency than the boundary layer sources.

Various methods have been used to estimate the global budget of NO_x produced by lightning (Tuck, 1976; Lawrence, 1995; Ridley, 1996; Price and Penner, 1996; Wang et al., 1996). Most of these methods rely on estimates of the following parameters: (1) global flash frequency (e.g. Orville and Spencer 1979; Orville and Henderson 1986), (2) intra-cloud (IC) vs. Cloud-to-Ground (CG) flash ratio (Price and Rind, 1993), and (3) NO_x production rates for IC and CG flashes (see Lawrence et al., 1995). These global parameters have significant uncertainties. The production rate for NO_x per lightning flash has been estimated from laboratory, theoretical and field studies (see Lawrence et al., 1995 for a review). Another factor to be considered is the height of the lightning source in the free troposphere.

Initial results from a modeling study, which varied the height profile of the NO_x injection and compared these results to observations, suggest that the IC production efficiency and the height profile of NOx injection used in previous research is lower than necessary to match observations (K. Pickering, personal communication, 1998). The source height influences the lifetime of the NO_x and further chemical interactions. Finally, we must consider the mixing and transport of NO_x by convective circulations. Global and regional dynamic models, coupled with chemical models and simple parameterizations (e.g., Price and Rind, 1992, PR92 hereafter) for the flash rate given the grid inferred convective cloud height, have shown that the LNO_x source has a dominant effect in the role of NO_x in the free troposphere (e.g., Kraus et al., 1996; Kasibhatla et al., 1993; Levy et al., 1996; Pickering et al., 1998). This effect holds especially true in remote regions downwind of major continental lightning sources, as verified by measurements from PEM-West B (Kawakami et al., 1997). Prior studies, dynamic modeling coupled with chemical models, use PR92 to address the global flash frequency and use estimates for IC to CG ratio and IC and CG NO_x production rates. We will further investigate global flash frequency and the IC to CG ratio.

To understand the global distribution of lightning, we must consider the electrification process within convection. The basic steps leading to lightning are the separation of charge, transport of the charge to different regions within the thunderstorm and, finally, the breakdown process that occurs between the charge centers. Current research (e.g. Carey and Rutledge, 1994; Carey and Rutledge, 1998; Lang, 1997; Dye et al., 1989; Williams, 1985) suggests that an initial generation of charge within thunderstorms, prior to generation of significant charge and the resulting electric fields, can be explained through the non-inductive charging theory (Takahashi, 1978; Saunders et al., 1991; Saunders, 1993).

The non-inductive charging theory (NIC) requires three types of particles: supercooled cloud droplets, small ice crystals and precipitation-sized (>1mm) ice particles. The precipitation-sized ice particles are typically graupel particles or frozen raindrops. Charge generation has been studied in numerous laboratory studies. These studies indicate that charges of opposite signs are separated when precipitation-sized ice particles undergo rebounding collisions with small ice crystals in the presence of supercooled water droplets. These dissimilar-sized ice particles separate under the influence of gravity.

The sign of the charge on the rebounding particles depends on several parameters, including the liquid water content, temperature, and size of the small ice crystals (Saunders et al., 1991).

The laboratory studies illustrated that for typical conditions in thunderstorms the precipitation-sized ice particle acquires a negative charge above a charge reversal level and a positive charge below this level. Such a reversal occurs between -10°C and -20°C for the liquid water contents and temperatures found in thunderstorms. The NIC theory is consistent with the simple tripole charge structure model of a thunderstorm. This conceptual model consists of a disperse upper region of positive charge, a lower region of negative charge generally confined in the -20°C to 0°C level, and a lower region of positive charge. Finally, lightning occurs when the electric field between the charge regions exceeds a critical breakdown strength. Lightning can occur as an intra-cloud flash between the upper positive and lower negative regions. Additionally, the lower positive region can cause the initial breakdown to occur downward and result in a cloud-to-ground flash (CG) (MacGorman and Rust, 1997).

Due to the strict microphysical requirements for significant cloud electrification, its onset typically occurs when supercooled liquid water and ice hydrometeors are lofted above the -10°C level in convective updrafts (Workman and Reynolds 1949; Dye et al. 1989; Carey and Rutledge 1994; Carey and Rutledge 1998; Peterson et al. 1989). Thus, a correlation can be drawn between stronger updraft velocities and higher electrical discharge rates. Price and Rind (1992) (PR92) parameterize continental lightning flash rates as proportional to cloud top height raised to the fifth power. Their parameterization is based on empirical and theoretical arguments. PR92 employed a different parameterization for the lower flash rate of oceanic convection. The oceanic parameterization is empirically based on the weaker updraft velocities which occur in oceanic convection. These simple parameterizations developed by PR92 have been used in modeling seasonal time scale lightning flash rates in both regional and global scale models.

The limitations for the spatial and temporal scales which apply to the PR92 parameterizations are uncertain. A modeling study with one-hour temporal resolution showed that episodic emissions, as opposed to constant lightning emissions, have a significant impact on the LNO_x distribution and resulting chemical impact (Flatøy and Hov 1997). The PR92 parameterization of the continental flash rate was based on

empirical results collected in the United States (Williams, 1985). Significant variations may occur regionally (Price and Rind, 1992). A study of the relationship between cloud top height, established via CAPE, and total flash rate in the French Guyana coast was found to be situated between PR92's continental and maritime regimes (Molinié and Pontikis, 1995). This relationship reveals that the PR92 parameterizations may be inappropriate in coastal regions. Another drawback to the PR92 parameterizations is the indirect nature of the relationship between cloud top height and the microphysics involved in thunderstorm charge generation. It is possible to have storms with similar cloud top heights and very different microphysical properties within the region responsible for charge separation (Petersen, et al., 1996). This occurrence leads to variations between the total flash rate in storms with the same cloud top height.

When modeling the LNOx impact, we must also make assumptions about the IC/CG ratio (e.g. Price and Rind, 1993), which has been shown to vary with latitude (Pierce, 1970; Prentice and Mackerras, 1977). Since energy released in IC flashes is thought to be lower than in CG flashes they are thought to produce less NO_x per flash, thus variations in the IC/CG ratio effect modeling estimates of the LNO_x source.

Other storm parameters in addition to cloud top height have been correlated to lightning activity, such as rainfall (Buechler et al. 1990; Petersen and Rutledge, 1998) and the area of radar reflectivity (Marshall and Radhakant, 1978). Recently, Solomon and Baker (1998), using a method from Helsdon et al. (1992), modeled various types of convection. Interestingly, they found a dependence of the total flash rate on the cloud condensation nuclei concentration and a strong dependence on the updraft speed and liquid water fraction within the charging layer. The charging layer is defined as the zone in which ice crystals, graupel particles and supercooled water coexist. This collection of prior works suggest that parameters other than the cloud top height could be used to estimate the total flash rate in thunderstorms.

1.2 Scientific Objectives

The primary scientific objective of this work is to determine if more effective predictors of lightning flash-rate other than cloud top height can be identified. To find such predictors, we will examine trends between radar-derived storm parameters and lightning flash-rates. The radar parameters we will analyze include the cloud top height, as determined by the 0 dBZ radar reflectivity level; maxima in height at other reflectivity levels; area, defined as an area exceeding a reflectivity threshold at the level of a specific temperature threshold; and volume, defined as volume exceeding a reflectivity threshold above a specific temperature threshold. The analysis will include investigation of radar-derived parameters on the same scale as the PR92 parameterization (length raised to the fifth power). Furthermore, this research will investigate the relationship between the above radar characteristics and the IC to CG flash ratio. As a related objective, we will examine the different trends between storm strength (via radar parameters and CAPE), storm organization and lightning regimes.

1.3 Organization of the thesis

After this introductory chapter, Chapter 2 addresses the instrumentation and data sets used in the work, as well as the methodology used to interpret the data. Chapter 3 presents five mid-latitude continental case studies in northeastern Colorado. Chapter 4 details three tropical case studies from the Darwin, Australia area; one coastal case and two island cases. Chapter 5 presents conclusions of the research and recommendations for future investigation.

CHAPTER 2

INSTRUMENTATION AND METHODOLOGY

This chapter describes the observational platforms used in this research and the methodology used in the analysis of the data from these platforms. The chapter is broken into seven sections which cover the following subjects: the Colorado State University, University of Chicago and University of Illinois (CSU-CHILL) radar; the Bureau of Meteorology Research Centre (BMRC) and National Center for Atmospheric Research (NCAR) C-POL radar; radar data methodology; the Office National d"Etudes de Recherches Aerospatiales (ONERA) VHF lightning interferometer (ITF); flat plate antennas, also known as field change meters (FCM); the National Lightning Detection Network (NLDN); and the Maritime Continent Thunderstorm Experiment (MCTEX) Advanced Lightning Direction Finding (ALDF) network.

2.1 CSU-CHILL multiparameter Doppler radar

The CSU-CHILL radar is an S-band dual, linearly polarized, Doppler radar. The operational details of the radar are listed in Table 2.1. During the Stratosphere-Troposphere Experiments: Radiation, Aerosols, and Ozone-A (STERAO-A) project, the scanning strategy included plan-position indicator (PPI) sector scans, full storm volume scanning, good temporal resolution (typically less than or equal to 6 minutes per volume), and less than 1 degree of separation between elevation angles. At times, especially when the storms were in close proximity to the radar, sacrifices in spatial resolution had to be made to ensure good temporal resolution. At these times, the sacrifice was made to decrease elevation resolution in order to scan to the top of the storms close to the radar. This issue's effect on the data analysis is discussed in section 2.3 and in Chapter 3 for the cases in question. A second radar scanning strategy for another project was used at

times during the 12 July 1996 case, which resulted in reduced temporal resolution during one time period. Figure 2.1 shows the STERAO-A operational area and the location of the CSU-CHILL radar.

Table 2.1 Operational Characteristics of CSU-CHILL During STERAO-A

CSU-CHILL radar characteristic	Value during STERAO-A
Wavelength (cm)	11
Polarization	Linear: H and V
Antenna diameter (m)	8.5
3 dB beamwidth (°)	1.0
Sidelobe level (dB)	< -27
Integrated cross-polarization isolation (dB)	< .32
Peak power (kW)	800
(Pulse length)/2 (h/2, m)	150
Pulse repetition frequency (Hz)	1000
Pulse per integration	128
Receiver noise power (dBm)	-115
Maximum Range (km)	150

Variables measured by the radar include horizontal reflectivity (Z_h), radial velocity (V_r), differential reflectivity (Z_{dr}), linear depolarization ratio(L_{dr}), correlation coefficient at zero lag (ρ_{hv}), and total differential phase (Ψ_{dp}). In this research only the Z_h, V_r, and ρ_{hv} variables were used for the CSU-CHILL data set. The horizontal reflectivity (Z_h) is a measure of the total returned power in the radar volume using horizontal polarization. In the Rayleigh regime, for spherical particles much smaller than the incident radiation ($r < 0.07\ \lambda$), Z_h is a function of the sixth power of the particle diameter. Thus, the largest particles have the strongest effect on reflectivity. Radial velocity (V_r) is the reflectivity weighted average of the particle velocities in the direction of the radar beam, either toward or away from the radar. For a complete discussion of Doppler methods for deriving radial velocity, see Doviak and Zrnic (1993). The correlation coefficient at zero lag (ρ_{hv}) is the statistical correlation between the horizontal and vertical polarized returns. The variable ρ_{hv} is a function of size, canting angle and shape of the hydrometeors. This variable is > 0.97 in areas of rain and falls off in regions of mixed phase precipitation.

Secondary lobes in the transmitted beam of the CSU-CHILL radar are extremely small, but for reflectivity cores > 50 dBZ, significant returns from these lobes can occur. These echoes can be distinguished from other high elevation angle echoes by their low ρ_{hv} and symmetrical patterns of

reflectivity and radial velocity. Thus, we used these radar variables when editing the radar data for the occurrence of sidelobe echoes.

The National Center for Atmospheric Research's (NCAR) software Research Data Support System (RDSS) (Carbone and Oye, 1981) was used to edit the radar data in this study. Thresholding on $Z_h < 0$ dBZ and $\rho_{hv} < 0.7$ was performed to remove ground clutter and echoes associated with anomalous propagation. For light rain situations Z_h is used as a proxy for rain-rate where Z_h of 0 dBZ is equivalent to a rain-rate less than 1mm hr^{-1}(Jones, 1955). Echoes associated with radar sidelobes were manually removed using Z_h, V_r and ρ_{hv}. The sidelobe echoes were encountered at high elevation angles where the unaffected V_r field rarely deviated from the environmental flow. The sidelobe echo was identified by a butterfly-shaped V_r field, which deviated substantially from the unaffected echo and low values of ρ_{hv}.

The edited reflectivity field was interpolated to a cartesian grid using the REORDER software package, also developed by NCAR. The Cressman filtering scheme was used to assign data to the cartesian grid (Cressman, 1959), with a variable radius of influence. The azimuthal spacing was set at 1 degree, equivalent to the CSU-CHILL 3 dB antenna beamwidth. The grid resolution was 1.0 km horizontally and 0.5 km vertically.

2.2 C-POL multiparamter Doppler radar

The C-POL radar is a dual, linear polarized, C-Band Doppler radar. The operational characteristics of this radar are listed in Table 2.2 (see Keenan et al., 1998). The scanning strategy during MCTEX was similar to that in STERAO-A, with some exceptions. At times, especially on 27 November 1995 (27Nov), additional low level scans over a rain gauge network were interspersed with the sector volume scans of the storm. Non-polarimetric scans, not used for this work, were also taken during portions of the MCTEX cases (27 and 23 November). These exceptions degrade the temporal resolution of the cases selected for this study. The field project in Darwin, for the 29 January 1998 case, involved 360° volume scans every ten minutes. Though this resolution is not nearly sufficient to study convective dynamics, it is

sufficient to study the bulk microphysical trends identified by the radar variables. Figure 2.2 shows the MCTEX operational area and the location of the CPOL radar.

Table 2.2 Characteristics of the C-POL radar during MCTEX and Darwin field projects

C-POL radar characteristic	Value
Wavelength (cm)	5.5
Polarization	Linear: H and V
Antenna diameter (m)	4.2
3 dB beamwidth (°)	1.0
Sidelobe level (dB)	< -27
Integrated cross-polarization isolation (dB)	< -35
Peak power (kW)	250
Pulse repetition frequency (Hz)	1000
Receiver noise power (dBm)	-115
Maximum Range (km)	150

Variables measured by the CPOL radar include horizontal reflectivity (Z_h), radial velocity (V_r), differential reflectivity (Z_{dr}), linear depolarization ratio (L_{dr}), correlation coefficient at zero lag (ρ_{hv}), and total differential phase shift (Ψ_{dp}). For this work, in addition to Z_h, V_r and ρ_{hv} (see Section 2.1 for descriptions), the differential phase shift was used to correct for significant attenuation that occurs in Z_h at C-Band (5.5 cm) wavelengths. The total differential phase is the cumulative sum of phase shift over all radar data bins up to the current bin. The two factors that contribute to the total two-way differential phase shift(Ψ_{dp}) are the propagation differential phase shift (ϕ_{dp}) and the backscatter differential phase shift (δ).

The propagation differential phase shift(ϕ_{dp}) occurs due to propagation through an ansiotropic

$$\Psi_{dp} = \phi_{dp} + \delta \qquad (2.1)$$

medium, such as oblate raindrops. The backscatter phase shift (δ) occurs due to interaction with particles large enough to cause non-Rayleigh scattering, such as hail, and appears in the total differential phase(Ψ_{dp}) as a noisy signal over the propagation differential phase (ϕ_{dp}). The variable ϕ_{dp} is obtained by smoothing Ψ_{dp} (see Hubbert et al., 1993).

The editing software, RDSS, developed by NCAR was used after conversion from the LASSEN format, which C-POL data were recorded in. After using similar thresholding on Z_h and ρ_{hv} as with the

CSU-CHILL cases, the variable Ψ_{dp} is unfolded. Typically, C-POL has a range of -32° to 32° for Ψ_{dp} before unfolding. Fortunately, no sidelobes were apparent when the C-POL data were inspected. Next, the data was processed by filtering Ψ_{dp}, as described previously, to obtain ϕ_{dp}. The data was processed with REORDER software onto cartesian grids, as with the CSU-CHILL data except for the inclusion of the multiparameter variables to be used for the next step of attenuation correction.

Attenuation of a C-Band radar can be significant, especially in high reflectivity cores (see Keenan et al., 1998). Attenuation was corrected following the method described by Ryzhkov and Zrnic (1995). They demonstrate how the bias in reflectivity (ΔZ_h) is linearly related to the propagation differential phase (ϕ_{dp}). In their method, the variables ΔZ_h and ϕ_{dp} are plotted for each radar volume over all radar data bins dropping statistical anomalies. The resulting linear regression allows for a linear correction of Z_h for a given ϕ_{dp}, over all gates in the radar volume. This regression and correction on Z_h was applied for all volumes which resulted in a positive correction coefficient, a ρ_{hv} higher than 0.25 and a regression containing at least 100 significant data points. When these conditions were not met, average values for the correction equation were used as determined by previous work on the MCTEX cases (personal communication, D. Ahijevych, 1998).

2.3 Radar height methodology

The three-dimensional cartesian grid of radar reflectivity was converted to a two-dimensional grid of highest height for a given threshold of reflectivity. The radar data was spatially filtered to a range

from a point in space associated with the strongest reflectivity cores (only for the STERAO-A cases). See Table 2.3 for values of this range threshold.

Table 2.3 Values of CSU-CHILL and NLDN range filtering

Date of STERAO-A Case	Range (km)
July 9, 1996	60
July 10, 1996	40
July 12, 1996	50
July 30, 1996	60
August 9, 1996	50

The two-dimensional height grids were inspected for cases where the radar data was missing, where the top the entire height of the storm was not completely scanned. A few radar volumes had an insignificant amount of data missing in this way, while several radar volumes had to be dropped from the analysis. Dropping data decreased the temporal resolution, but never created a resolution of less than 10 minutes. Sounding data during the field projects was used to establish the height of particular temperature levels. FORTRAN programs calculated three variables from the radar two-dimensional height grids: the peak height, the area of the height field above the temperature level, and the volume bounded by both the temperature level and the height field.

2.4 ONERA VHF lightning interferometer

During STERAO-A, ONERA operated a two station radio interferometry system to map VHF emissions from lightning. This discussion of their system is based on Lang (1997), which was developed from Mazur et al. (1997), Laroche et al. (1994), and communications between Lang and ONERA researchers. The principal behind this lightning mapping technique is conversion of the difference in arrival times of the radiation into a differential phase. This phase is then used to calculate the angle to the radiation source. With two stations, except along the baseline between the stations, the horizontal position of the radiation source can be determined. Ambiguities in the arrival angle are resolved by measuring the baseline in wavelengths. The ONERA ITF consisted of two receiving stations, each with antennas to measure the

azimuthal angle. One station had an additional antenna to measure the elevation angle to the source radiation. The operational details of the ONERA ITF are listed in Table 2.4.

Table 2.4 ONERA ITF operational characteristics

ITF characteristic	Value
Frequency Bandwidth (MHz)	110-118
Bandwidth (MHz)	1
Time Resolution (μs)	23
Azimuthal Resolution (°)	0.5
Elevational Resolution (°)	0.25

The ONERA ITF stations used during the STERAO-A project were oriented approximately northwest to southeast with a baseline of about 40 km. The northern station had an elevation sensor in addition to an azimuthal sensor. Spatial resolution between 1 and 2 km is obtained in the high resolution lobes to a distance of 50 km to the east and west of the baseline (see Figure 2.1 for a diagram of these lobes during STERAO-A). The best cases occurred when the storm was located within one of these lobes. Several of the cases studied in this thesis have time periods when calculated flash rates are unknown because the storms cross the baseline between the sensors.

Discharges that the ITF identifies include the recoil streamer, the negative leader and the spider discharge (see Uman, 1987, for a review of types of lightning discharges). Intra-cloud lightning is typically associated with recoil streamers and spider discharges. Cloud-to-ground (CG) lightning of the negative polarity is typically associated with negative leaders. The processes associated with positive CG lightning do not radiate significantly in the ITF's bandwidth (110-118 MHz). ONERA's software, Analyse, was used to classify the radiation localizations into bursts, which were further grouped into flashes based on the criteria in Table 2.5. Further processing of the data to correct errors in the ONERA Analyse software was accomplished by using software developed by NCAR's Jim Dye and Martin Venticique. Finally, the data was spatially filtered in the same way as the radar height data. Note that the resulting data represents the total flash rate of the storms minus the flash rate due to positive CG's.

Table 2.5 ONERA ITF flash grouping criteria

ITF criteria	Value
Maximum burst velocity (ms^{-1})	1.0×10^8
Minimum duration of leader/spider discharge (μs)	800
Minimum altitude of leader (m) –above which it is a spider discharge	1.5×10^3
Maximum number of sampling periods (23 μs) between two successive points in a burst	10
Maximum duration of a flash (μs)	1.0×10^6
Maximum distance between two bursts within a flash (m)	2.5×10^4
Maximum time between two bursts within a flash (μs)	250

2.5 Field Change Meters and Visual Observations

Field change meters (FCM), also known as flat plate antennae, were used during both MCTEX and STERAO-A to estimate the total flash rate. The FCM used in MCTEX was located at the C-POL radar site. In STERAO-A, the FCM was located at a position located 55° in direction and 33.4 km from the CSU-CHILL radar on 9 August 1996. This instrument is identical to that used by Carey and Rutledge (1996, 1998) as well as by Lang (1997). Thus, the following description is based on their work.

An FCM measures the electrostatic field charge associated with both IC and CG lightning (Uman, 1987), and the data from the sensor can be used to estimate the total flash rate. The sensor consists of a disk shaped conductor with its long axis parallel to the ground, housed in a metal canister containing the associated electronics. The canister is mounted on a stand with the FCM conductor facing the ground to reduce the precipitation contamination of the signal. Changes in the ambient electrostatic field result in a change in voltage across the conductor. The time constant of the device was set at 30 ms for both MCTEX and STERAO-A. This time constant allows for the detection of an IC or CG signal, yet allows the signal to return to zero between flashes. Voltage and time data were sampled at approximately 1 kHz. The instrument is not calibrated, so voltage can only be used to qualitatively estimate the electrostatic field change.

The detection range of the instrument falls approximately between 35 and 40 km (Carey, 1996; Lang, 1997). The detection efficiency of the instrument is not well known, but is probably a function of signal strength and range to flash (Lang, 1997). The data were processed with a weighted running mean filter designed to remove a known source of 60 Hz noise. Lightning flashes were then counted by

comparing signal amplitudes to the noise amplitude and counting flashes for those signals exceeding 1.8 times the signal-to-noise ratio. The counting algorithm accounted for the occurrence of return strokes by only counting another flash after 500 ms. Due to the problems with the detection efficiency and nature of the counting algorithm, the FCM's are only used as a general estimate to the total flash rate in this work. In addition, much of the trend in the data is expected to be a result of the storm's movement into and out of the FCM's relatively small range compared to storm size.

During the January-February of 1998 field experiment in Darwin, visual observations of low to null flash rates were observed in several cases. The lack of visible lightning during the night indicates a lightning flash-rate of zero to a range of approximately 40 km. This rate was used to quantify the lightning characteristics for the 29 January 1998 case.

2.6 National Lightning Detection Network

The NLDN is a network of magnetic direction finder sensors and time-of-arrival sensors over the contiguous United States. The NLDN accurately reports the horizontal position, time, multiplicity, polarity and peak current of those CG flashes it detects. The recent upgrade of the network is described in Cummins et al. (1998). The authors report an improved detection efficiency in the STERAO-A project domain of 90% or higher, with a median location accuracy of 0.5 km. The upgrade resulted in an anomalous population of small peak current positive CG's. These flashes are recognized by Cummins et al. (1996) as IC discharges incorrectly identified as positive CG's. The data was filtered as recommended by Cummins et al. (1998) removing positive flashes less than 10 kA. The data was filtered spatially in the same fashion as the radar height data.

2.7 MCTEX ALDF

During the MCTEX field project, four Advanced Lightning Direction Finder (ALDF) antennae were used (see Table 2.6) to measure CG lightning. These stations were provided by NASA/MSFC. Time-of-arrival techniques were used to translate the individual station's data CG flash data (personal communication J. Bailey, 1997; Uman, 1987). The data were comprised of solutions for the CG's position and polarity (as indicated by the nearest stations' magnetic field strength). The data were spatially filtered to the position and approximate range of the FCM located at the C-POL radar site.

Table 2.6 ALDF Network Locations

Location Name	**Longitude and Latitude, Degrees**
Coastal Plains	131.31332, -12.57833
Jabiru	132.89459, -23.66167
Douglas Daly	131.19839, -13.83398
Nguiu	130.61627, -11.76379

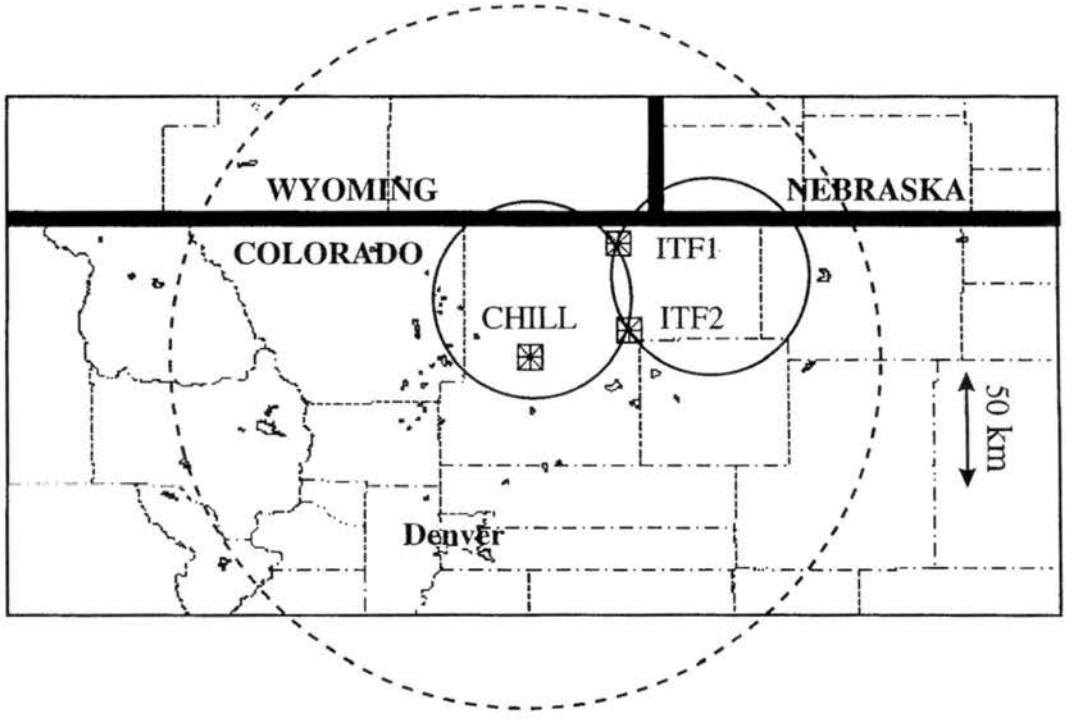

Fig. 2.1 Schematic map of STERAO-A operational area, including state boundaries (bold lines) and county boundaries (dashed lines). ITF1 and ITF2 indicate locations of ITF antenna. Best resolution ITF lobes indicated by solid circles. CHILL indicates location of CSU-CHILL radar. Dashed circle indicates operational range of CSU-CHILL radar (150 km).

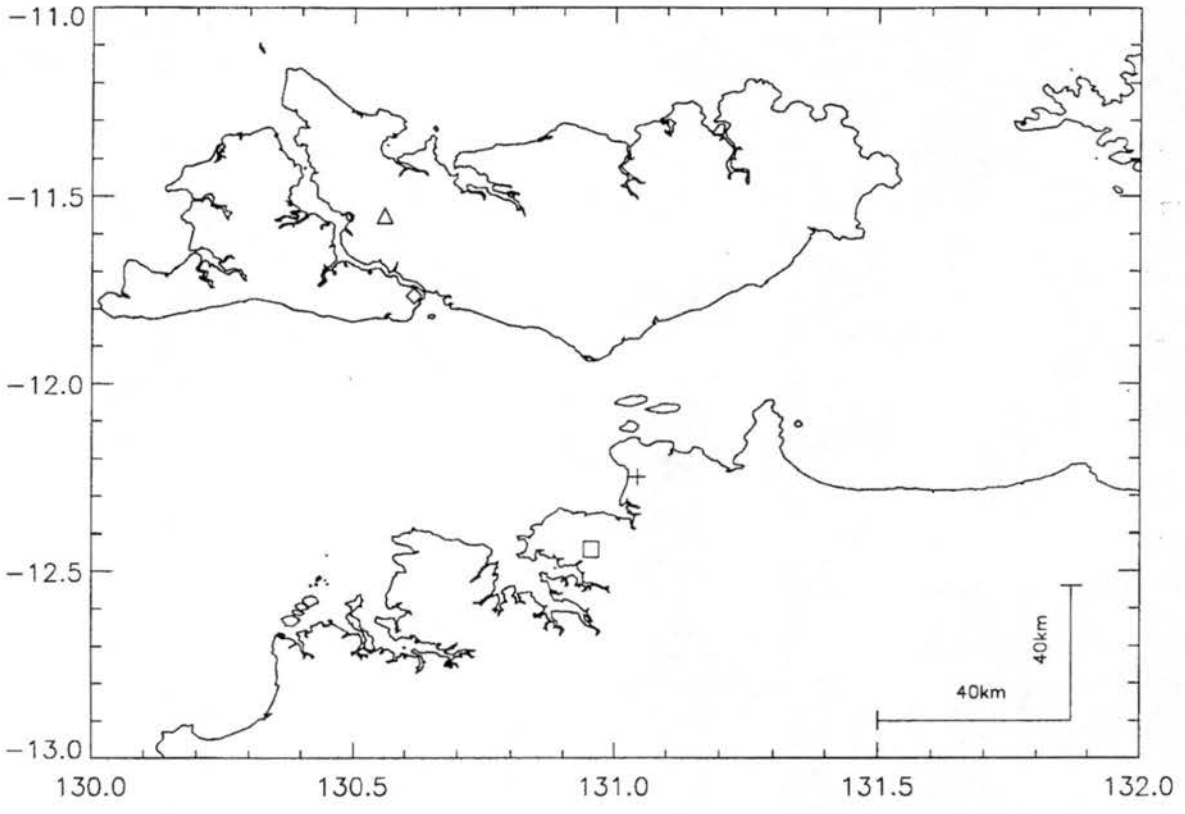

Figure 2.2 Schematic map of MCTEX and Darwin January-February 1998 operational area. Latitude on ordinate and longitude of abscissa Triangle indicates location of MCTEX sounding locations. Diamond indicates location of CPOL during the MCTEX project (as well as location of FCM). Plus (+) indicates location of CPOL during January-February 1998. Square indicates location of lightning observations during January-February 1998.

CHAPTER 3

MID-LATITUDE CASES FROM NORTHEAST COLORADO

In this chapter we present case studies for five storms in NE Colorado, identifying their radar and lightning characteristics. The storms span a range of lightning activity and storm intensity. The first two case studies include sensitivity tests to establish the best values for temperature and reflectivity parameters for attaining the highest correlations between the radar parameters and lightning observations.

3.1 July 10, 1996

The storm on July 10, 1996 (J10) is described in detail in Lang (1997). This storm initially formed in southwest Nebraska before propagating into the research area in northeast Colorado. Figure 3.1 illustrates the CLASS sounding launched from Fort Morgan airport at 1450 MDT, approximately 7 hours before the four hour period of appropriate lightning and radar data for this case. This sounding was approximately 90 km south of the initial convection. The CAPE was 792 J kg^{-1}, the shear 14.4 ms^{-1} (over the lowest 6 km), the lifted index -2.8°C, and the Bulk Richardson Number 7.7. The sounding certainly does not represent the conditions under which the convection formed. Additionally, this sounding may not accurately represent the conditions appropriate for the mature phase of this case. It is, however, the nearest sounding both in space and time to this storm.

The organizational characteristics, as indicated from radar reflectivity, showed a strong transition around 01 UTC. (See Fig. 3.2 for 1.5 km height horizontal cross sections of reflectivity and Fig. 3.3 for 9 km height horizontal cross sections of reflectivity.) As the storm moved into the instrument network, the storm was multicellular. At 23 UTC, the storm had two reflectivity cores separated by approximately 15 km. One core exceeded 40 dBZ and the other exceeded 50 dBZ. An upper level anvil stretched to the east

and southeast. At 00 UTC, the storm complex consisted of three reflectivity cores in excess of 40 dBZ aligned west-northwest to east-southeast. Around 01 UTC (Fig. 3.2f), a single reflectivity cell dominated and continued to dominate through 02 UTC (Fig. 3.2h). Many supercell characteristics were present during the last stages of the storm, being single-cellular and having a Weak Echo Region (WER), mid-level rotation, and higher IC flash rates; but the lack of consistent storm intensity and steadiness led Lang (1997) to identify this stage of the storm as "quasi-supercellular."

The parameterization of flash rates by cloud height, as described by PR92, was established using data consisting of 28 convective events. This correlation between total flash rate and cloud top height applies to the maximum observed flash rate and the maximum cloud top height observed. Arguments by Price and Rind (1992) also suggest total flash rate and maximum updraft velocity are proportional. Some storms exhibit brief periods of intense updrafts leading to brief increases in total flash rate followed by periods of reduced flash rates, while others exhibit a more steady production of lightning flashes. Under the former case, one would expect the flash rate to follow the cloud top height under short time scales until the maximum height and storm intensity is reached. After this point, the water and ice masses aloft would be expected to persist long after charge separation ceases or diminishes in a decaying storm. As shown in the cases below, for some storms, radar derived variables correlate to some extent on the time scale of radar volumes—6 to 10 minutes—while other storms demonstrate no such correlation. The J10 storm exhibited a correlation between radar derived variables and total flash rates but, not suprisingly, this correlation underwent a transition along with the storm transition associated with evolving reflectivity patterns.

Figure 3.4 (a-e) shows five time series plots of peak height, area, volume and five minute averaged total flash rate—with the radar variables calculated using reflectivity thresholds of 0, 10, 20, 30 and 40 dBZ and a temperature threshold of -10°C. For example, the 20 dBZ radar volume is the volume of radar echo > 20 dBZ at the -10°C level. The peak height in each time series shows little variability, especially at lower reflectivity thresholds. If we examine the variation of the volume, and to a lesser extent the peak height, as the reflectivity threshold increases, we see an increased dynamic range in the variation of these variables. For example, for the volume at 30 dBZ (see Figure 3.4d), we see pronounced peaks and troughs not present

in the volume at 0 dBZ (see Figure 3.4a). In addition, the trend of the volume variable follows the total flash rate closely from 2229 UTC through about 0100 UTC. At this point, which coincides to the transition from multi-cellular to single-cellular structure, a different trend emerges between these variables.

After the transition, the changes in flash-rate are followed by smaller variations in the radar variables than before the transition. Linear regressions between the radar derived variables and the total flash rate were performed, and the resulting correlation coefficients were calculated. The calculations cover three different time scales: the entire storm, the period prior to transition and the period after transition. An example of one of these regressions is shown in Figure 3.5, illustrating the regression for the 20 dBZ threshold. A second set of regressions was performed between the radar variables and the total flash rate lagged by one radar volume. This time period varied over the storm, but averaged 5.5 minutes. Table 3.1 lists the correlation coefficients for the three radar derived variables over each regression. Table 3.1 includes both the non-lagged and lagged sets of regressions. Note that the coefficients in this table correspond to the trend between radar variables and total flash rate plotted in Figure 3.4 (a-e).

Table 3.1 Correlation Coefficients for July 10, 1996: Radar Variables vs. Total Flash Rate using -10°C temperature cutoff while varying the reflectivity threshold

Time Series	dBZ Threshold	R^2 for Peak Height--Normal	R^2 for Area--Normal	R^2 for Volume--Normal	R^2 for Peak Height--Lagged	R^2 for Area--Lagged	R^2 for Volume--Lagged
Entire	0	0.0002	0.47	0.46	0.009	0.42	0.36
Entire	10	0.022	0.51	0.51	0.039	0.43	0.39
Entire	20	0.017	0.38	0.52	0.052	0.29	0.40
Entire	30	0.028	0.062	0.041	0.015	0.087	0.08
Entire	40	0.016	0.047	0.002	0.013	0.076	0.024
One$_a$	0	0.003	0.16	0.21	0.017	0.11	0.14
One	10	0.002	0.25	0.29	0.078	0.20	0.22
One	20	0.00003	0.34	0.38	0.084	0.33	0.47
One	30	0.0005	0.36	0.25	0.092	0.39	0.47
One	40	0.013	0.30	0.078	0.017	0.35	0.29
Two$_b$	0	0.22	0.70	0.65	0.32	0.70	0.55
Two	10	0.29	0.70	0.62	0.24	0.64	0.44
Two	20	0.64	0.38	0.61	0.80	0.07	0.29
Two	30	0.44	0.54	0.69	0.71	0.69	0.82
Two	40	0.58	0.76	0.68	0.44	0.83	0.85

$_a$-from 2229 UTC-0100 UTC $_b$-from 0113 UTC-0234 UTC

From these results, we can make generalizations about the each radar variables correlation to the total flash rate for different reflectivities. The radar variables tend to correlate with the total flash rate more closely reflectivity thresholds of 20 dBZ or higher. Although this is not specifically the case for the entire time series of J10, it is the case for the individual time series before and after the storm transition. The correlation between volume and flash-rate is most significant for high flash rate periods. Only in the case of the lagged data in the second time period of the storm does the peak height show any strong correlation, but even then the area and volume variables show a stronger correlation.

Further linear regressions of radar variables and total flash rates were performed while varying the temperature threshold for the area and volume calculations. Since the temperature parameter is not involved in the peak height variable, it is not considered here. Table 3.2 depicts the correlation coefficients for these linear regressions. This sensitivity test to the temperature parameter does not have as clear results as the sensitivity study of reflectivity. The best correlation of the area variable occurs when the temperature cutoff is either -10°C or -20°C. For the volume variable, the correlation is generally best at 0, 10 and 20

dBZ at -10°C or -20°C. Considering the portions of the storm separately for 30 and 40 dBZ, due to no correlation for the entire storm here, we find the best correlation at +10°C for the multicellular stage and -20°C for the single-cellular stage. A study of CG lightning in TOGA/COARE by Petersen et. al. (1996) found that necessary conditions for the onset of lightning include reflectivity volume of 30 dBZ above the -10°C temperature level. Additionally, most thunderstorm charging theories and observations have shown that the region of strongest charge separation is around the -10°C to -12°C temperature level (Workman and Reynolds, 1949; Takahashi, 1978; Saunders et al., 1991; Saunders, 1993). Due to this previous research, as well as the temperature sensitivity study for 10 July 1996 and 12 July 1996 (see Section 3.2), all further area and volume analysis were done using the -10°C level as the temperature parameter.

Table 3.2 Correlation Coefficients for July 10, 1996: Radar Variables vs. Flash Rate varying both reflectivity and temperature parameters

Time Period	Temp. (°C)	Reflectivity (dBZ)	Area R^2	Volume R^2
Entire[a]	10	0	0.46	0.47
Entire	0	0	0.47	0.46
Entire	-10	0	0.47	0.46
Entire	-20	0	0.51	0.52
Entire	10	10	0.51	0.52
Entire	0	10	0.48	0.44
Entire	-10	10	0.51	0.51
Entire	-20	10	0.53	0.48
Entire	10	20	0.37	0.49
Entire	0	20	0.38	0.51
Entire	-10	20	0.38	0.52
Entire	-20	20	0.36	0.41
Entire	10	30	0.052	0.046
Entire	0	30	0.051	0.045
Entire	-10	30	0.062	0.041
Entire	-20	30	0.094	0.019
Entire	10	40	0.056	0.012
Entire	0	40	0.064	0.012
Entire	-10	40	0.047	0.0019
Entire	-20	40	0.013	0.0057
One[b]	0	20	0.33	0.39
One	-10	20	0.34	0.38
One	-20	20	0.37	0.30
One	0	30	0.32	0.28
One	-10	30	0.36	0.25
One	-20	30	0.26	0.042
Two[c]	0	20	0.39	0.59
Two	-10	20	0.37	0.61
Two	-20	20	0.25	0.66
Two	0	30	0.48	0.66
Two	-10	30	0.54	0.69
Two	-20	30	0.69	0.73

[a]-2229 to 0234 UTC
[b]-2229 to 0113 UTC
[c]-0119 to 0234 UTC

This storm was a weak producer of CG lightning throughout its lifetime. Figure 3.6 shows the 5-minute averaged total flash rate, CG flash rate and IC/CG ratio over the lifetime of the storm. Periods of modest CG production, predominately negative in polarity, include one burst around 0010 UTC followed by a very small number of CG's after 0100 UTC. The resulting IC/CG ratio is low over the storm's lifetime, dropping below 0.6 once. The maxima in total flash rate, CG flash rate and radar parameters as well as total production of lightning and radar parameters will be discussed in Section 3.6, with the other cases.

3.2 July 12, 1996

Detailed reflectivity structures and lightning flash rates can be found in Lang (1997) for the 12 July 1996 case (J12). Figure 3.7 illustrates the CLASS sounding launched from Fort Morgan airport at 1356 MDT, approximately three hours before the four hour period from which we analyzed lightning and radar data for. Furthermore, the location of this sounding was over 100 km southeast of the initial convection. The CAPE was only 441 J kg^{-1}, the shear 13.6 m s^{-1} (over the lowest 6 km), the lifted index -3.5°C, and the Bulk Richardson Number 4.7. As in the previous case, the sounding does not represent the conditions at the time of convective initiation for this event. Additionally, it may not accurately represent the conditions during the mature stage of this case.

Figure 3.8 (a-f) presents horizontal cross sections of the reflectivity at a height of 1.5 km. Figure 3.9 (a-f) shows horizontal cross sections of reflectivity at a height of 9 km. Throughout the case, the storm was multicellular, initially moving into the northwest corner of the radar range around 2130 UTC (Fig. 3.8a) as a collection of eight small cells that exceeded 30 dBZ. By 2201 UTC (Fig. 3.8b), two cells, oriented in an east west line, dominated with low level reflectivities exceeding 50 dBZ. At this time (see Fig. 3.9b), an anvil had begun to form above the low level reflectivity cores. These cells propagated and redeveloped in an east-southeast fashion, dividing into four cells with reflectivities above 50 dBZ at 2230 and 2300 UTC (Figs. 3.8c and 3.8d). Due to other convection within the research project domain, the radar data was limited to the collection of cells shown in Figs. 3.8 and 3.9. Furthermore, the lightning data was filtered spatially to the same area.

The J12 case exhibited low to moderate correlations between radar and lightning variables on radar volume time scales (approximately ten minutes). Figure 3.10 (a-b) shows plots of radar variables versus total flash rate for the different reflectivity thresholds. In this case, the total lightning flash rate data from the interferometer was not valid, as the storm crossed the baseline of the network during the strongest periods of radar reflectivity (2140 UTC through 2230 UTC).

Linear regressions performed for the J12 case resulted in the correlation coefficients listed in Table 3.3. Though the correlation is not as significant as in the J10 case, especially at 0, 10 and 20 dBZ thresholds, there is a clear trend for increased correlation with high reflectivities. For the variation of the temperature cutoff between 0 and -10°C, the higher correlation coefficients occur for the -10°C level. As further explained in Section 3.1, area and volume radar variables will use -10°C as the temperature parameter.

Table 3.3 Correlation Coefficients for July 12, 1996: Radar Variables vs. Total Flash Rate varying both the reflectivity threshold and the temperature parameter.

Temp. (°C)	Reflectivity (dBZ)	Peak Height R^2	Area R^2	Volume R^2
0	0	0.13	0.07	0.18
-10	0	0.15	0.11	0.21
0	10	0.20	0.21	0.29
-10	10	0.19	0.20	0.28
0	20	0.20	0.20	0.33
-10	20	0.20	0.22	0.34
0	30	0.17	0.26	0.44
-10	30	0.17	0.28	0.48
0	40	0.28	0.31	0.47
-10	40	0.28	0.38	0.47

This case produced significantly more CG strikes than the J10 case. Figure 3.11 shows the 5-minute averaged total flash rate, CG flash rate and IC/CG ratio over the lifetime of the storm. The portion of the storm with lightning data coverage extends from 2224 to 0200 UTC. This storm had typical mid-latitude IC/CG ratios of approximately 0.8 during the storm's lifetime (Prentice and Mackerras, 1977). The maxima in total flash rate, CG flash rate and radar parameters, as well as total production of lightning and radar parameters, will be discussed in Section 3.6 with the other cases.

3.3 July 9, 1996

The case on 9 July 1996 (J9) was significantly different from both the J10 and J12 cases. In the J9 case, the northern Colorado Front Range was under an upslope induced cloud cover. In addition, a mesoscale circulation, consistent with the Denver cyclone as described by Crook et. al. (1990) and Crook et. al. (1991), was in place over the region. The Denver cyclone is a well known feature that aids convective initiation, particularly of strong convection, in this region. Figure 3.12 illustrates the CLASS sounding launched from Fort Morgan airport at 1430 MDT approximately two hours before the two hour period of appropriate lightning and radar data. The CAPE was only 236 J kg^{-1}, the shear 7.0 m s^{-1} (over the lowest 6 km), the lifted index -0.9°C, and the Bulk Richardson Number 9.7. Of the convection elements embedded throughout the research area, cells located west of the radar site along the Front Range were those analyzed for this work.

Storm structure was generally multicellular in nature for the J9 case, embedded within a large area of stratiform precipitation. Fig. 3.13 (a-h) shows horizontal cross sections of reflectivity at a height of 1.5 km for the J9 case. Fig. 3.14 (a-h) depicts horizontal cross sections at a height of 7 km. The cells examined in detail are located around 90 km west and 60 km north of the CSU-CHILL radar (see Fig. 3.13a). The radar data was spatially filtered to a range of 60 km of the strongest cells. This storm is less vertically developed; the upper level is captured at a height cross section of 7 km. The strongest cells occurred between 2230 and 2300 UTC, producing reflectivities > 50 dBZ. The convection was 80 to 100 km east of the radar for the first hour (2200-2300 UTC) and then began to propagate or redevelop to the southeast. See Figure 3.15 (a-b) for plots of 0 and 30 dBZ time series of radar variables versus total flash rates. In this case, there was no correlation on the radar volume time scale (approximately six minutes) between radar variables and the total flash rate.

Since this case was much less vertically developed than the J9 and J10 cases, it is consistent with the lower total flash rates. Figure 3.16 shows the 5-minute averaged total flash rate and CG flash rate over the lifetime of the storm. The lightning data for the J9 case extended from 2200 to 2343 UTC. The IC/CG ratio is lower for this storm than other cases examined in this chapter, falling lower than typical mid-latitude values of about 0.8. The maxima in total flash rate, CG flash rate and radar parameters as well as total production of lightning and radar parameters are discussed in Section 3.6, with the other cases.

3.4 July 30, 1996

On the evening of 30 July 1996, two severe hailstorms moved through Morgan county in northeast Colorado. Several hours before, some initial convection of a much weaker nature moved through the same area northwest of the CHILL radar. These earlier, smaller storms are considered as one case (J30a) and the hailstorms are considered a second case (J30b). No sounding data were available for these events.

Fig. 3.17 (a-j) and Fig. 3.18 (a-j) depict cross sections of horizontal reflectivity at 1.5 km and 9 km respectively, during the J30 cases. The first cells on J30 (case a) briefly flared > 50 dBZ around 0030 UTC before weakening and propagating to the southeast. The second round of convection to the east of the radar developed NNE of the radar and dropped into the radar's range around 0130 UTC. The western flank of the strong multicellular was positioned about 40 to 60 km west of the radar continually propagating to the south. The strongest stages included two or more cells with reflectivities stronger than 60 dBZ from 0300 UTC through 0500 UTC (Figs. 3.18f-j), at which time the cells had left the southern portion of the eastern ITF lobe. The J30a case had weak reflectivities aloft at the 9 km level, with small areas of reflectivity advected to the east of the low level reflectivity cores (see Fig. 3.18a-c). The J30b case had very large areas of low reflectivity extending all the way to the east of the radar data range (150 km east of the radar). In addition, there are high reflectivity cores aloft indicating the storm's vigorous nature. Figure 3.19 (a-b) shows plots of 0 and 30 dBZ time series of radar variables versus total flash rates. In these cases, there was little correlation on the radar volume time scale between radar variables and the total flash rate.

The J30a case was a minor producer of CG lightning. The J30b case was an example of a severe hailstorm producing large amounts of IC lightning. The J30b case had the highest fraction of positive ground strokes, 39%, of any case that was examined. Figure 3.20 (a-b) presents the 5-minute averaged total flash rate, CG flash rate and IC/CG ratio over the lifetime of the storm. The lightning data for these cases includes from 0000 to 0100 UTC for the J30a case and 0130 to 0430 UTC for J30b. The J30a case produced moderate flash-rates, up to 17 flashes per minute at 0019 UTC and two peaks in the CG flash rate of 3 flashes per minute at 0023 and 0047 UTC. The J30b case included many pulses in the total flash rate with peaks at or above 80 flashes per minute around 0150 UTC and at 0245, 0251 0300 and 0324 UTC.

The maxima in total flash rate, CG flash rate, total production of lightning and radar variables are discussed in Section 3.6 along with the other cases.

3.5 August 9, 1996

On August 9, 1996 some electrified low precipitation cells moved through the research area. This case (A9) was studied via FCM data, unlike the other cases in this chapter, which used data from the ITF interferometer. No sounding data were available for this case. The convection on this day initiated on the Cheyenne Ridge to the north of the research area before moving southeast into the study area. Fig. 3.21 (a-f) and Fig. 3.22 (a-f) depict cross sections of horizontal reflectivity at 1.5 km and 7 km, respectively, during the A9 case. This small multicelled storm never produced more than two cells with reflectivity above 40 dBZ. Figure 3.23 (a-b) shows a time series of radar variables versus total flash rates for 0 and 30 dBZ. In these cases there was little correlation on the radar volume time scale between radar variables and the total flash rate.

This case was less vertically developed than the J9 and J10 cases, which lead to lower total flash rates. Figure 3.24 shows the 5-minute averaged total flash rate and CG flash rate over the lifetime of the storm. Importantly, the total flash rate is simply an estimate from the flatplate antenna (FCM). The estimate of total flashes for the entire storm at 3,077 over an hour data period is abnormally high and will not be considered when comparing to other cases in Section 3.6. The total flash data only exists for the time period 2216 to 2320 UTC. Interestingly, of the four CG flashes the storm produced over its entire lifetime, each were positive ground strokes.

Table 3.4 Radar Maxima for the 9 August 1996 storm

Maxima			
Reflectivity	Peak Height	Area	Volume
00 dBZ	13	2714	10709
10 dBZ	13	1647	5653
20 dBZ	13	668	2634
30 dBZ	12	156	382
40 dBZ	11	44	129

[a]-at 2221 UTC

3.6 Comparison of northeast Colorado cases

We have examined the correlations of total flash rate with radar parameters for five cases in northeastern Colorado. Significant correlations were found for the July 10 and 12 cases, especially for the area and volume variables. In the A9, J9, J30a, and J30b cases, especially before each storm's weakening, weak correlations between radar variables and the total flash rate were found. We examined the J10 and J12 cases for changes in these correlations with changes in the reflectivity and temperature parameters. The correlations between total flash rate and all radar variables were improved by using higher reflectivity thresholds than the 0 dBZ threshold (taken as a proxy for cloud top). Also, it was determined that the storm area and volume correlated better to the total flash rate with the -10°C temperature threshold. The better correlation with high reflectivities, area, volume and the -10°C level suggests these parameters are more directly linked to the microphysical properties of charge separation and updraft velocities.

We now examine the maximum total flash rates, CG flash rates, and radar parameters for the five cases, excluding total flash rate data for the 9 August 1996 case (because of the erroneous flash rates for that case). The maxima for the radar parameters are listed in Table 3.5. The maxima in lightning flash rates are listed in Table 3.6. The -10°C temperature threshold was used to calculate the area and volume estimates in Table 3.5.

Table 3.5 Maximum Radar Parameters

July 9th	Height (km)	Area (km^2)	Volume (km^3)	July 10th	Height (km)	Area (km^2)	Volume (km^3)
0 dBZ	15.5	7800	37500	0 dBZ	17	3300	23000
10 dBZ	15.5	6700	23000	10 dBZ	15.5	2700	16000
20 dBZ	12	4400	7000	20 dBZ	15.5	1400	5400
30 dBZ	12	440	930	30 dBZ	14.5	490	2000
40 dBZ	11	95	120	40 dBZ	13.5	225	990
July 12th				**July 30thA**			
0 dBZ	15	5500	27500	0 dBZ		2800	12500
10 dBZ	13.5	4800	18500	10 dBZ	14	2100	7100
20 dBZ	13	3300	7200	20 dBZ	12.5	920	2300
30 dBZ	13	640	1700	30 dBZ	12.5	300	650
40 dBZ	13	280	670	40 dBZ	10.5	130	200
July 30thB				**August 9th**			
0 dBZ		5000	40000	0 dBZ	13	2700	11000
10 dBZ		4900	33000	10 dBZ	13	1600	5700
20 dBZ	15.5	3200	15000	20 dBZ	13	670	2600
30 dBZ	15	1250	5600	30 dBZ	12	160	380
40 dBZ	14	650	2400	40 dBZ	11	44	130

Table 3.6 Maximum Lightning Parameters

Case	Total Flash Rate (min-1)	CG Flash Rate (min-1)
July 9	30	11
July 10	42	3
July 12	65	7
July 30a	17	3
July 30b	89	10

The correlations between the peak radar parameters and peak total flash rate are shown in Fig. 3.25. As in the correlations for the individual cases, the peak height shows weaker correlations at reflectivities lower than 30 dBZ. The volume shows stronger correlations than peak height at all reflectivities except matching at 40 dBZ. Although, at 0 dBZ (cloud top height) one would expect a non-linear relationship such as the one described by Price and Rind (1992) of flash rate being proportional to the fifth power of the cloud top height. A power law fit to our five cases for the 0 dBZ resulted in the relationship:

$$FR = 2.0 \times 10^{-5} \times H^{5.15} \quad (R^2 = 0.76) \qquad (3.1)$$

This equation is similar to Price and Rind's continental parameterization of FR= $3.44 \times 10^{-5} \times H^{4.9}$. Once again, like in the previous results, stronger correlations are found at the reflectivity thresholds above 20 dBZ. In Figure 3.26, we compare the PR92 parameterization with our northeast Colorado cases. We find that two of our cases exceed the PR92 continental parameterization by 30 flashes per minute. The Price and Rind parameterization seems to identify a lower bound. These results should be interpreted with caution since we have examined relatively few cases.

We will now investigate the relationship between the scale of a thunderstorm and its lightning flash rate. The following arguments are adapted from PR92. The potential difference (V) due to a point charge (q) at a distance R is given by:

$$V = \frac{kq}{R} \qquad (3.2)$$

where $k=1/4\varepsilon_0$, with ε_0 the permittivity of a vacuum. The electrical power between two point charges is $W= Vq'$, where q' is the magnitude of the point charge. Now for the electrical charge regions in thunderstorms we have:

$$W = \frac{kQQ'}{R} \qquad (3.3)$$

where Q and Q' are the magnitudes of the charge regions. Now we depart from PR92's arguments, instead of assuming the region's charges are given by:

$$Q \approx q * \text{Volume} \approx H^3 \qquad (3.4)$$

we assume: $Q \approx q *$ Volume. We also assume the distance between the charge regions is given by $R \approx$ Volume/Area. This assumption may introduce error for arbitrarily shaped volumes, but certainly is a stricter assumption than assuming the space charge is proportional to the height raised to the third power (eq. 3.4). Thus we have:

$$W \approx \text{Volume} * \text{Area} \qquad (3.5)$$

Next, following PR92, electrical power (W) is assumed to be proportional to the total flash-rate through the generation of charge regions and resulting electrical breakdowns between the regions.

We now examine if this relationship, total flash rate proportional to the product of volume and area, applies to our cases. In Table 3.7, the linear correlation of the product of the peak radar area and volume (mVA) with peak total flash rate is shown at the different reflectivity thresholds. This table includes all of the cases except the J9 case. This case did not follow the same trend between the mVA and the peak total flash rate. For the structure of this system, convection embedded within stratiform precipitation, larger areas and volumes were computed than would be associated with the convective elements themselves for the lower reflectivity thresholds. Using high reflectivity thresholds isolates the radar variables to the region associated with charge separation (see Chapter 5, Section 1). By using higher reflectivity thresholds, we have partitioned the stratiform precipitation portion echo out of our calculation of the radar variables. Note how the correlation of the product of area and volume with the flash rate increases when the J9 case is excluded from the regression analysis, especially at lower reflectivity.

Table 3.7 Correlation of Volume and Area Product with Maximum Total Flash Rate

Refl. (dBZ)	w/o J9	All
0	0.98	0.094
10	0.95	0.35
20	0.93	0.59
30	0.71	0.73
40	0.68	0.72

So far, we have only considered parameters that may predict the peak total flash rate for a convective event. We will now investigate total storm flash production. Table 3.8 lists the total production of different lightning parameters. Interestingly, the wide range of total IC produced per CG flash range from 95 for the J10 case to 5 for the J30b case. These trends, as well as the trend between the hourly production of total flashes (TIC/H) and averaged radar parameters, are discussed in Chapter 5 in conjunction with the tropical cases.

Table 3.8 Total Storm Lightning Parameters

Case	Max FR	Total F	Max CG	Total CG	Total +CG	% IC	% + CG
J9	30	1349	11	478	28	0.646	0.059
J10	42	3615	3	77	13	0.979	0.169
J12	67	4733	7	359	36	0.924	0.100
J30a	17	477	3	35	0	0.927	0
J30b	89	3396	10	619	242	0.818	0.391

From these cases, we have found that the best predictor of peak total flash rate for a convective event is the product of the maximum storm area and volume, as derived from radar data. This variable predicts better than area, volume or peak height used individually. The lower correlation between the peak area volume products and the peak total flash rate for all the cases, including the J9 case, at the low reflectivity thresholds (see Table 3.7) shows that realistic prediction of total flash rate requires high reflectivities for systems similar to the J9 case (such as mesoscale systems).

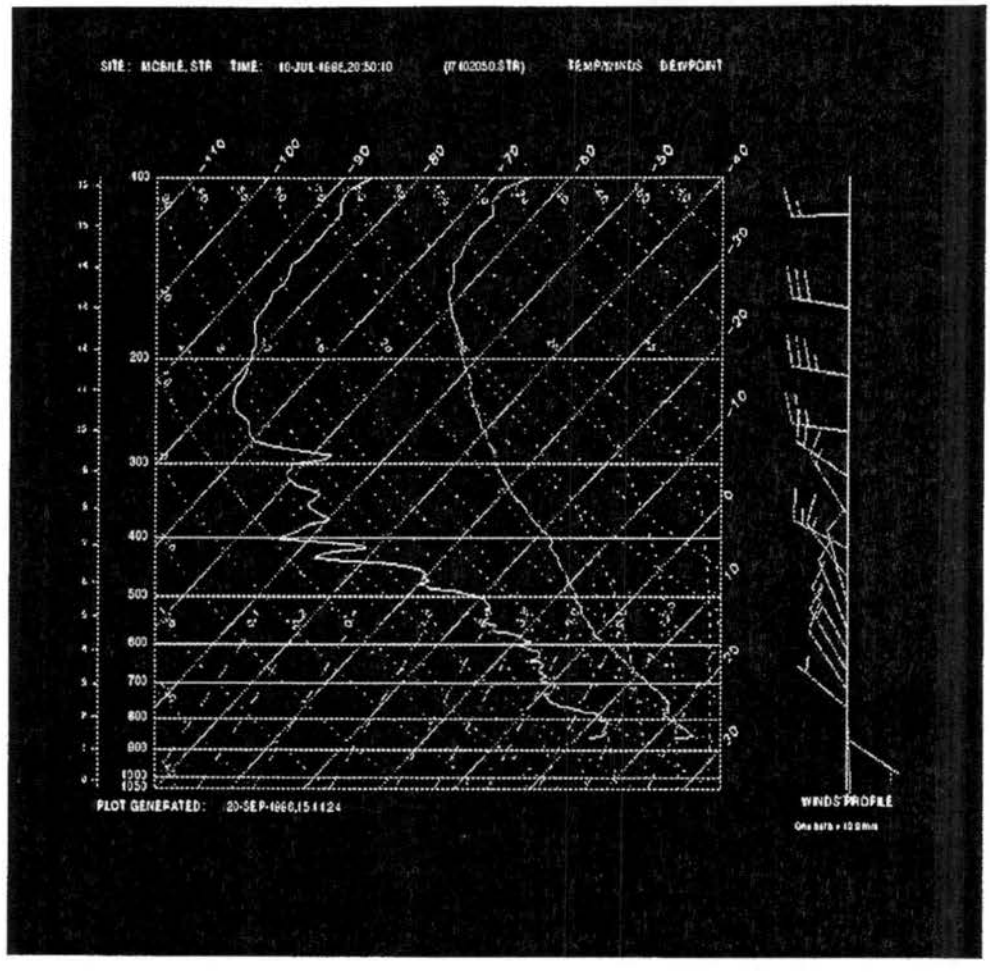

Figure 3.1 Mobile CLASS sounding from 2050 UTC 10 July, 1996.

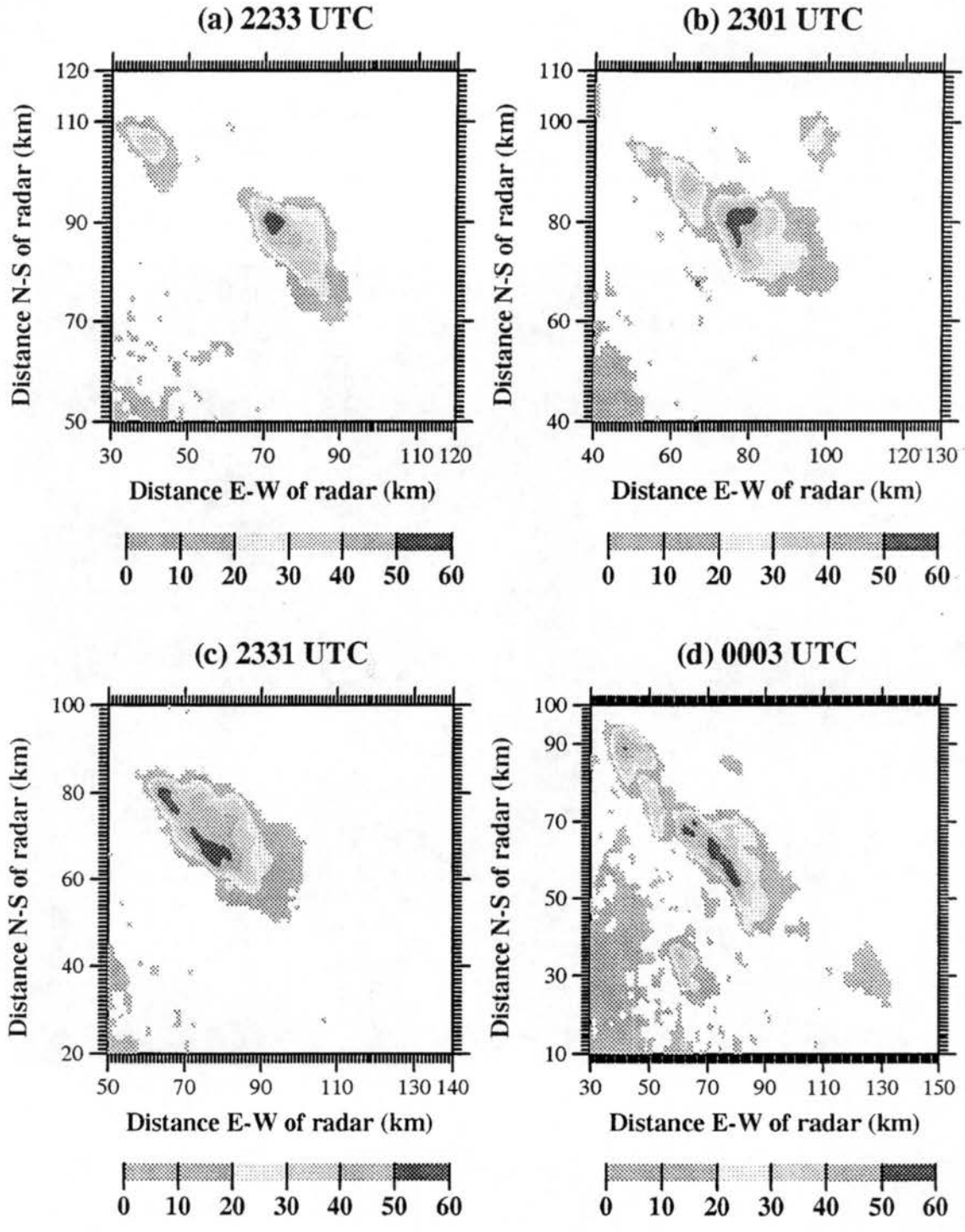

Fig. 3.2 (a-d) Horizontal radar reflectivity cross sections at height of 1.5 km from the CSU-CHILL radar for: a) 2233 UTC; July 10, 1996; b) 2301 UTC; July 10, 1996; c) 2331 UTC; July 10, 1996; d) 0003 UTC; July 11, 1996. Notice changes in scale.

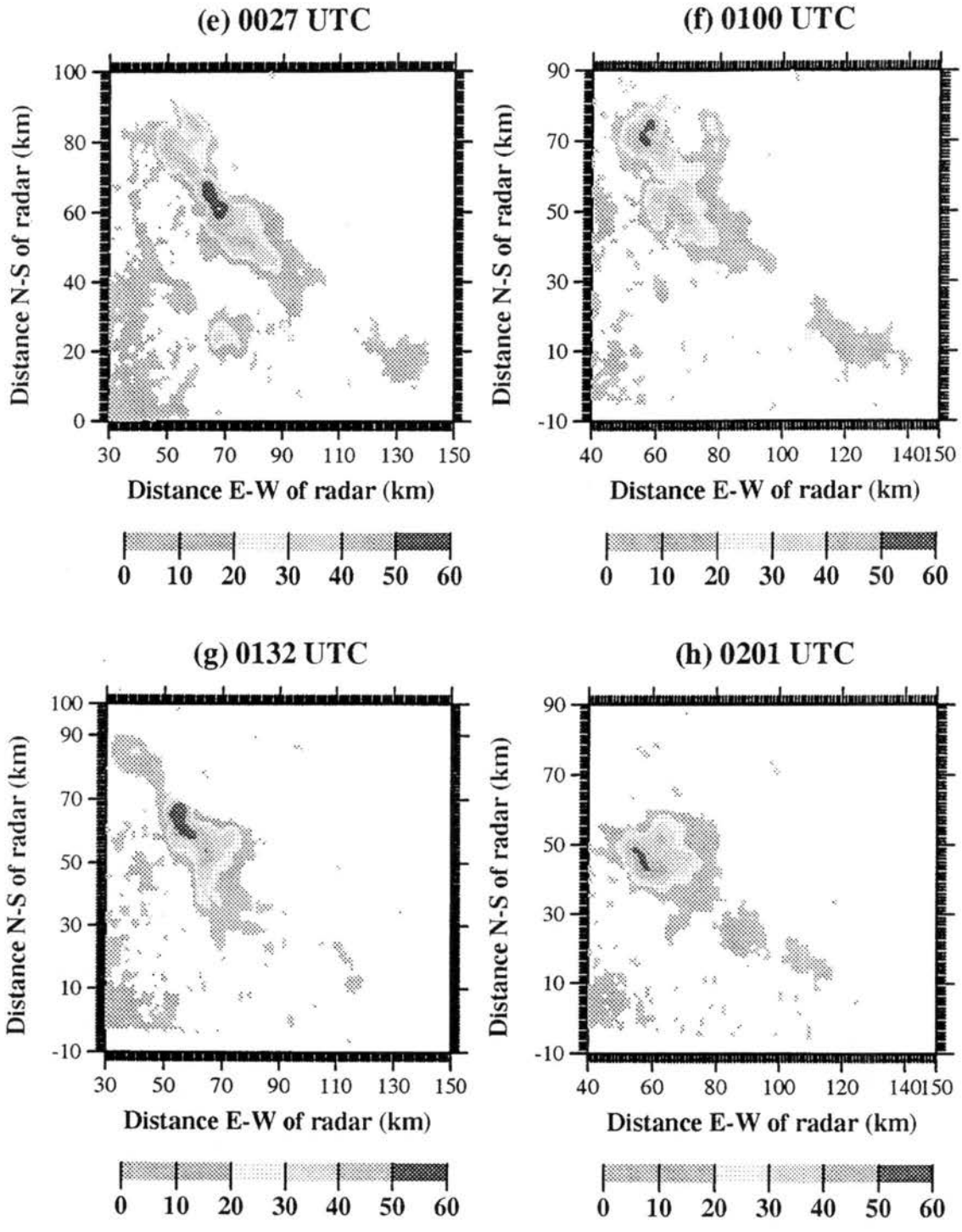

Fig. 3.2 (e-h) Horizontal radar reflectivity cross sections at height of 1.5 km from the CSU-CHILL radar for: e) 0027 UTC; July 11, 1996; f) 0100 UTC; July 11, 1996; g) 0132 UTC; July 11, 1996; h) 0201 UTC; July 11, 1996. Notice changes in scale.

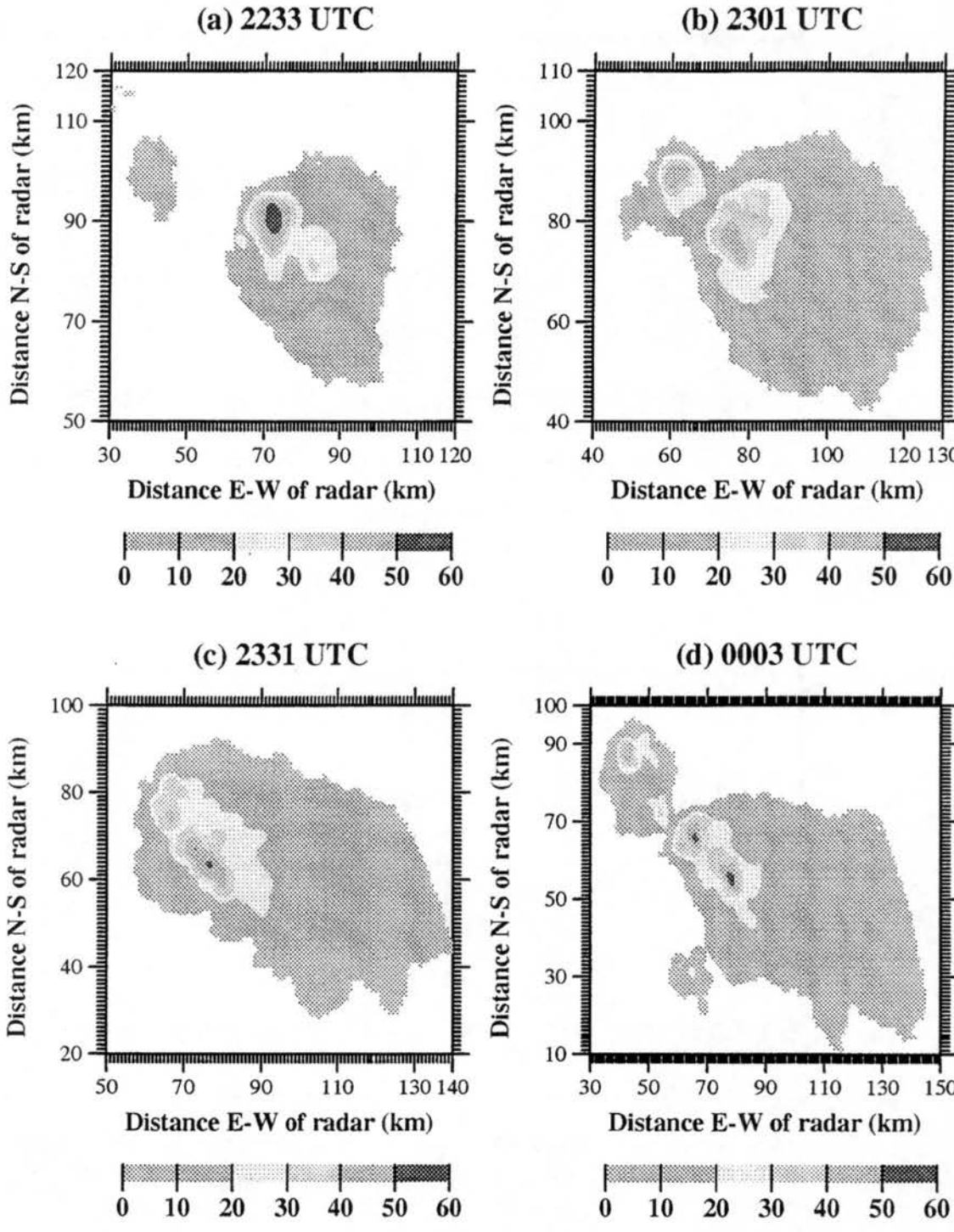

Fig. 3.3 (a-d) Horizontal radar reflectivity cross sections at height of 9 km from the CSU-CHILL radar for: a) 2233 UTC; July 10, 1996; b) 2301 UTC; July 10, 1996; c) 2331 UTC; July 10, 1996; d) 0003 UTC; July 11, 1996. Notice changes in scale.

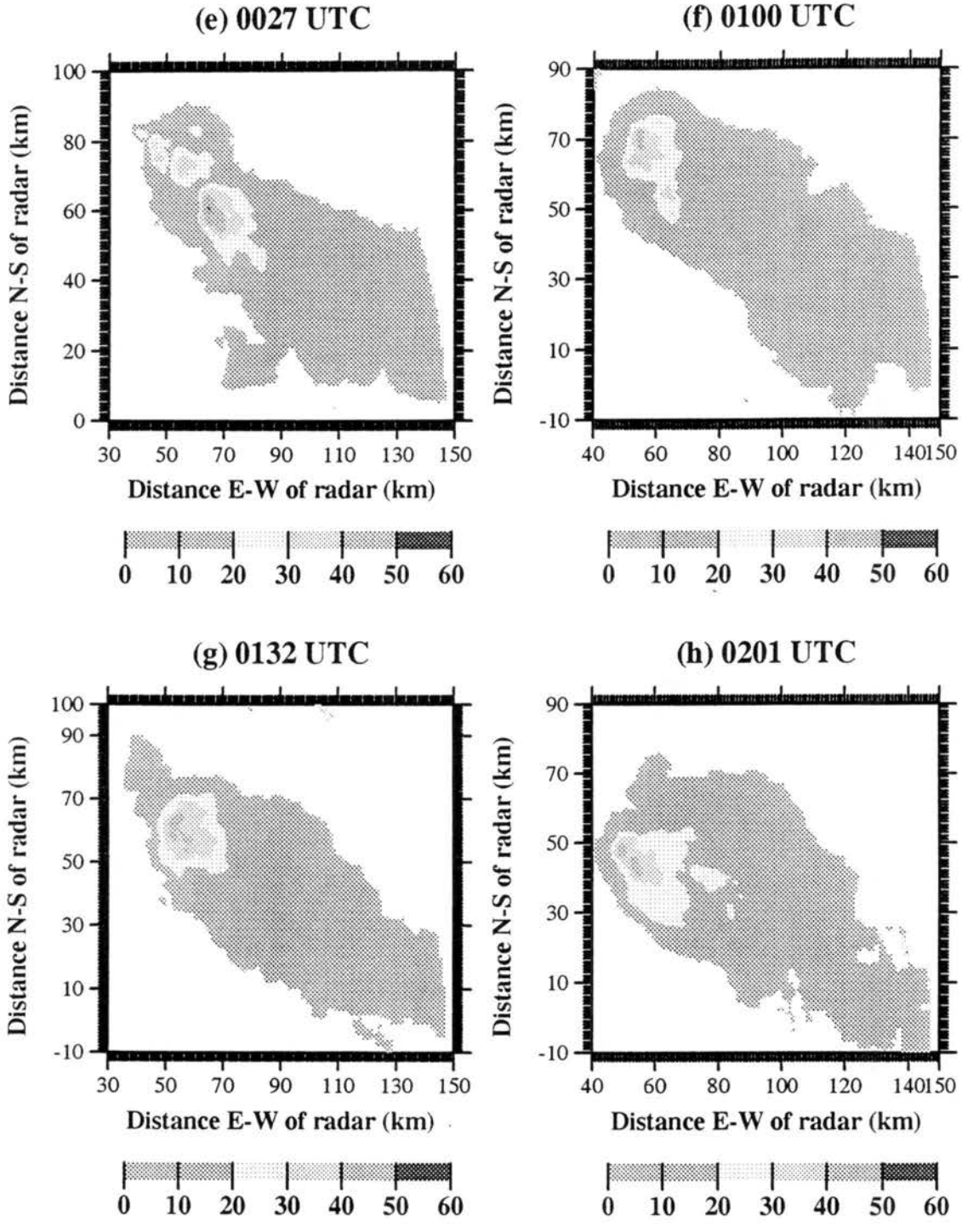

Fig. 3.3 (e-h) Horizontal radar reflectivity cross sections at height of 9 km from the CSU-CHILL radar for: e) 0027 UTC; July 11, 1996; f) 0100 UTC; July 11, 1996; g) 0132 UTC; July 11, 1996; h) 0201 UTC; July 11, 1996. Notice changes in scale.

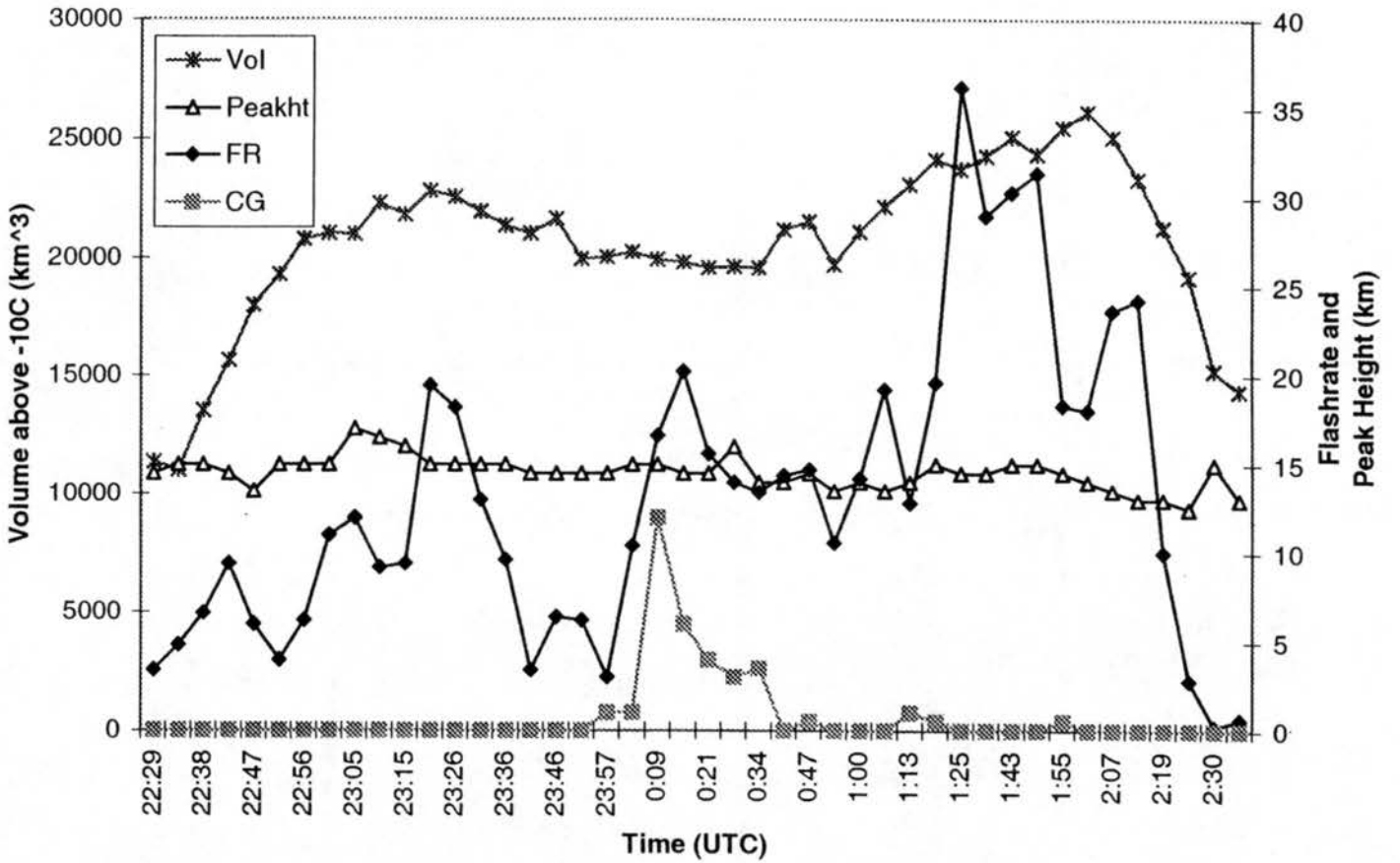

Figure 3.4 (a) Time series of radar and lightning variables: 2229 July 10, 1996 through 0234 UTC July 11, 1996. Radar variables calculated using 0 dBZ and -10°C thresholds. Flash rates (min^{-1})are five minute averages.

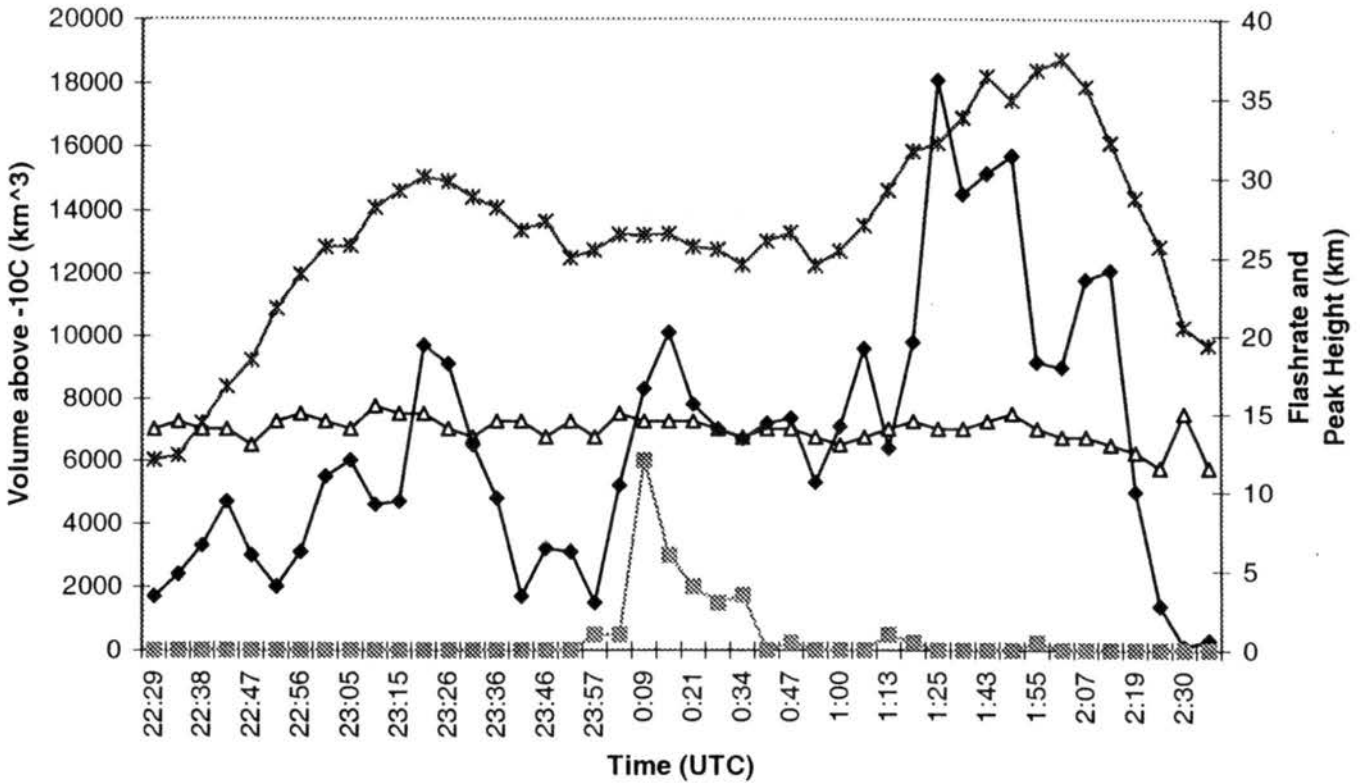

Figure 3.4 (b) Time series of radar and lightning variables: 2229 July 10, 1996 through 0234 UTC July 11, 1996. Radar variables calculated using 10 dBZ and -10°C thresholds. Flash rates (min^{-1}) are five minute averages. Symbols are as in Figure 3.4 (a).

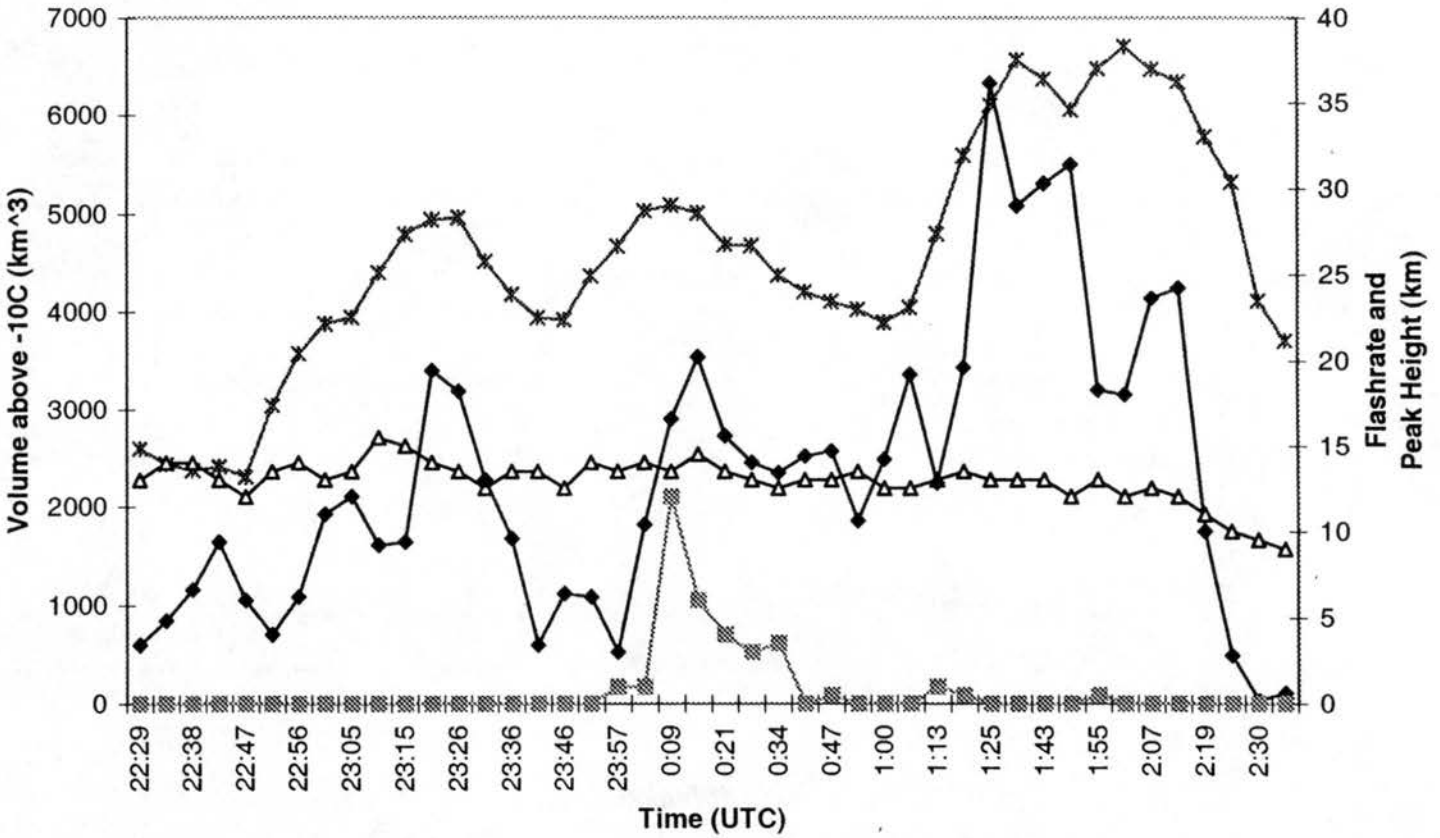

Figure 3.4 (c) Time series of radar and lightning variables: 2229 July 10, 1996 through 0234 UTC July 11, 1996. Radar variables calculated using 20 dBZ and -10°C thresholds. Flash rates (min^{-1}) are five minute averages. Symbols are as in Figure 3.4 (a).

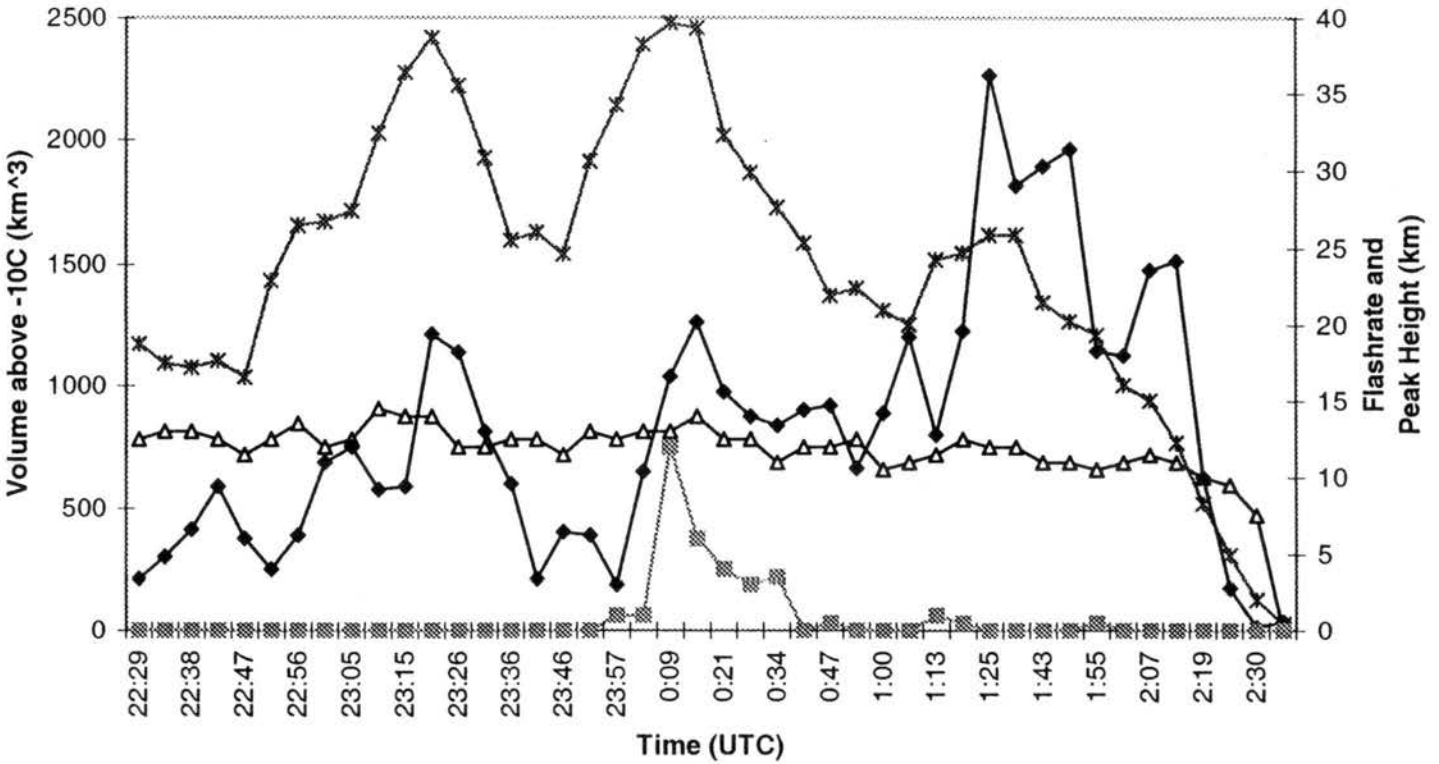

Figure 3.4 (d) Time series of radar and lightning variables: 2229 July 10, 1996 through 0234 UTC July 11, 1996. Radar variables calculated using 30 dBZ and -10°C thresholds. Flash rates (min^{-1}) are five minute averages. Symbols are as in Figure 3.4 (a).

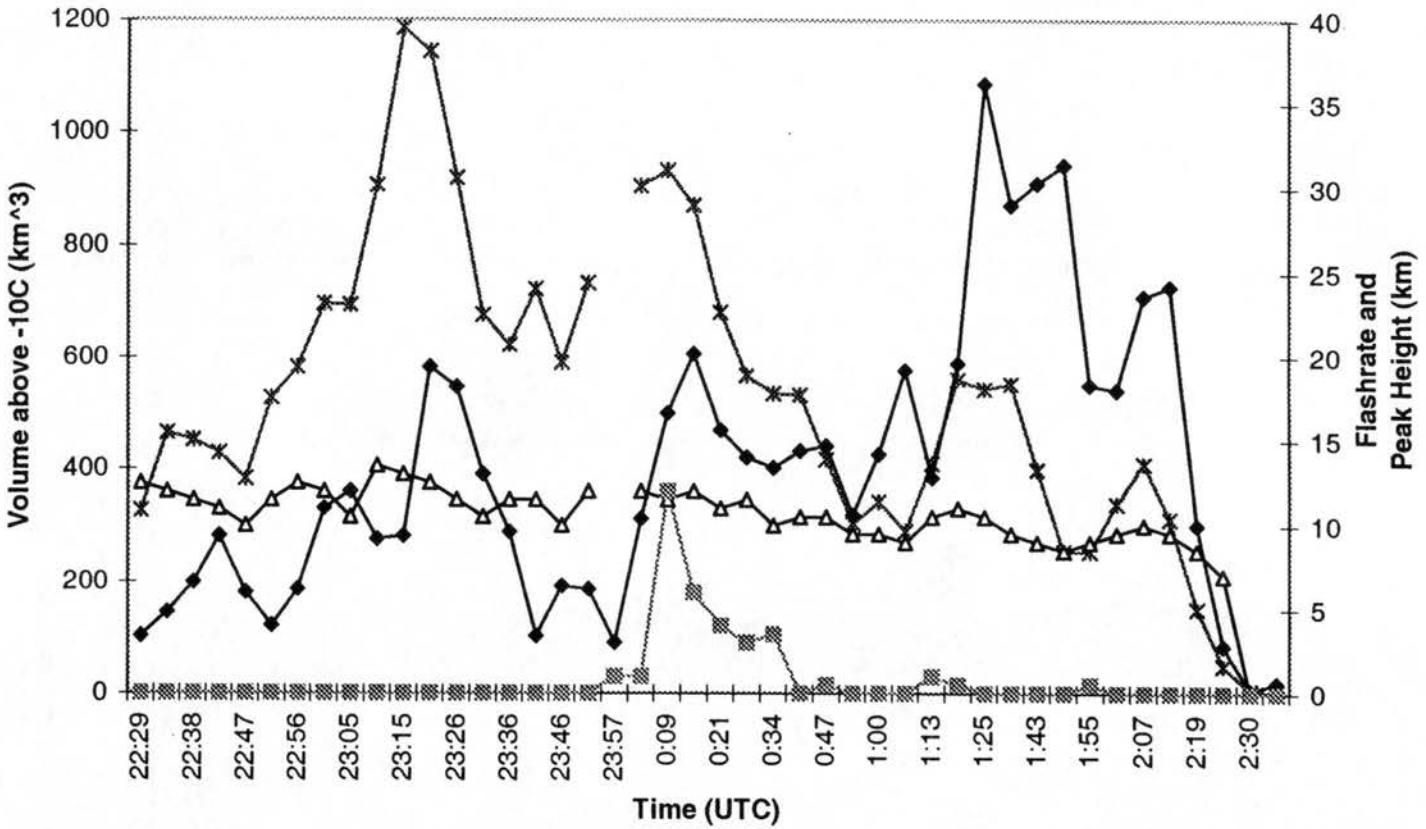

Figure 3.4 (e) Time series of radar and lightning variables: 2229 July 10, 1996 through 0234 UTC July 11, 1996. Radar variables calculated using 40 dBZ and -10°C thresholds. Flash rates (min^{-1}) are five minute averages. Symbols are as in Figure 3.4 (a).

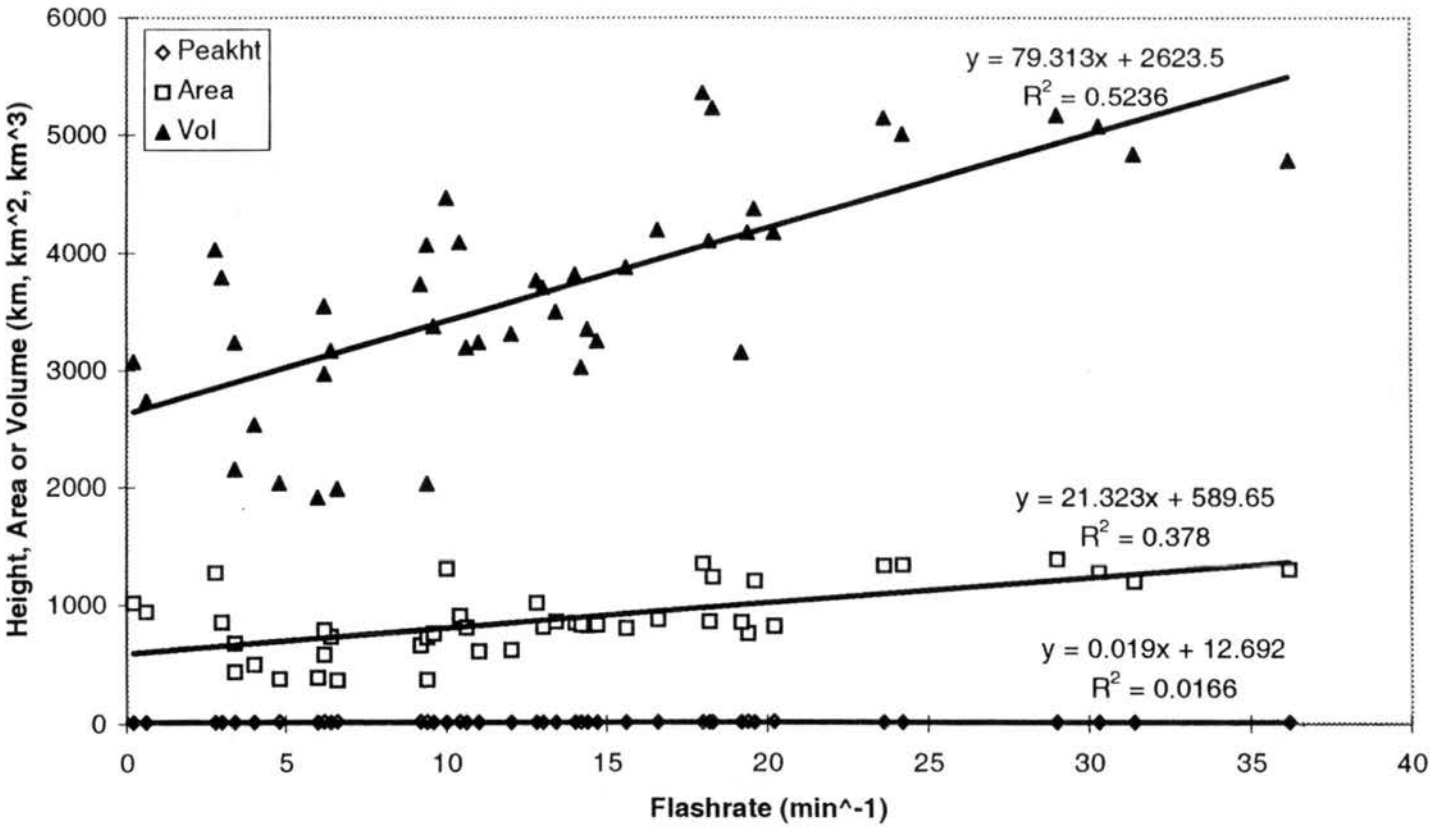

Figure 3.5 Linear regressions between peak height, area and volume and total flash rate for 10 July 1996 case. Radar variables calculated using 20 dBZ and -10°C thresholds. Equations and correlation coefficient are shown.

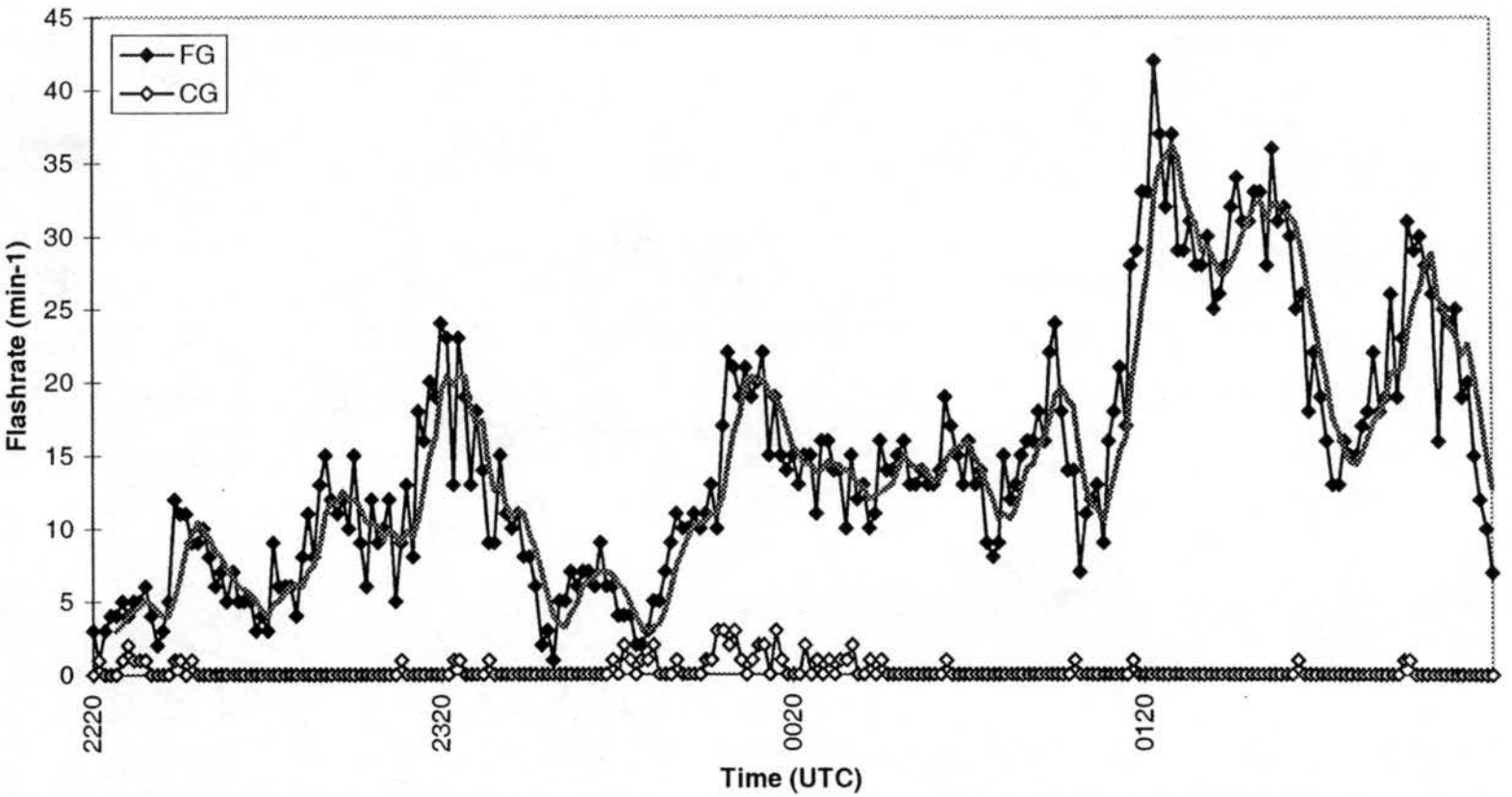

Figure 3.6 Time series of lightning flashrates from 10 July 1996 case. FR indicates total flash rate (min^{-1}). Five minute moving average of FR shown in thick red line. CG indicates cloud-to-ground flash rate (min^{-1}).

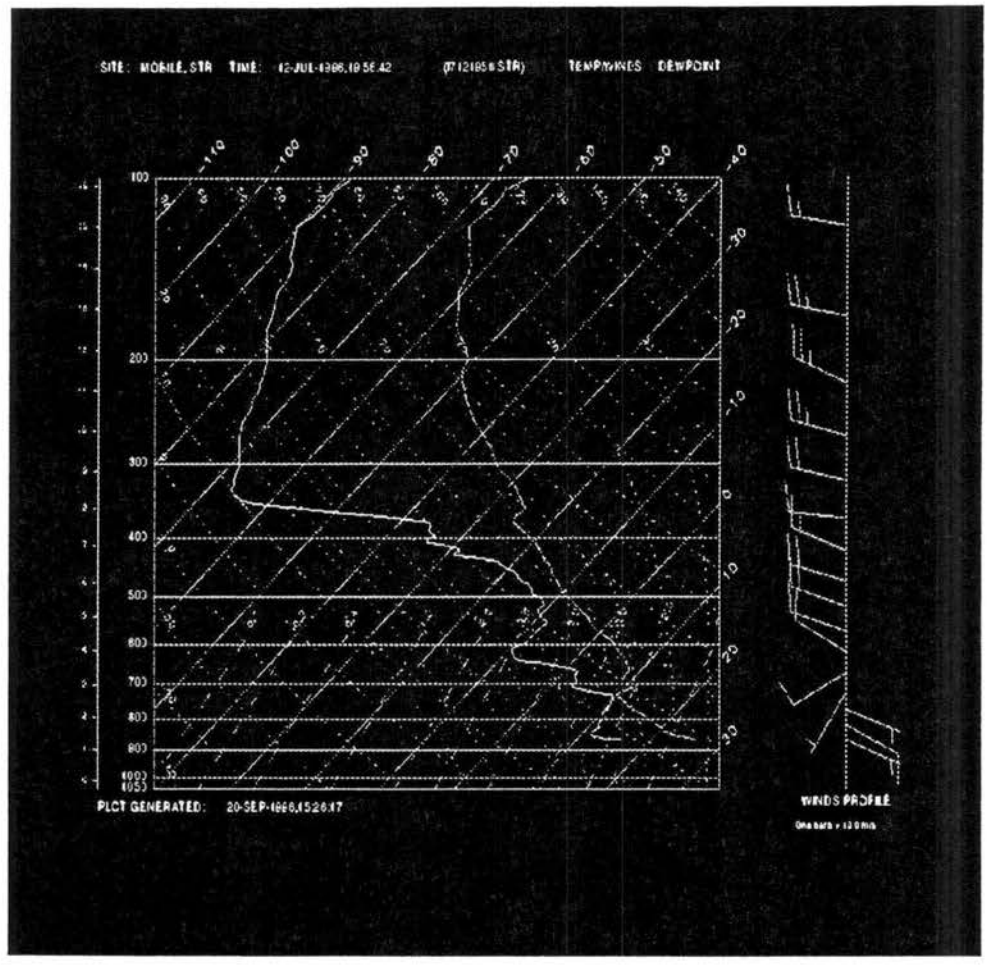

Figure 3.7 Mobile CLASS sounding from 1956 UTC 12 July 1996.

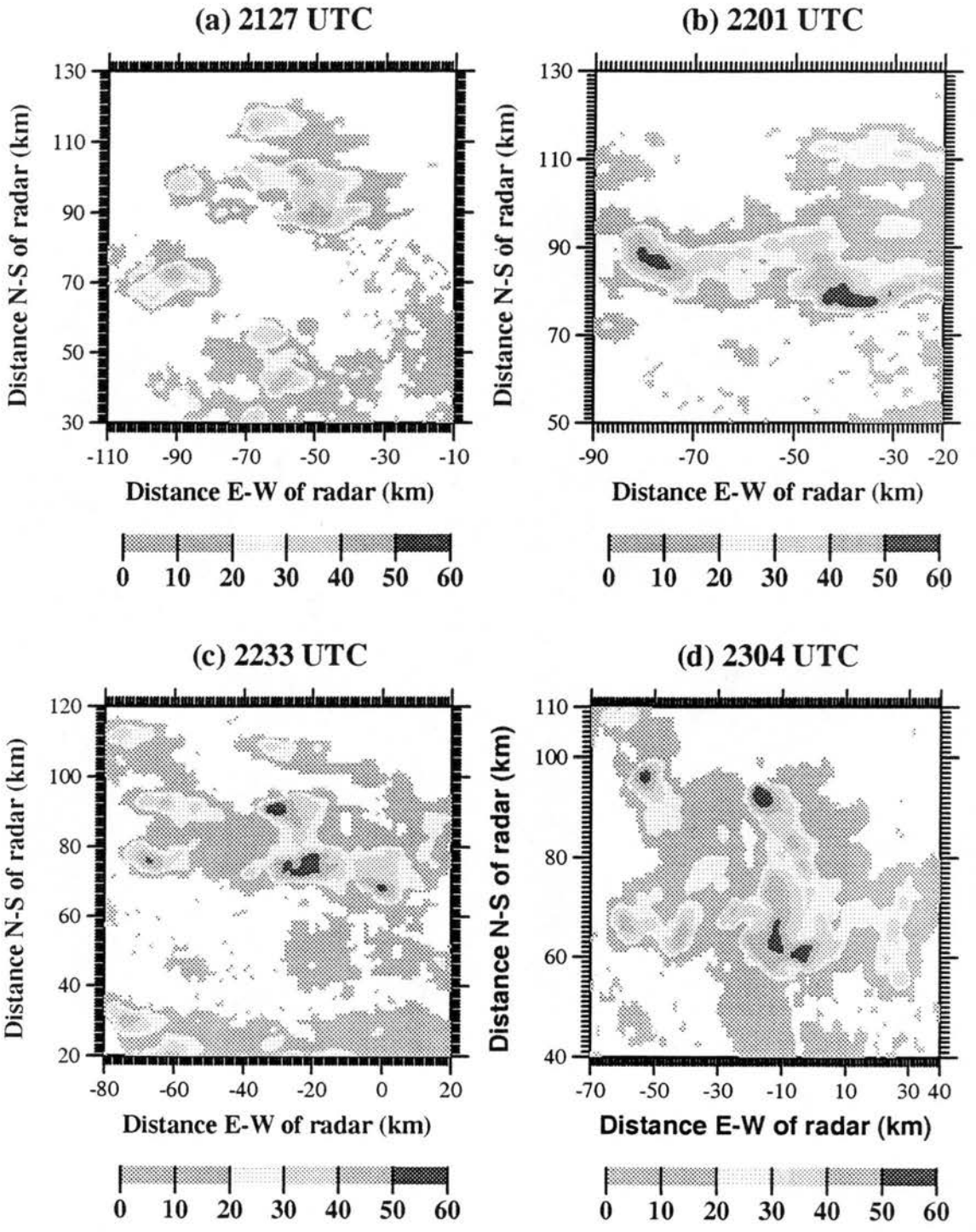

Figure 3.8 (a-d) Horizontal radar reflectivity cross sections at height of 1.5 km from the CSU-CHILL radar for: a) 2127 UTC; July 12, 1996; b) 2201 UTC; July 12, 1996; c) 2233 UTC; July 12, 1996; d) 2304 UTC; July 12, 1996. Notice changes in scale.

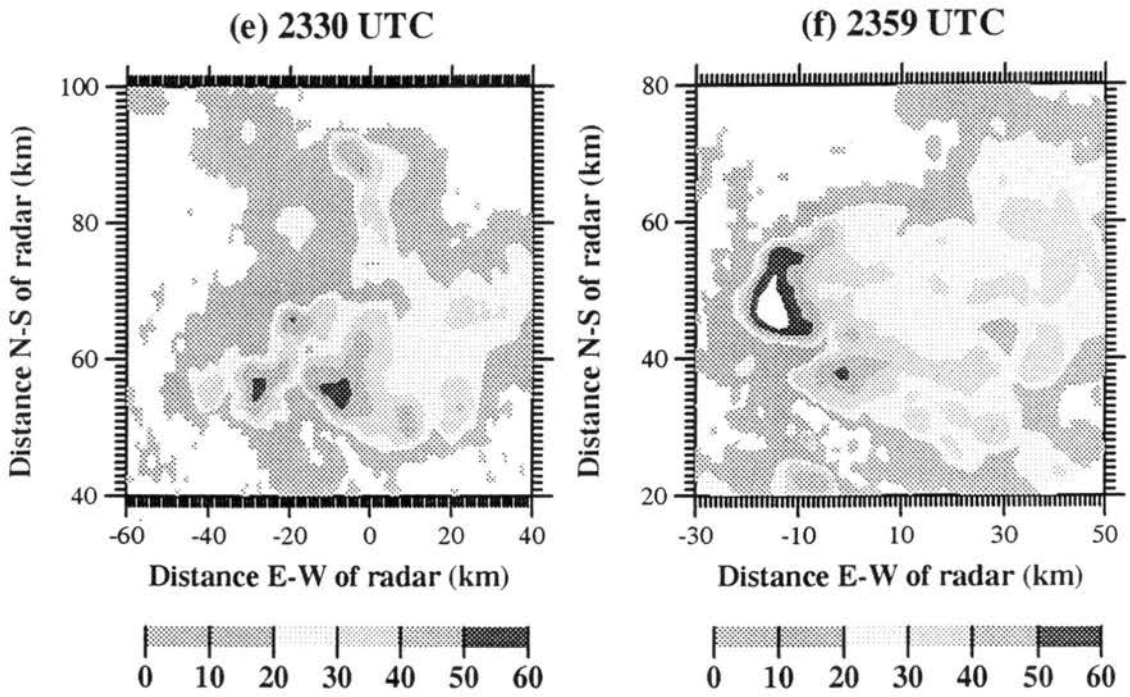

Figure 3.8 (e-f) Horizontal radar reflectivity cross sections at height of 1.5 km from the CSU-CHILL radar for: e) 2330 UTC; July 12, 1996; f) 2359 UTC; July 12, 1996. Notice changes in scale.

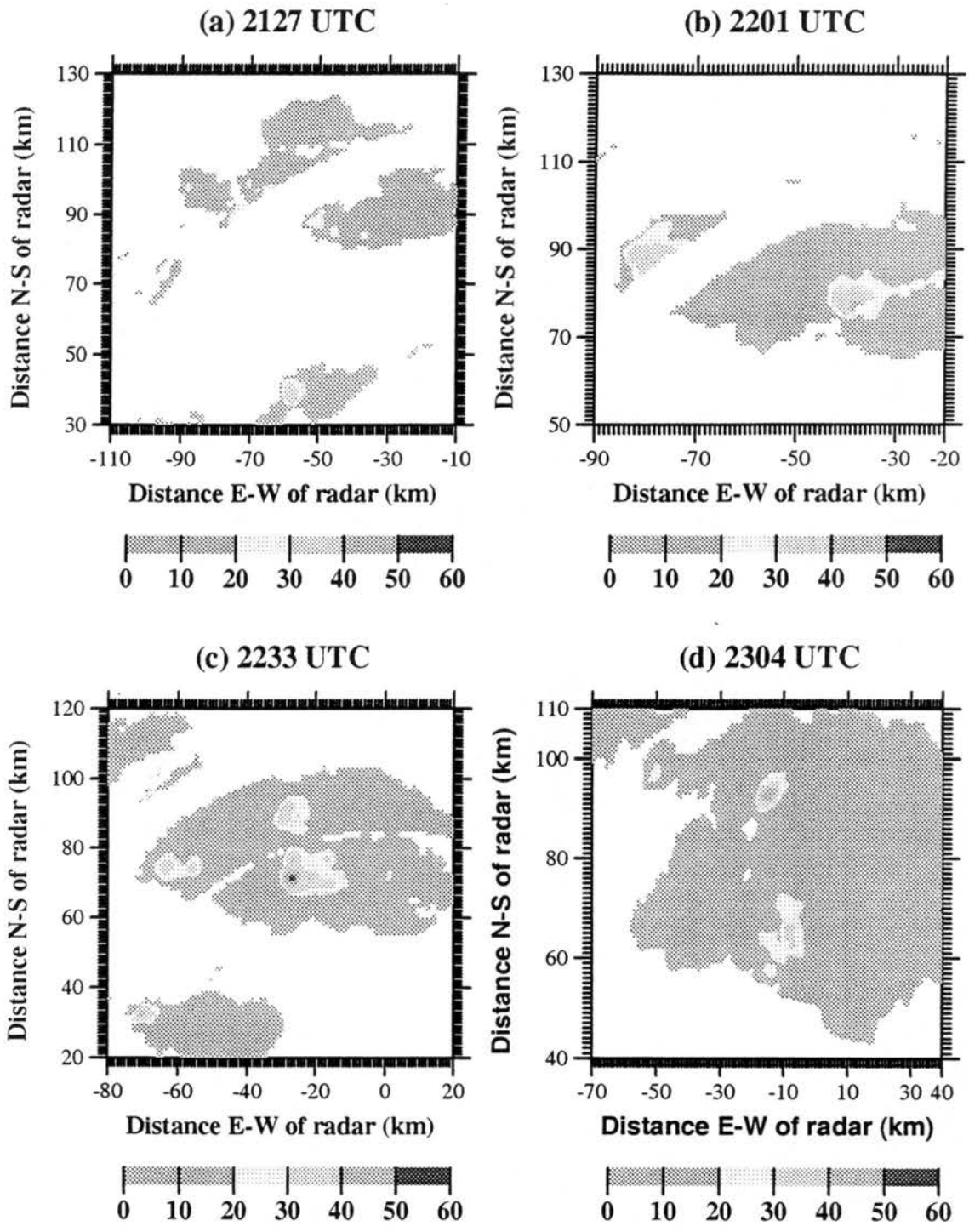

Figure 3.9 (a-d) Horizontal radar reflectivity cross sections at height of 9 km from the CSU-CHILL radar for: a) 2127 UTC; July 12, 1996; b) 2201 UTC; July 12, 1996; c) 2233 UTC; July 12, 1996; d) 2304 UTC; July 12, 1996. Notice changes in scale.

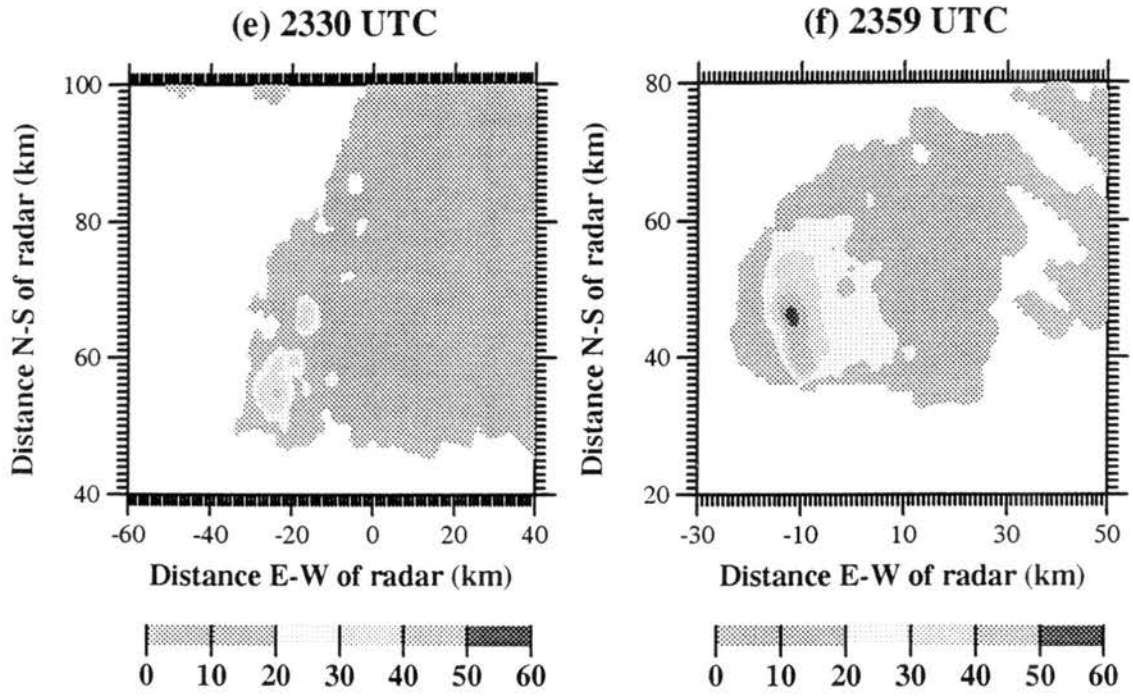

Figure 3.9 (e-f) Horizontal radar reflectivity cross sections at height of 9 km from the CSU-CHILL radar for: e) 2330 UTC; July 12, 1996; f) 2359 UTC; July 12, 1996. Notice changes in scale.

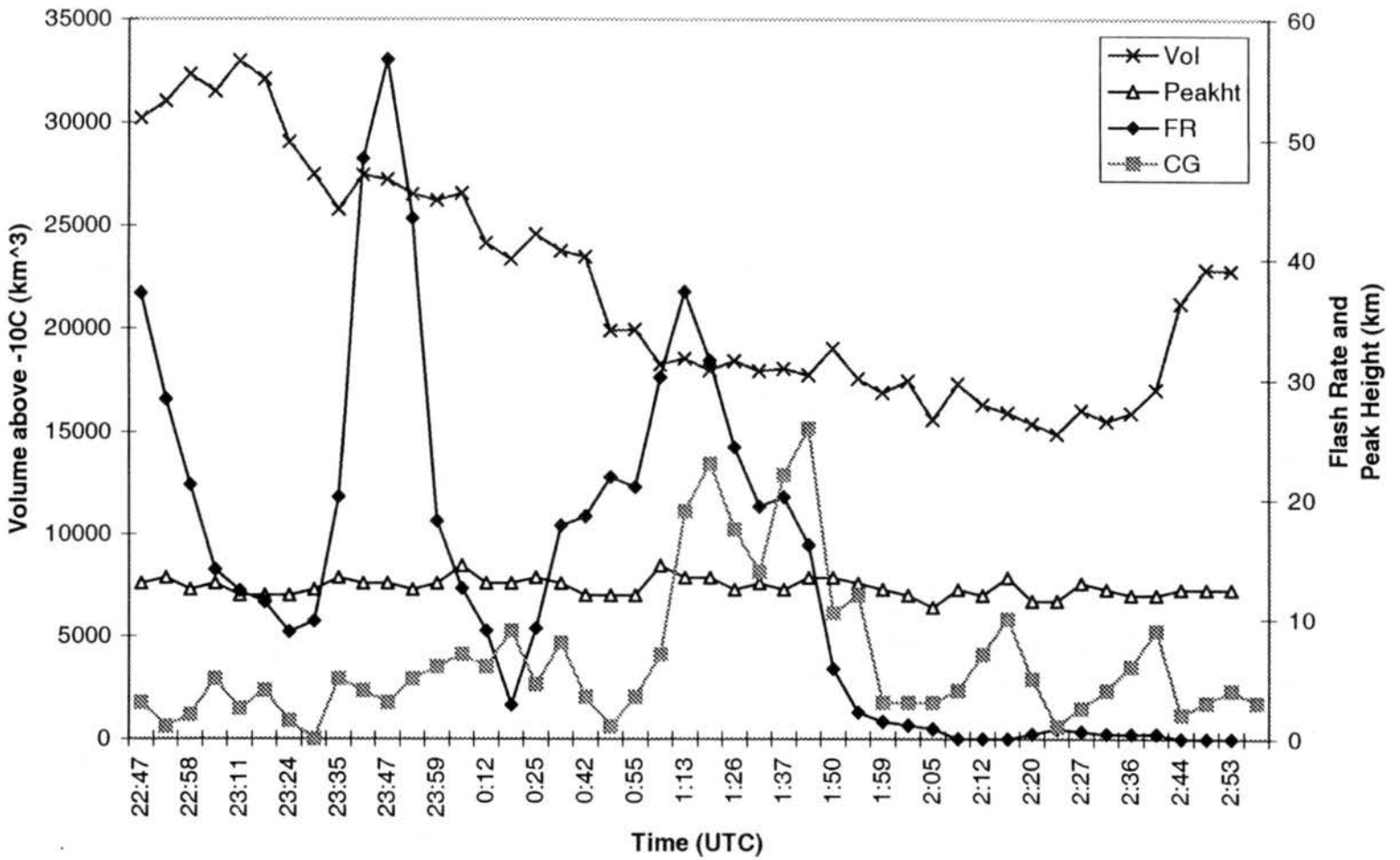

Figure 3.10 (a) Time series of radar and lightning variables: 2122 July 12, 1996 through 0257 UTC July 13, 1996. Radar variables calculated using 0 dBZ and -10°C thresholds. Flash rates are five minute averages.

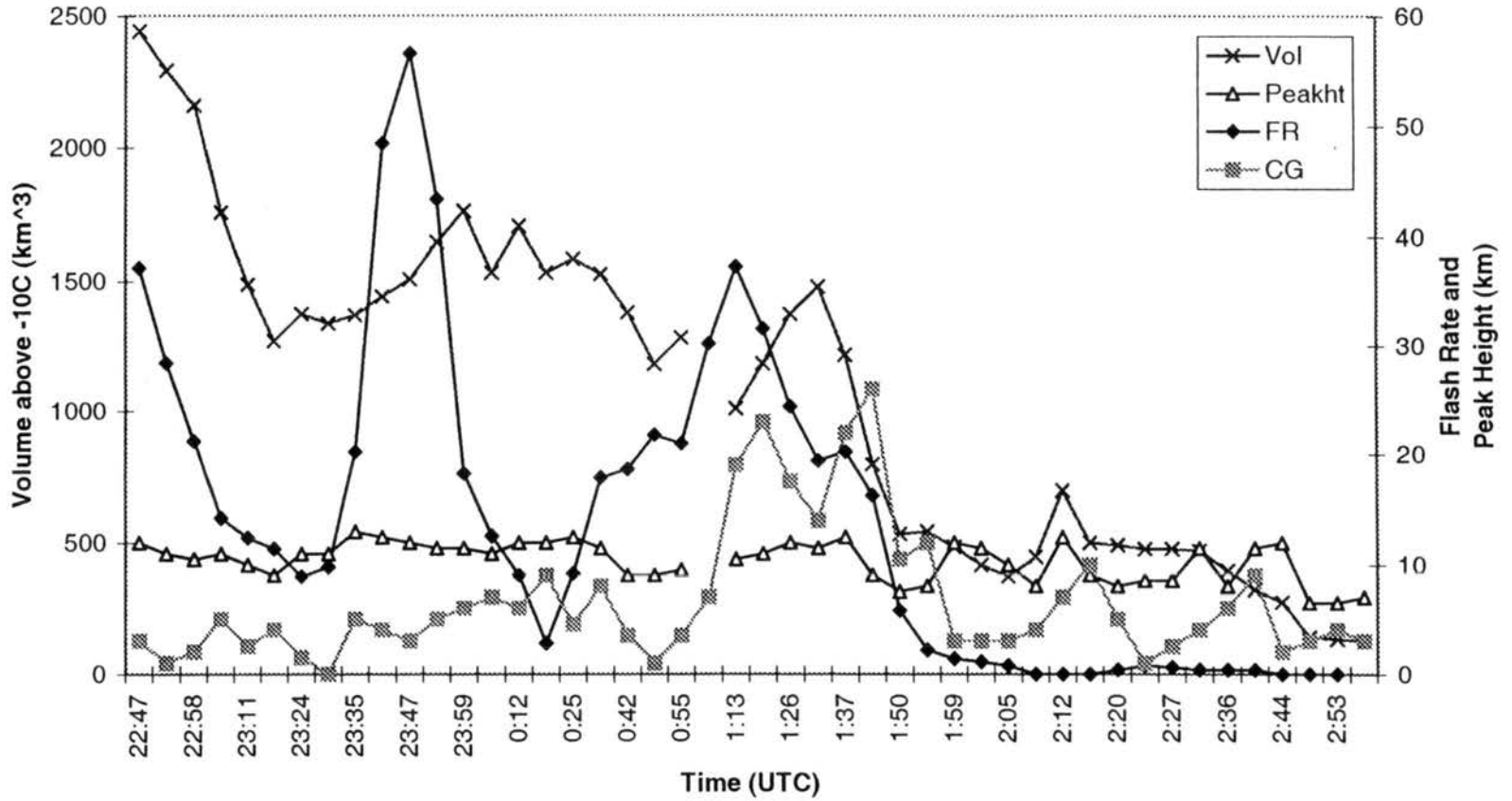

Figure 3.10 (b) Time series of radar and lightning variables: 2122 July 12, 1996 through 0257 UTC July 13, 1996. Radar variables calculated using 30 dBZ and -10°C thresholds. Flash rates are five minute averages.

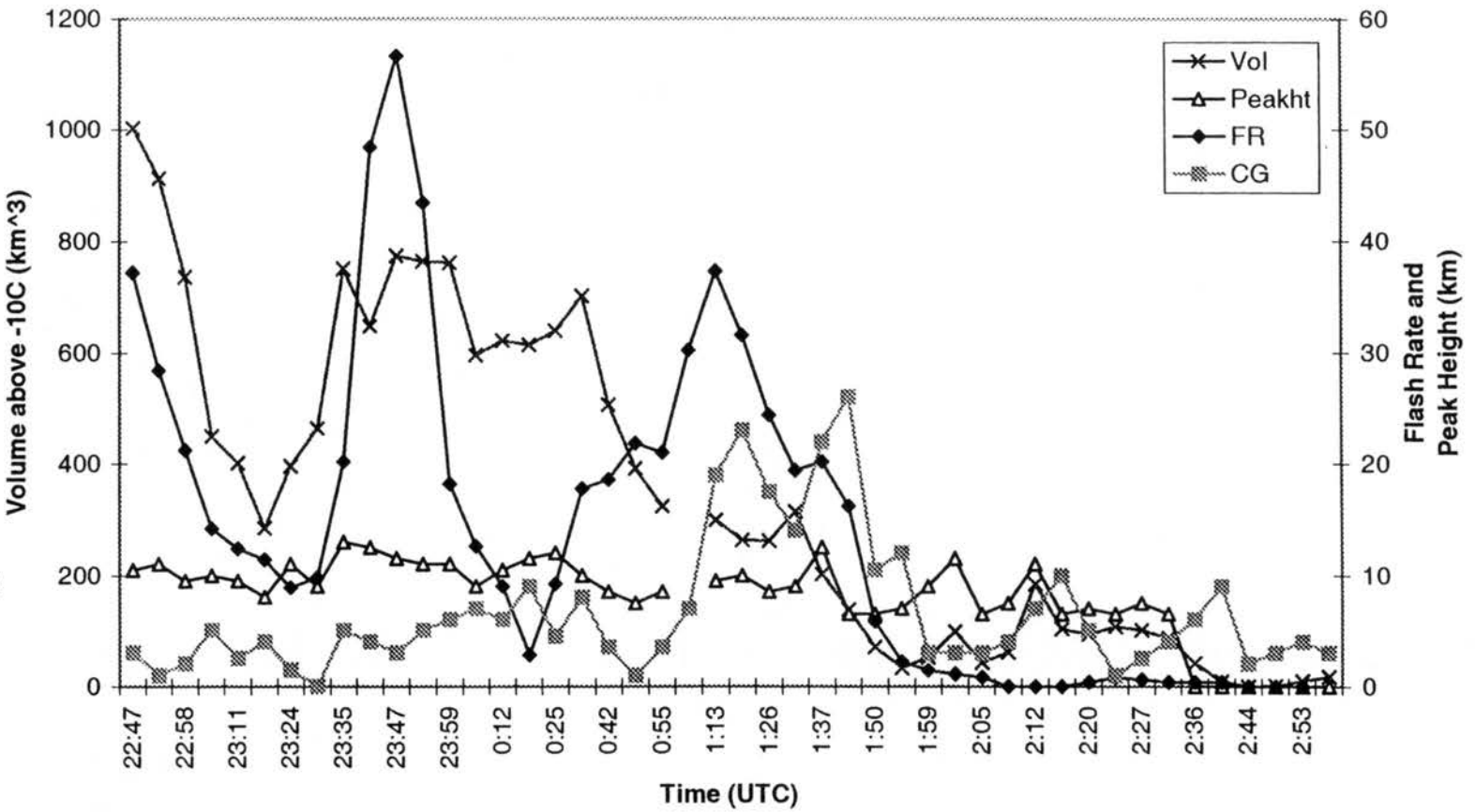

Figure 3.10 (c) Time series of radar and lightning variables: 2122 July 12, 1996 through 0257 UTC July 13, 1996. Radar variables calculated using 40 dBZ and -10°C thresholds. Flash rates are five minute averages.

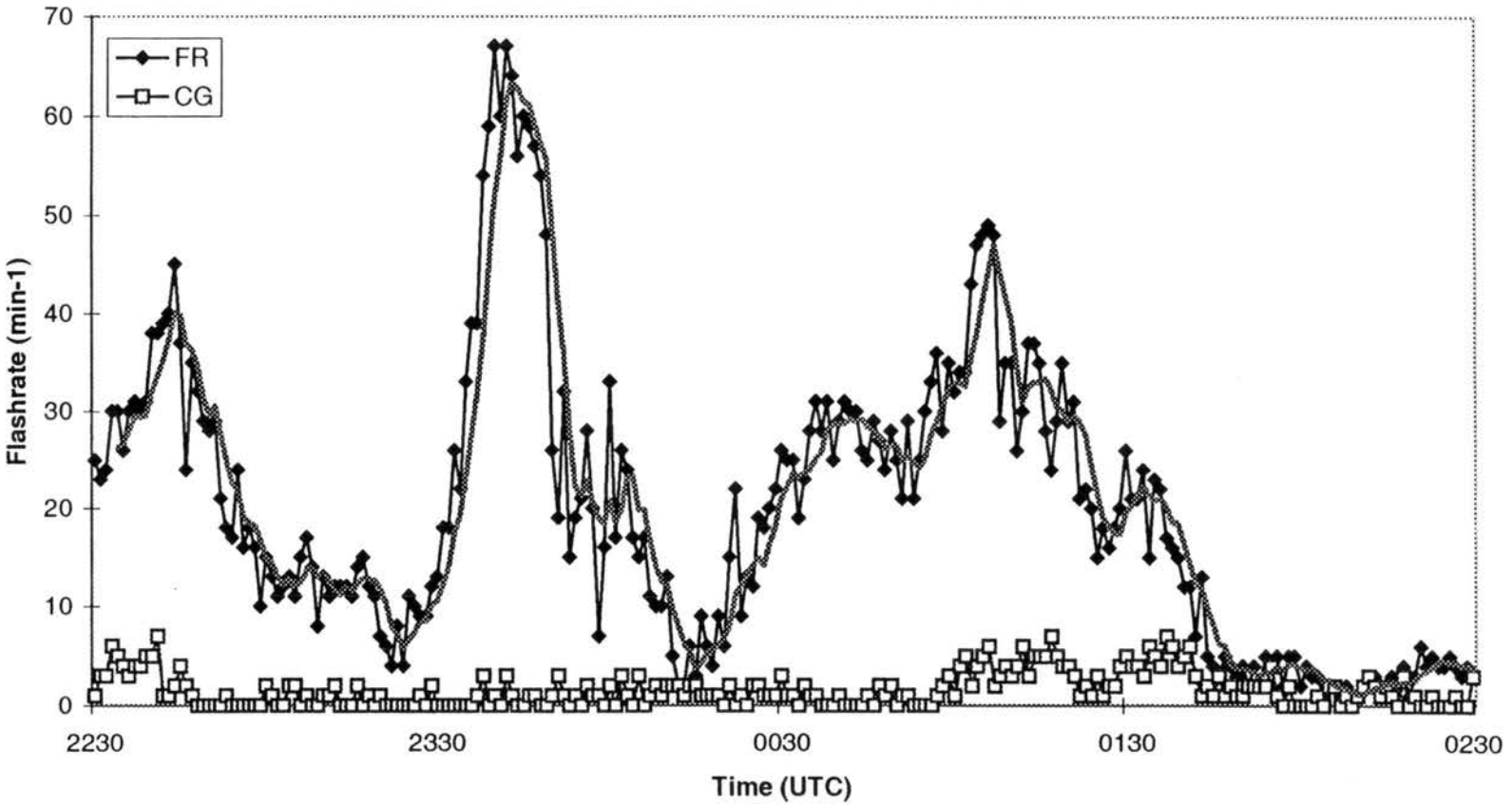

Figure 3.11 Time series of lightning flashrates from 12 July 1996 case. FR indicates total flash rate (min^{-1}). Five minute moving average of FR shown in thick gray line. CG indicates cloud-to-ground flash rate (min^{-1}).

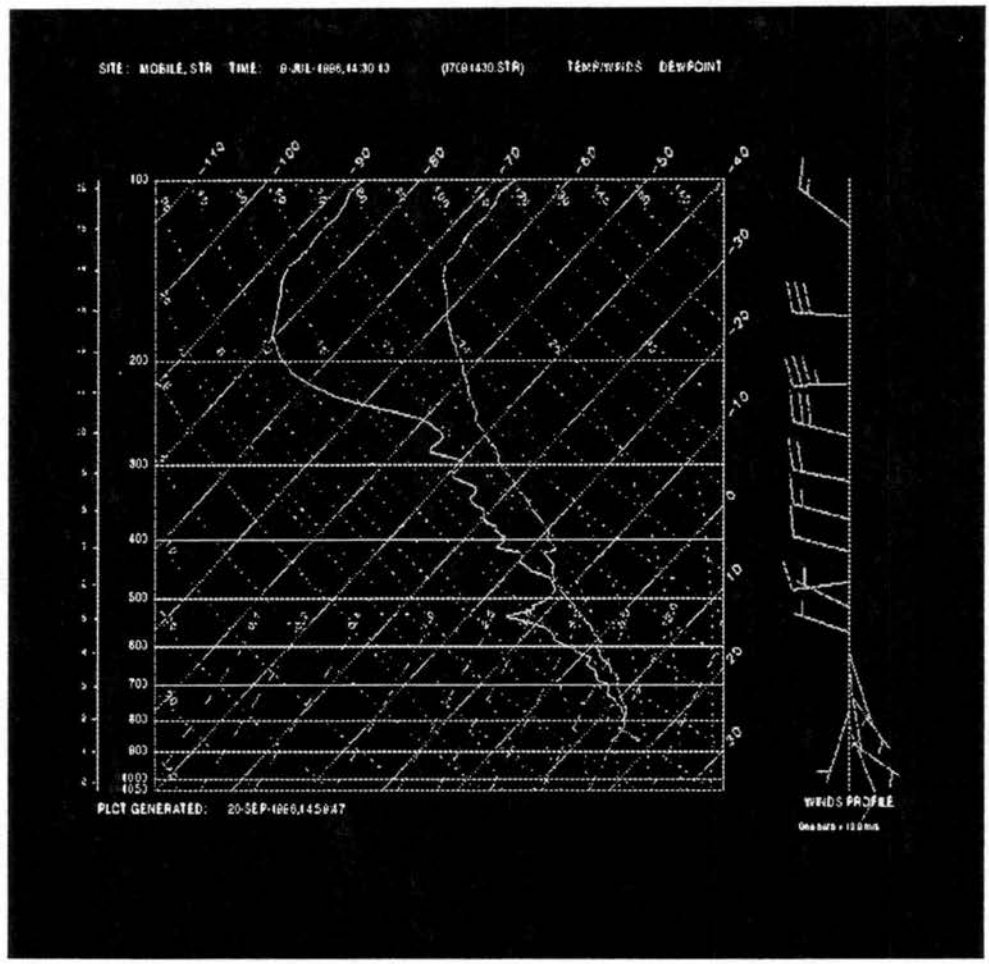

Figure 3.12 Mobile CLASS sounding from 2030 UTC 9 July 1996.

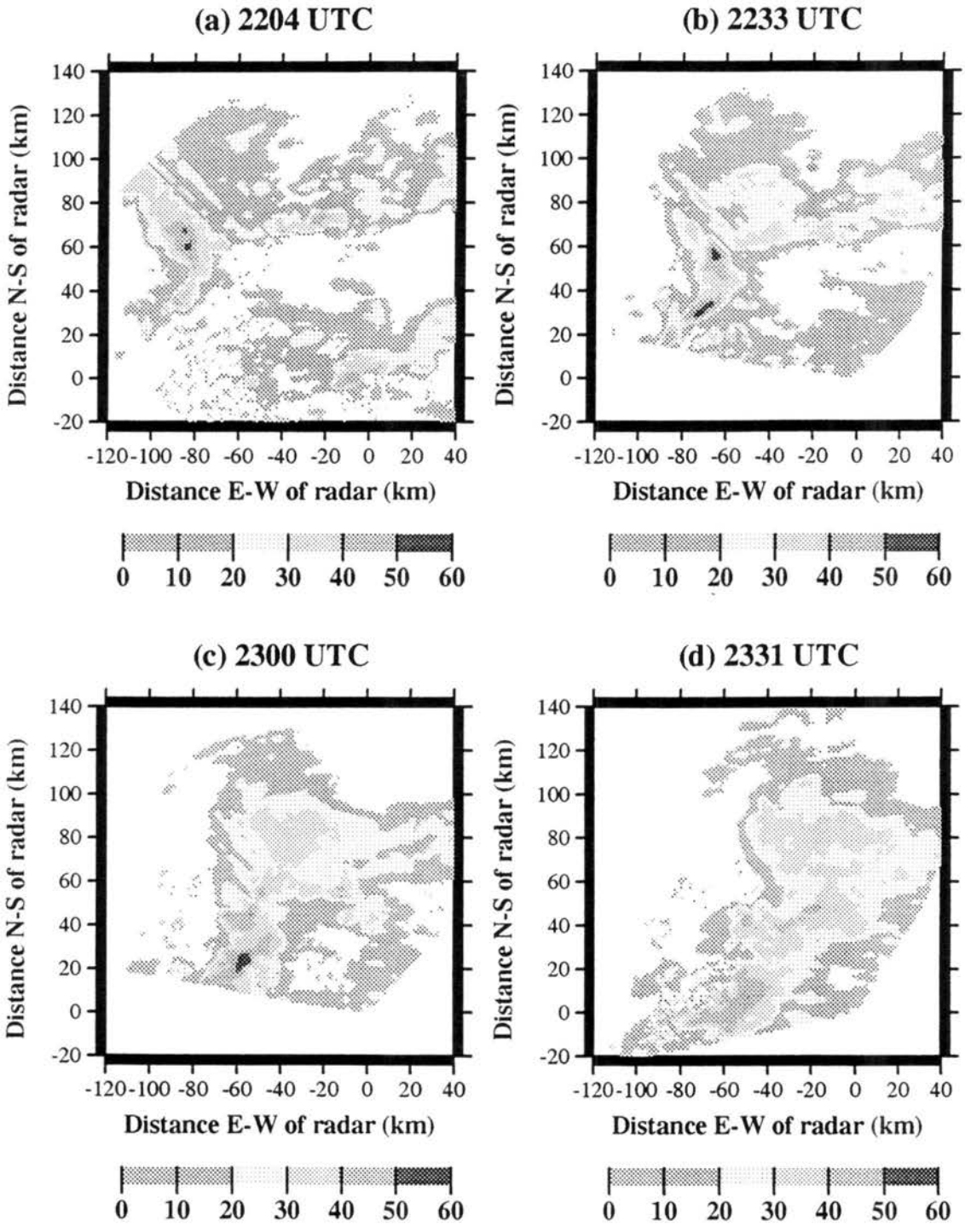

Figure 3.13 (a-d) Horizontal radar reflectivity cross sections at height of 1.5 km from the CSU-CHILL radar for: a) 2204 UTC; July 9, 1996; b) 2233 UTC; July 9, 1996; c) 2300 UTC; July 9, 1996; d) 2331 UTC; July 9, 1996. Notice changes in scale.

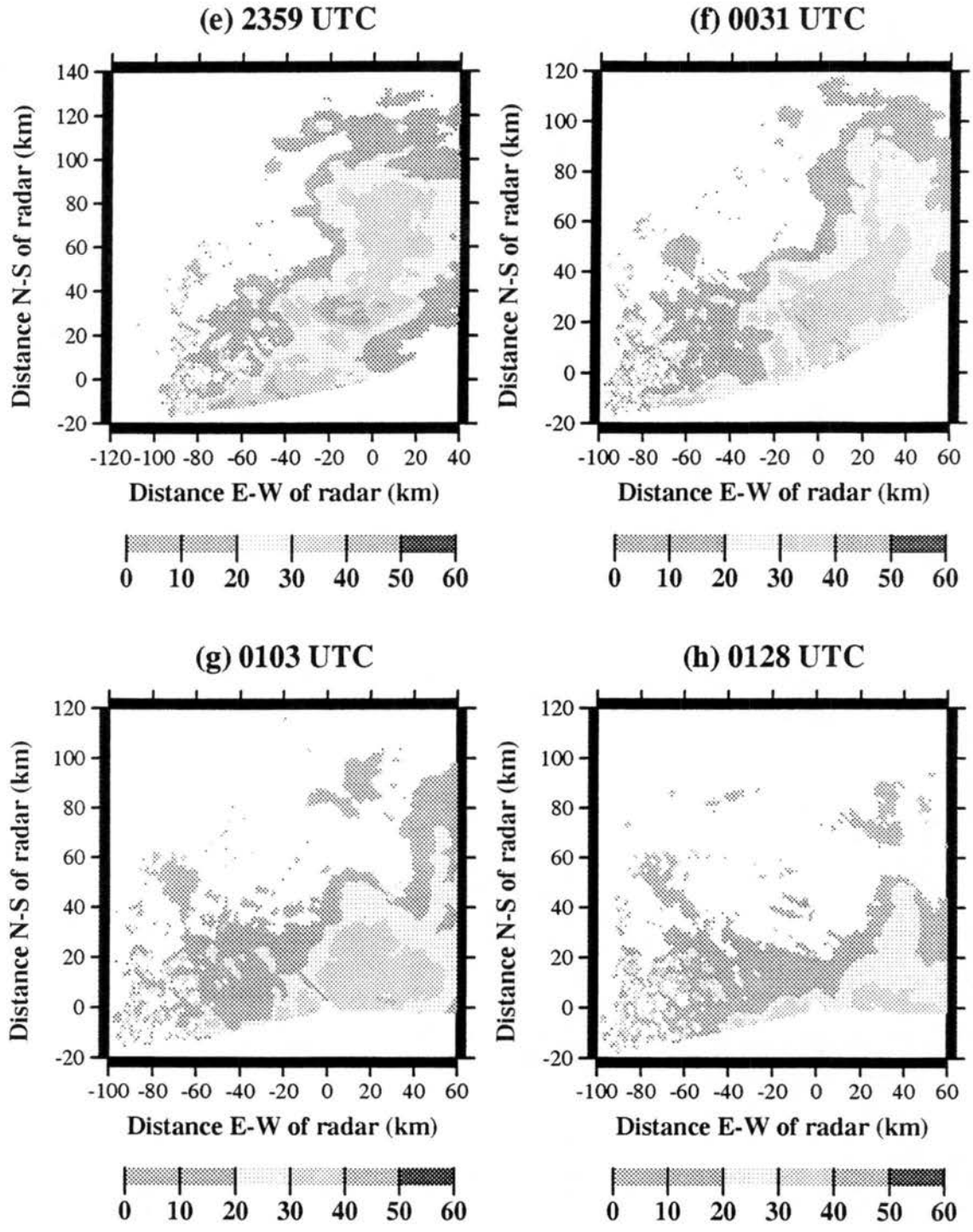

Figure 3.13 (e-h) Horizontal radar reflectivity cross sections at height of 1.5 km from the CSU-CHILL radar for: e) 2359UTC; July 9, 1996; f) 0031 UTC; July 10, 1996; g) 0103 UTC; July 10, 1996; h) 0128 UTC; July 10, 1996. Notice changes in scale.

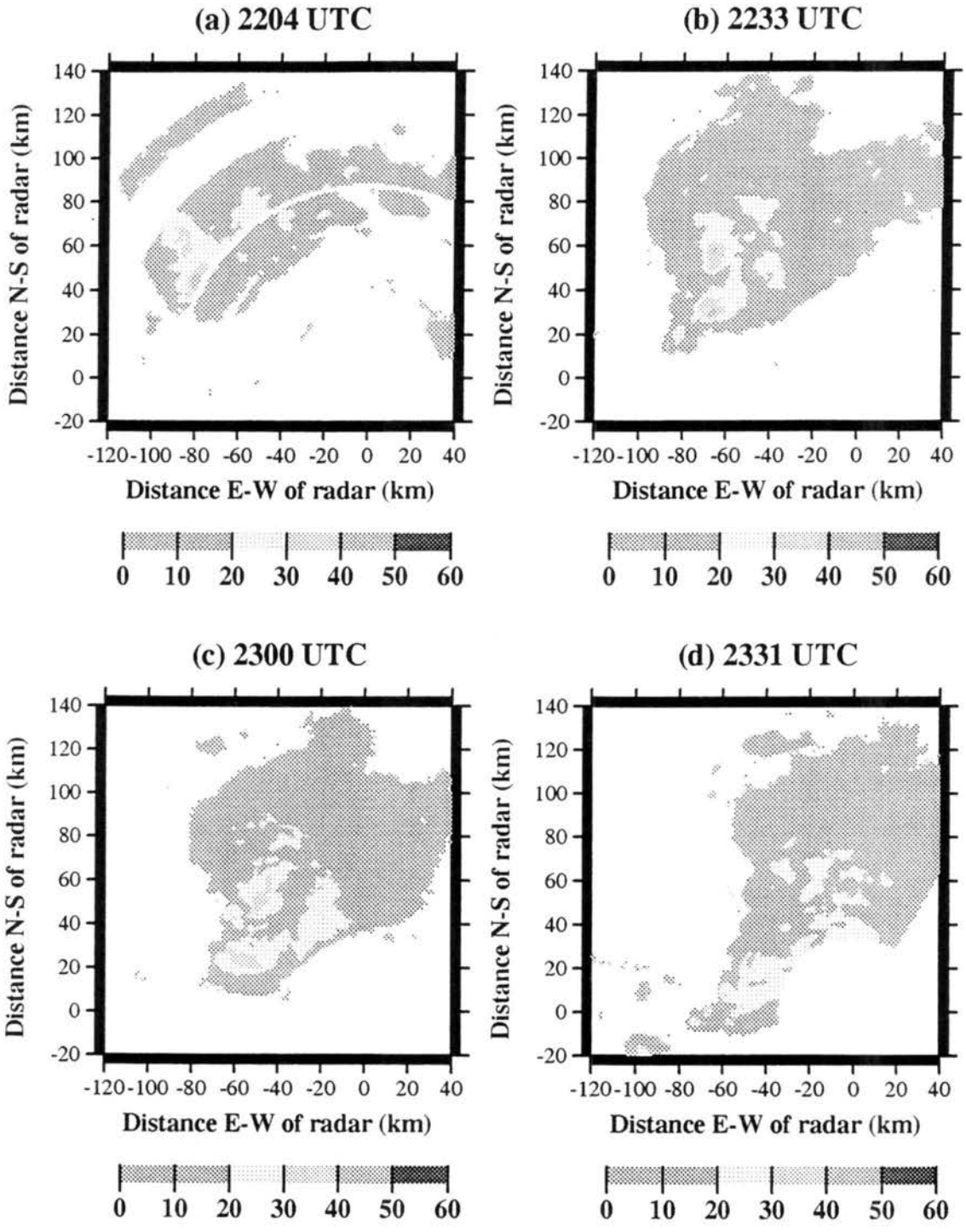

Figure 3.14 (a-d) Horizontal radar reflectivity cross sections at height of 7 km from the CSU-CHILL radar for: a) 2204 UTC; July 9, 1996; b) 2233 UTC; July 9. 1996; c) 2300 UTC; July 9, 1996; d) 2331 UTC; July 9, 1996. Notice changes in scale.

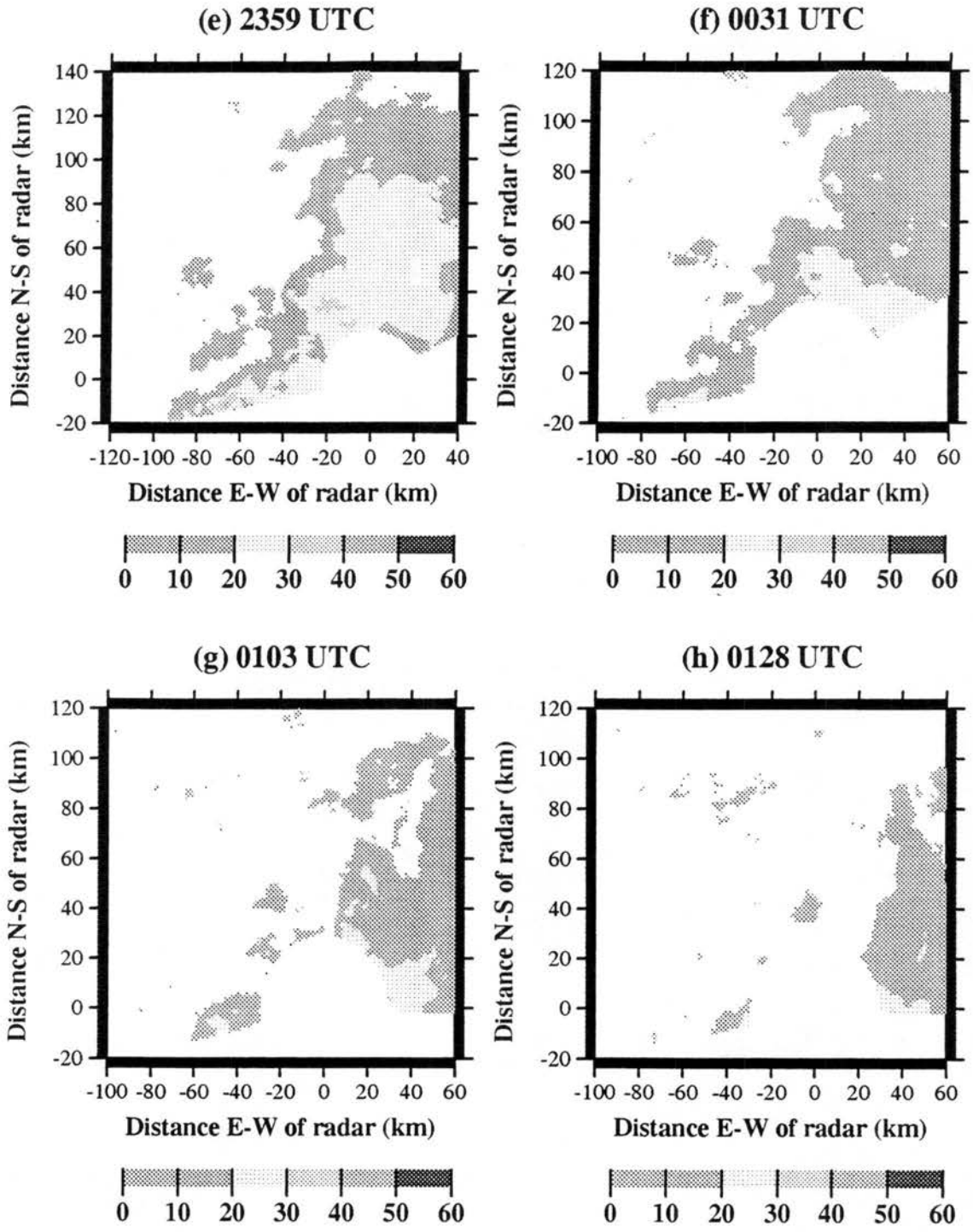

Figure 3.14 (e-h) Horizontal radar reflectivity cross sections at height of 5 km from the CSU-CHILL radar for: e) 2359 UTC; July 9, 1996; f) 0031 UTC; July 10, 1996; g) 0103 UTC; July 10, 1996; h) 0128 UTC; July 10, 1996. Notice changes in scale.

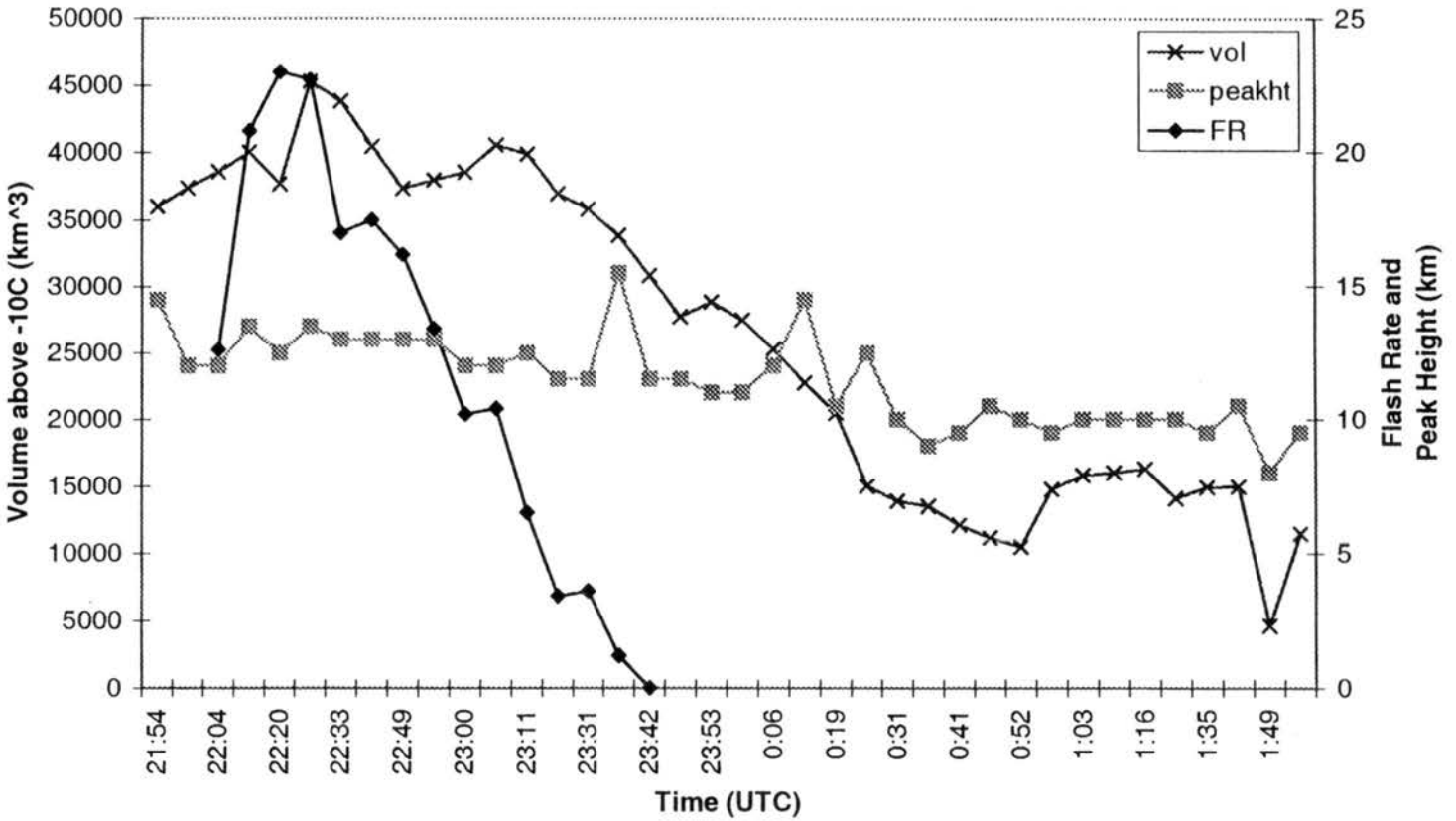

Figure 3.15 (a) Time series of radar and lightning variables: 2154 July 9, 1996 through 0153 UTC July 10, 1996. Radar variables calculated using 0 dBZ and -10°C thresholds. Flash rate (min^{-1}) is a five minute average.

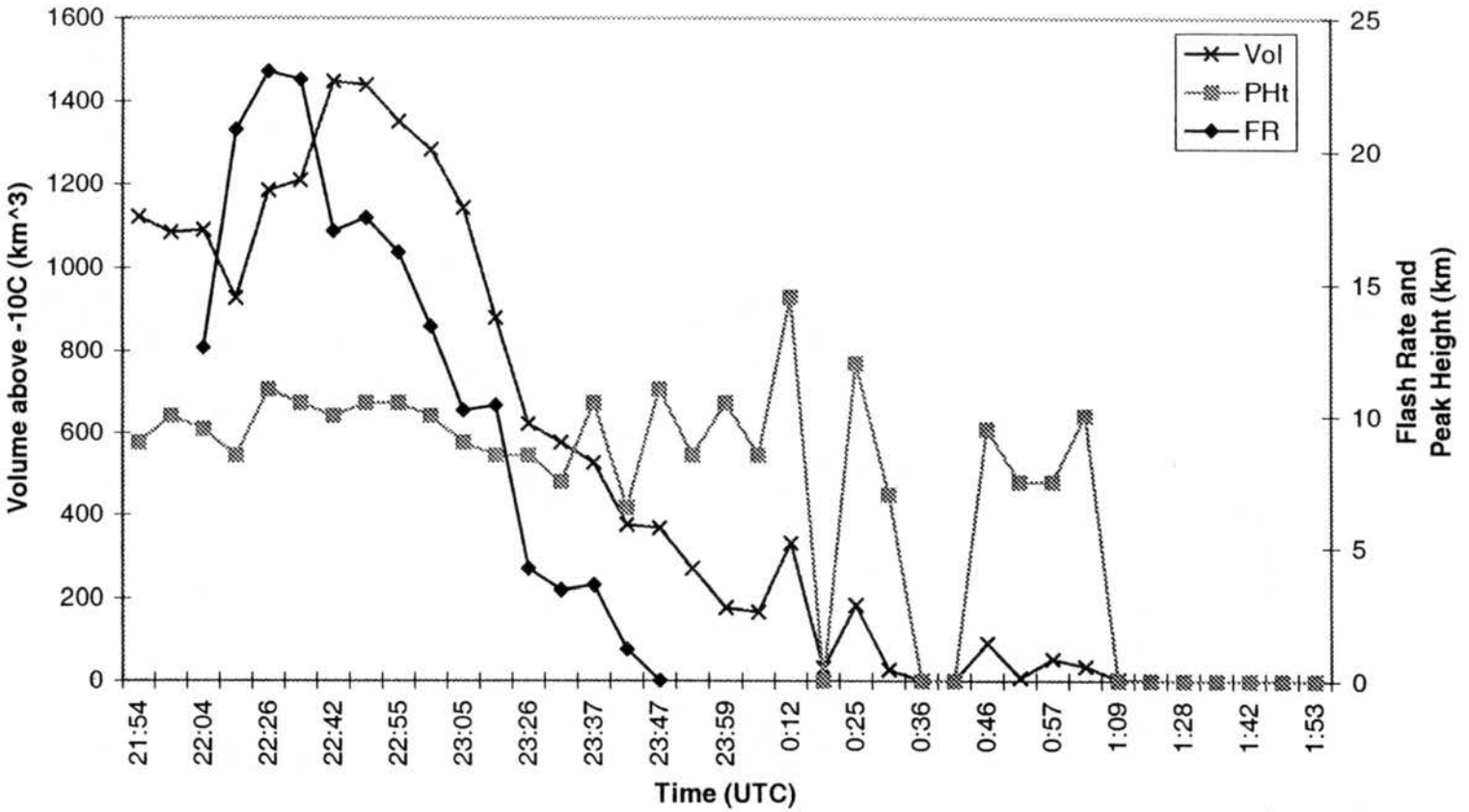

Figure 3.15 (b) Time series of radar and lightning variables: 2154 July 9, 1996 through 0153 UTC July 10, 1996. Radar variables calculated using 30 dBZ and -10°C thresholds. Flash rates (min^{-1}) is a five minute average.

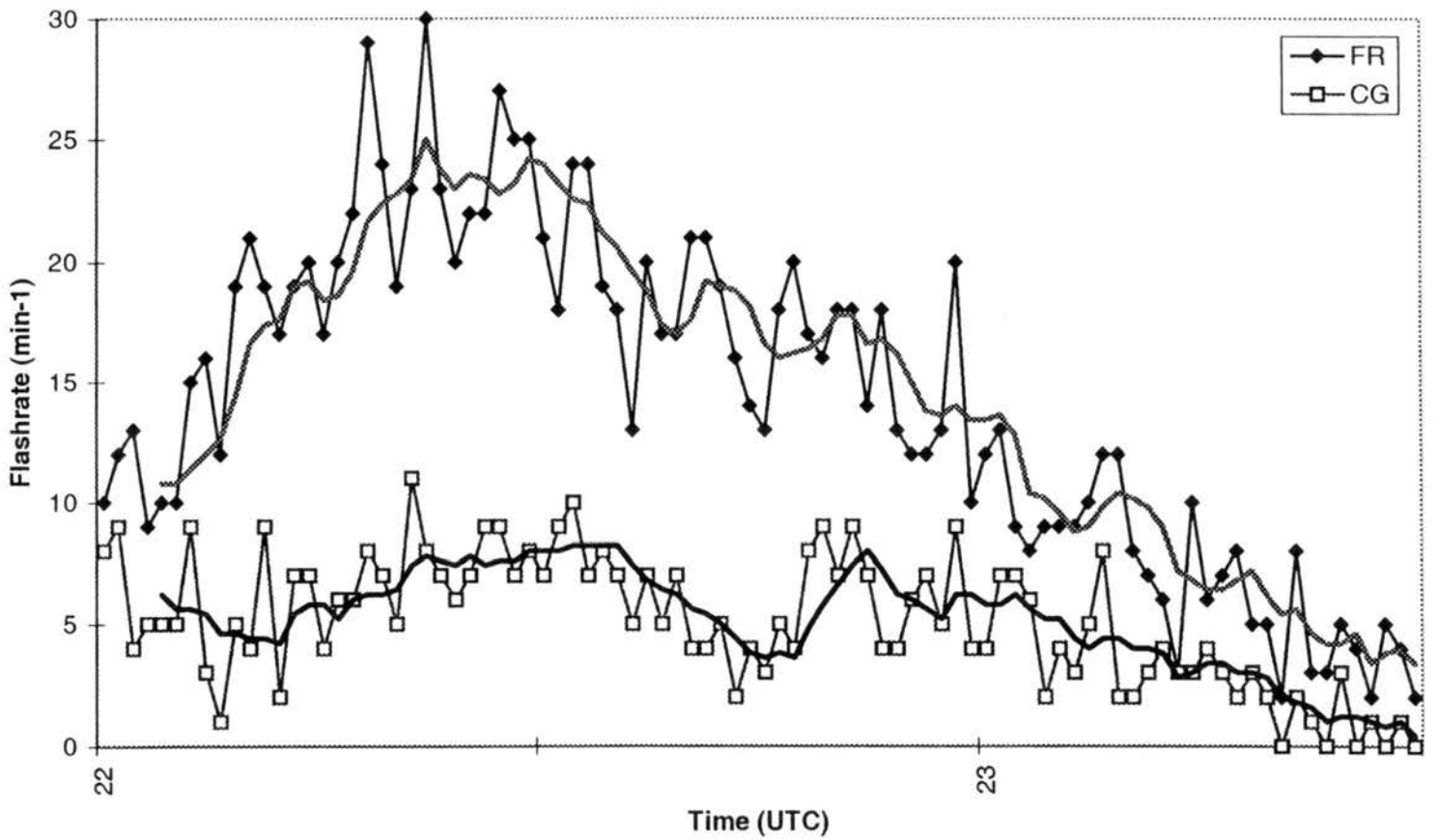

Figure 3.16 Time series of lightning flashrates from 9 July 1996 case. FR indicates total flash rate (min^{-1}). Five minute moving average of FR shown in thick gray line, while for CG in thick black line. CG indicates cloud-to-ground flash rate (min^{-1}).

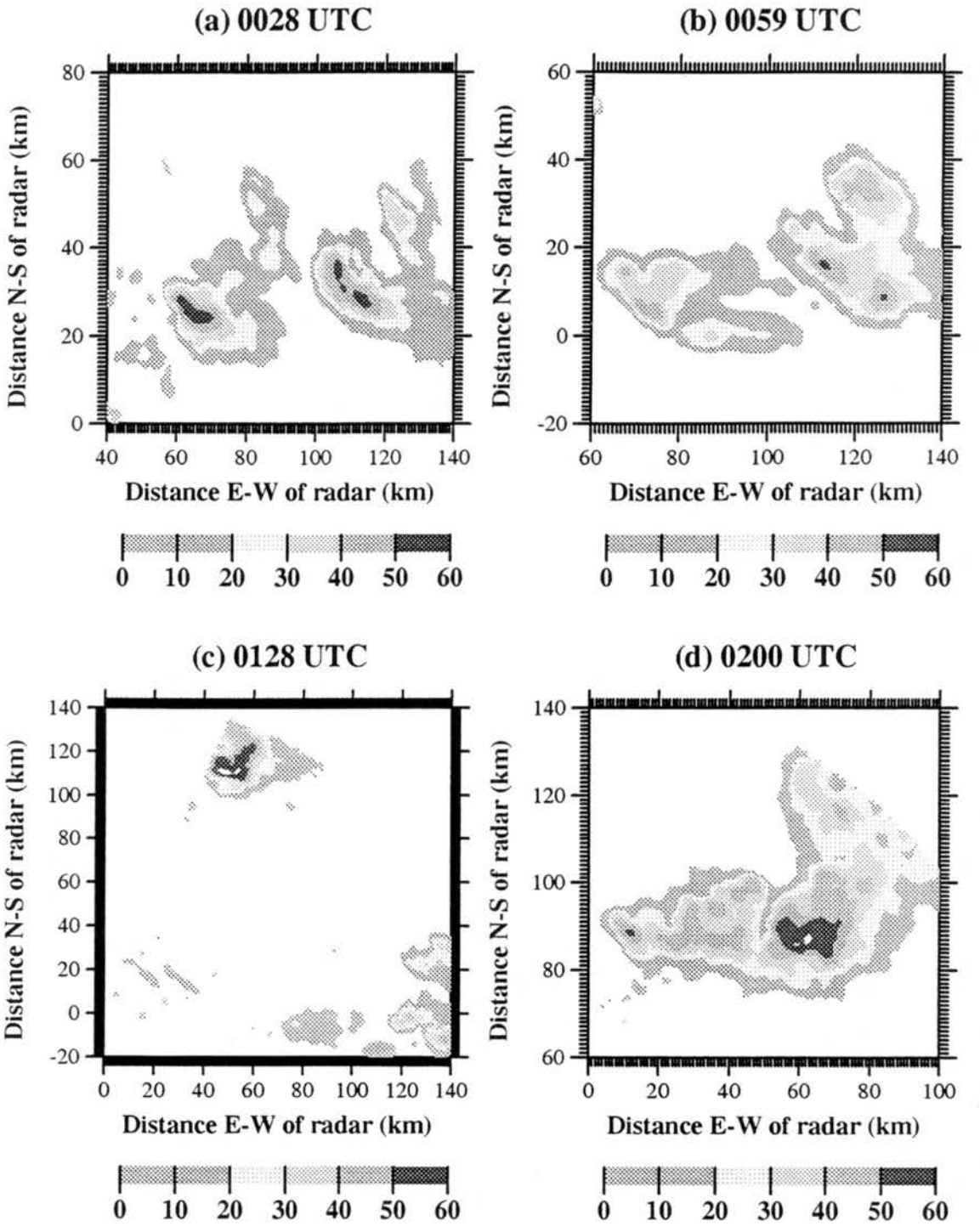

Figure 3.17 (a-d) Horizontal radar reflectivity cross sections at height of 1.5 km from the CSU-CHILL radar for: a) 0028 UTC; July 31, 1996; b) 0059 UTC; July 31, 1996; c) 0128 UTC; July 31, 1996; d) 0200 UTC; July 31, 1996. Notice changes in scale.

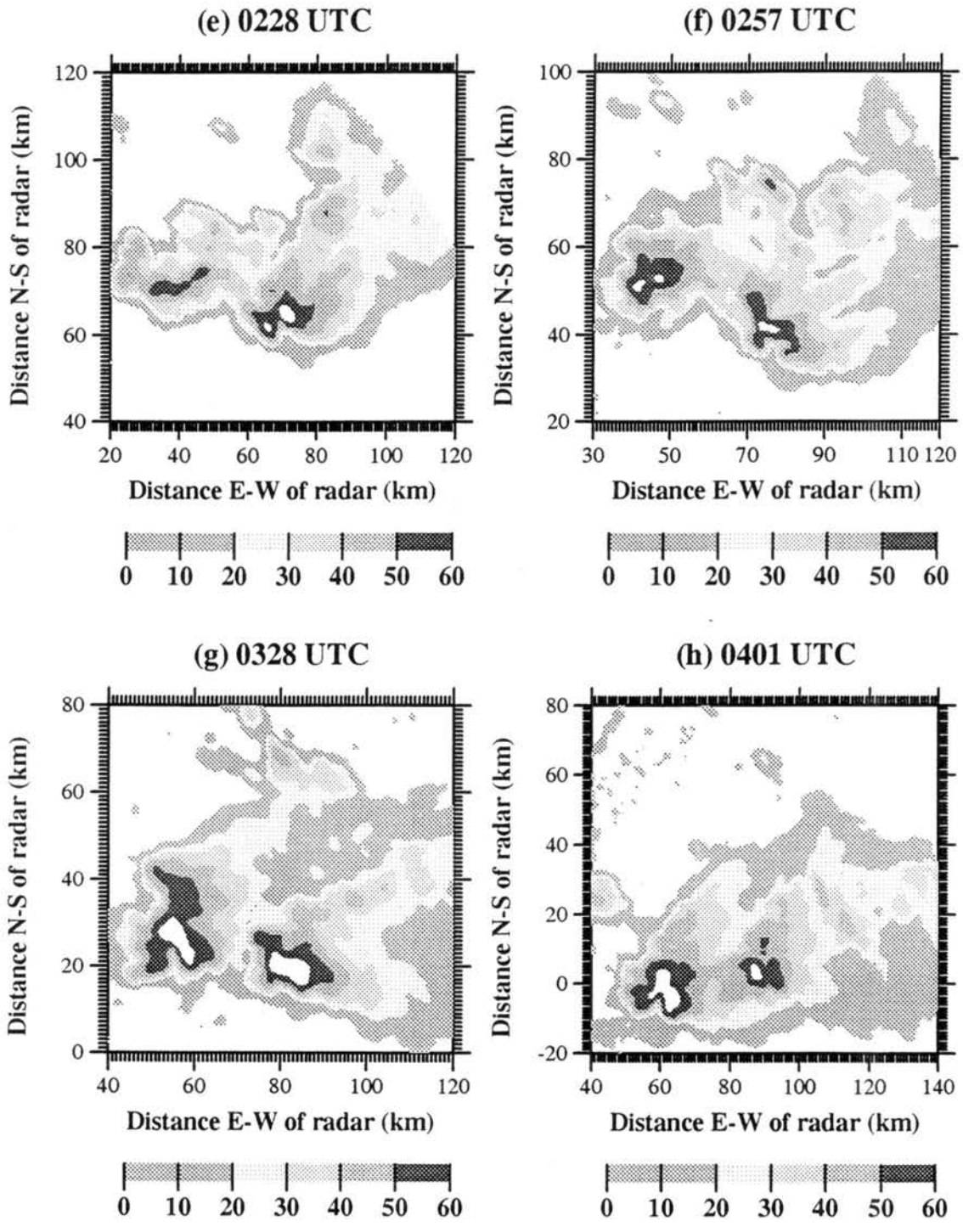

Figure 3.17 (e-h) Horizontal radar reflectivity cross sections at height of 1.5 km from the CSU-CHILL radar for: e) 0228 UTC; July 31, 1996; f) 0257 UTC; July 31, 1996; g) 0328 UTC; July 31, 1996; h) 0401 UTC; July 31, 1996. Notice changes in scale.

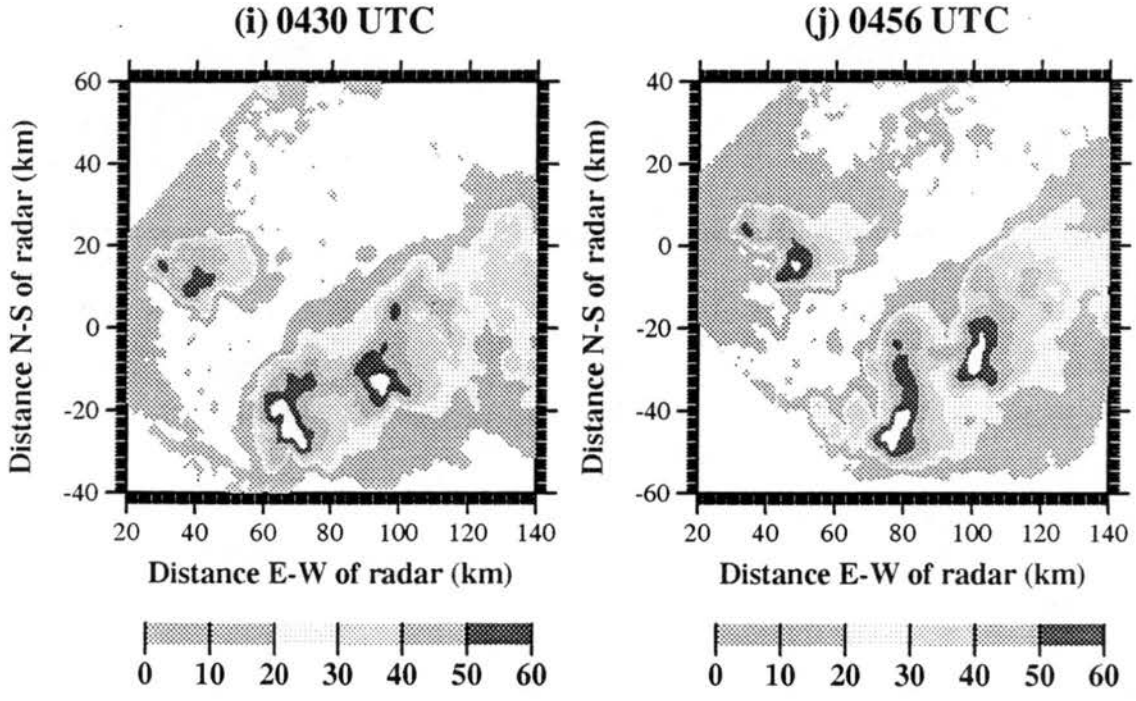

Figure 3.17 (i-j) Horizontal radar reflectivity cross sections at height of 1.5 km from the CSU-CHILL radar for: i) 0430 UTC; July 31, 1996; j) 0456 UTC; July 31, 1996. Notice changes in scale.

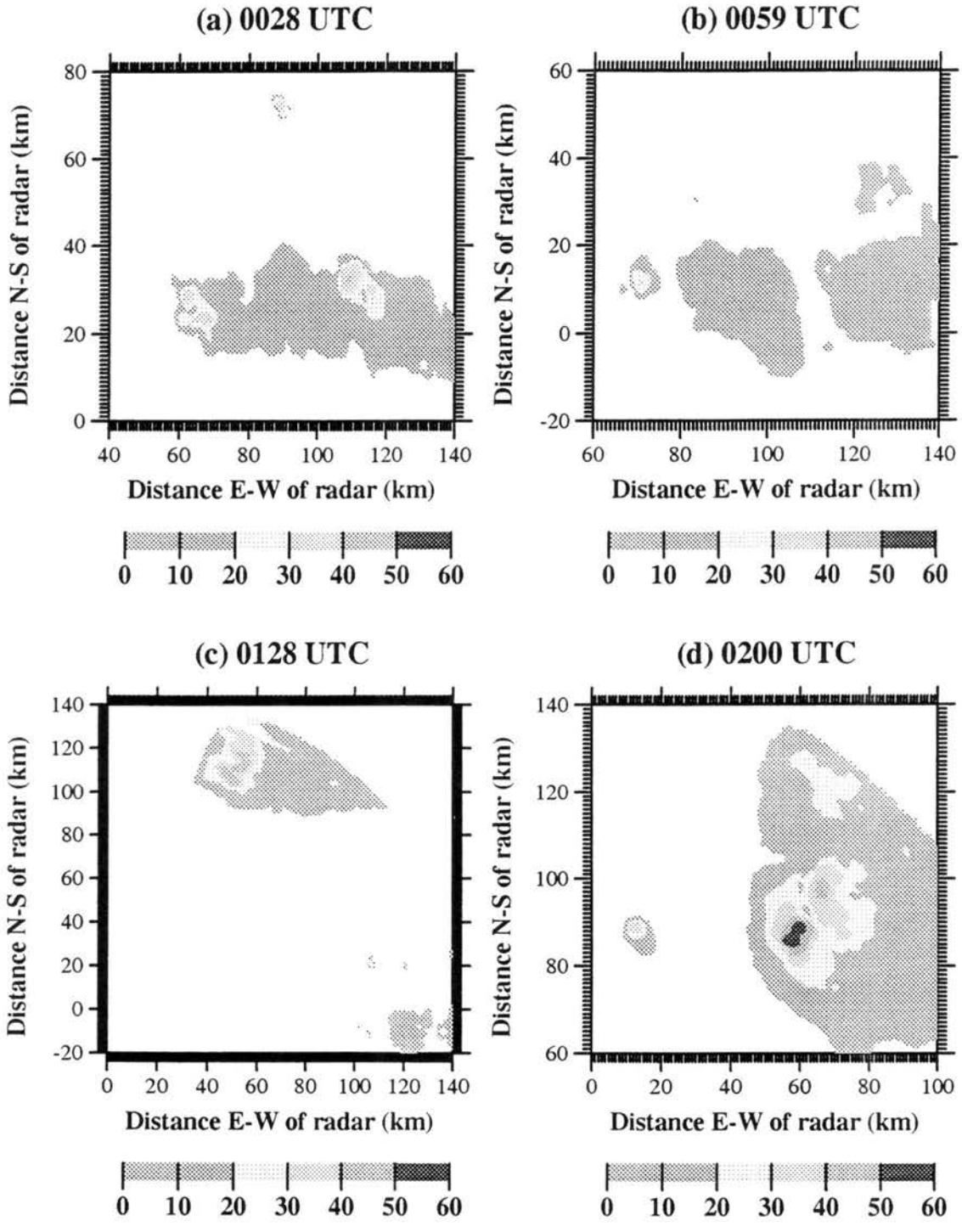

Figure 3.18 (a-d) Horizontal radar reflectivity cross sections at height of 9 km from the CSU-CHILL radar for: a) 0028 UTC; July 31, 1996; b) 0059 UTC; July 31, 1996; c) 0128 UTC; July 31, 1996; d) 0200 UTC; July 31, 1996. Notice changes in scale.

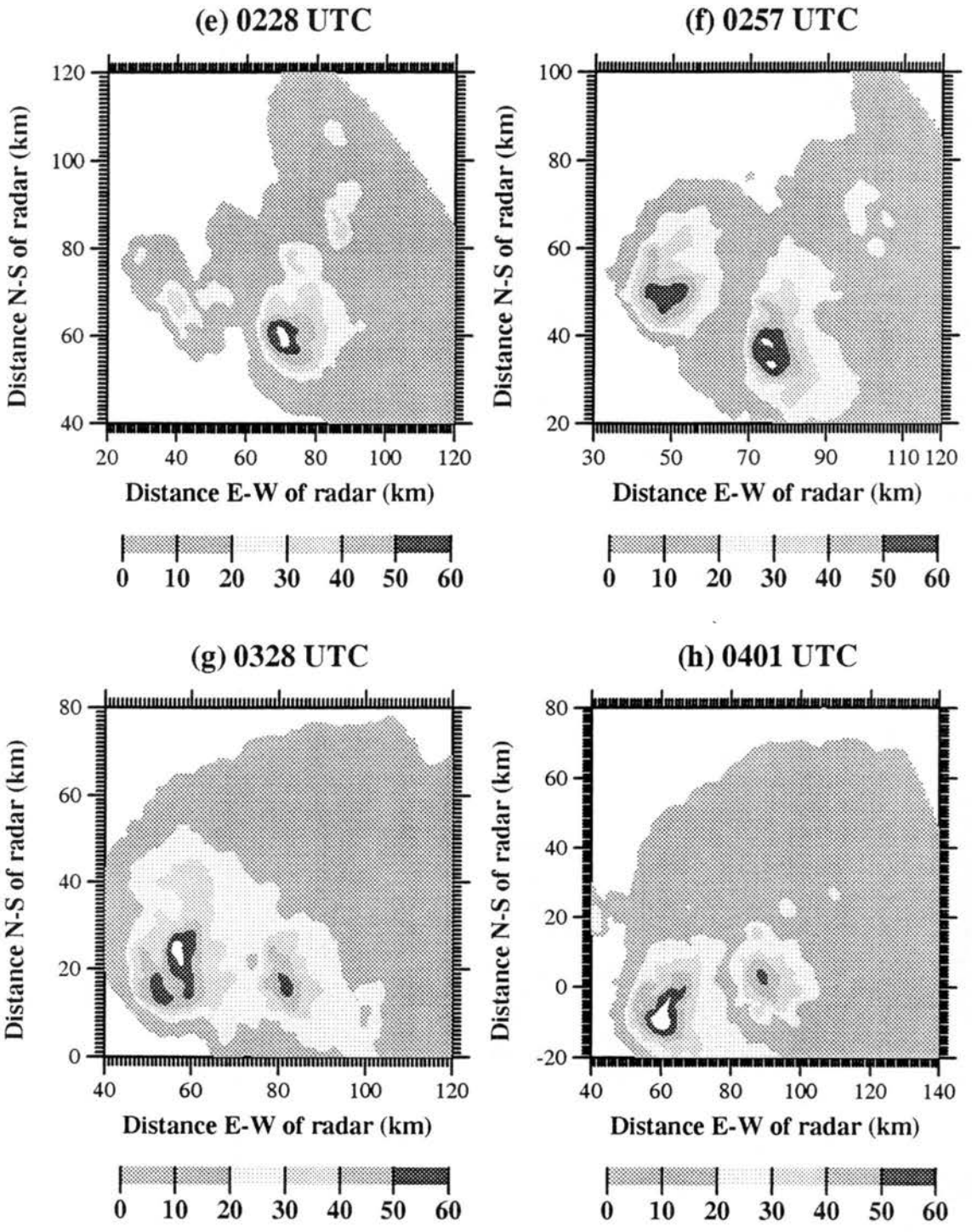

Figure 3.18 (e-h) Horizontal radar reflectivity cross sections at height of 9 km from the CSU-CHILL radar for: e) 0228 UTC; July 31, 1996; f) 0257 UTC; July 31, 1996; g) 0328 UTC; July 31, 1996; h) 0401 UTC; July 31, 1996. Notice changes in scale.

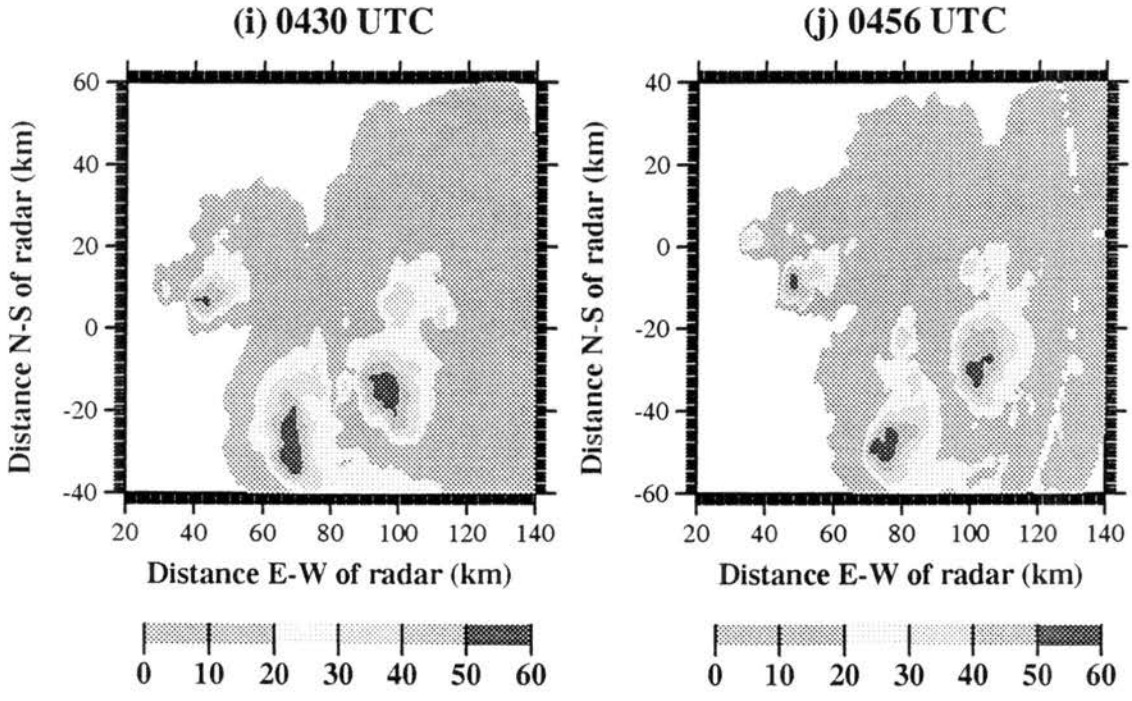

Figure 3.18 (i-j) Horizontal radar reflectivity cross sections at height of 9 km from the CSU-CHILL radar for: i) 0430 UTC; July 31, 1996; j) 0456 UTC; July 31, 1996. Notice changes in scale.

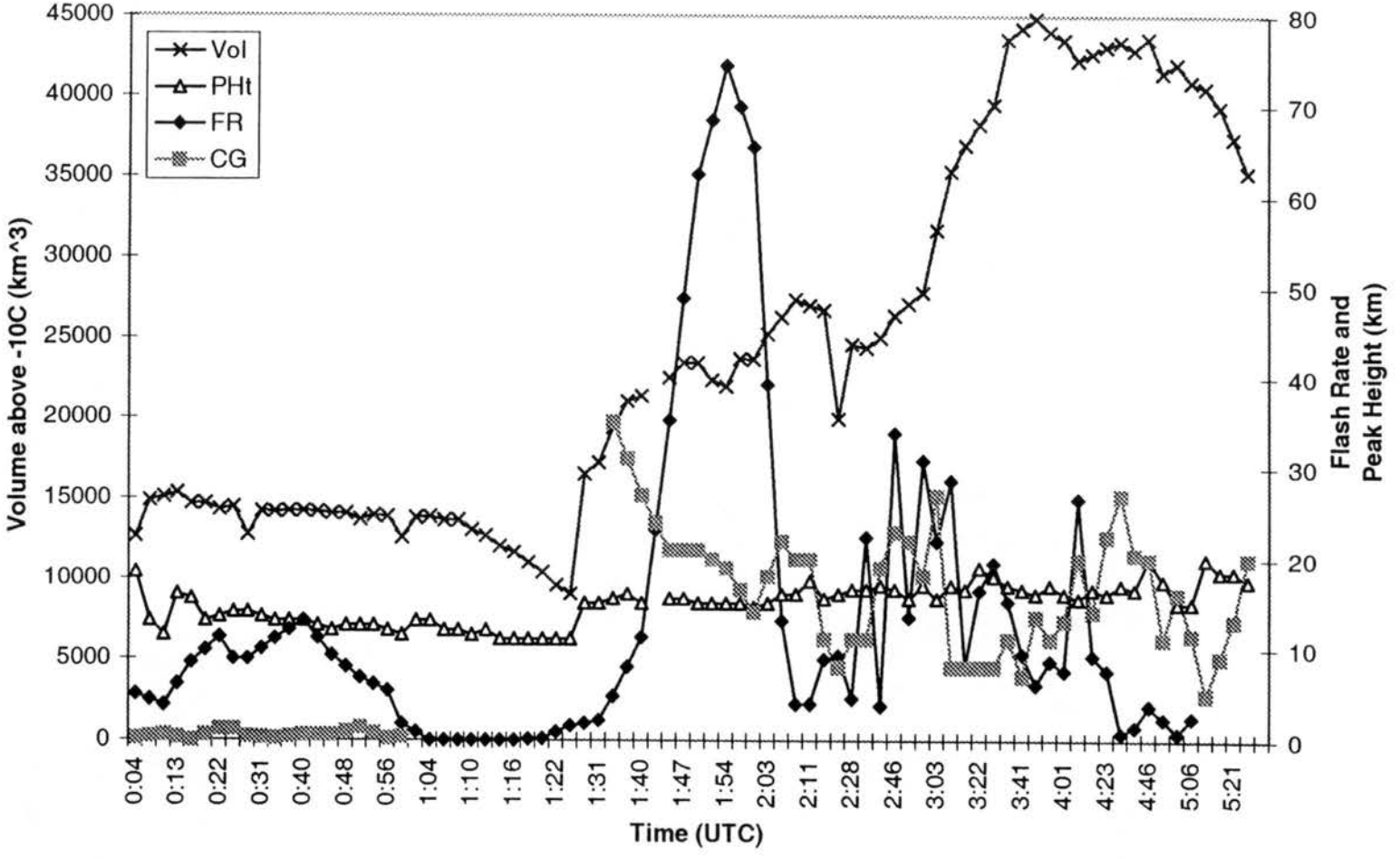

Figure 3.19(a) Time series of radar and lightning variables: 0004 July 31, 1996 through 0530 UTC July 31, 1996. Radar variables calculated using 0 dBZ and -10°C thresholds. Flash rates are five minute averages.

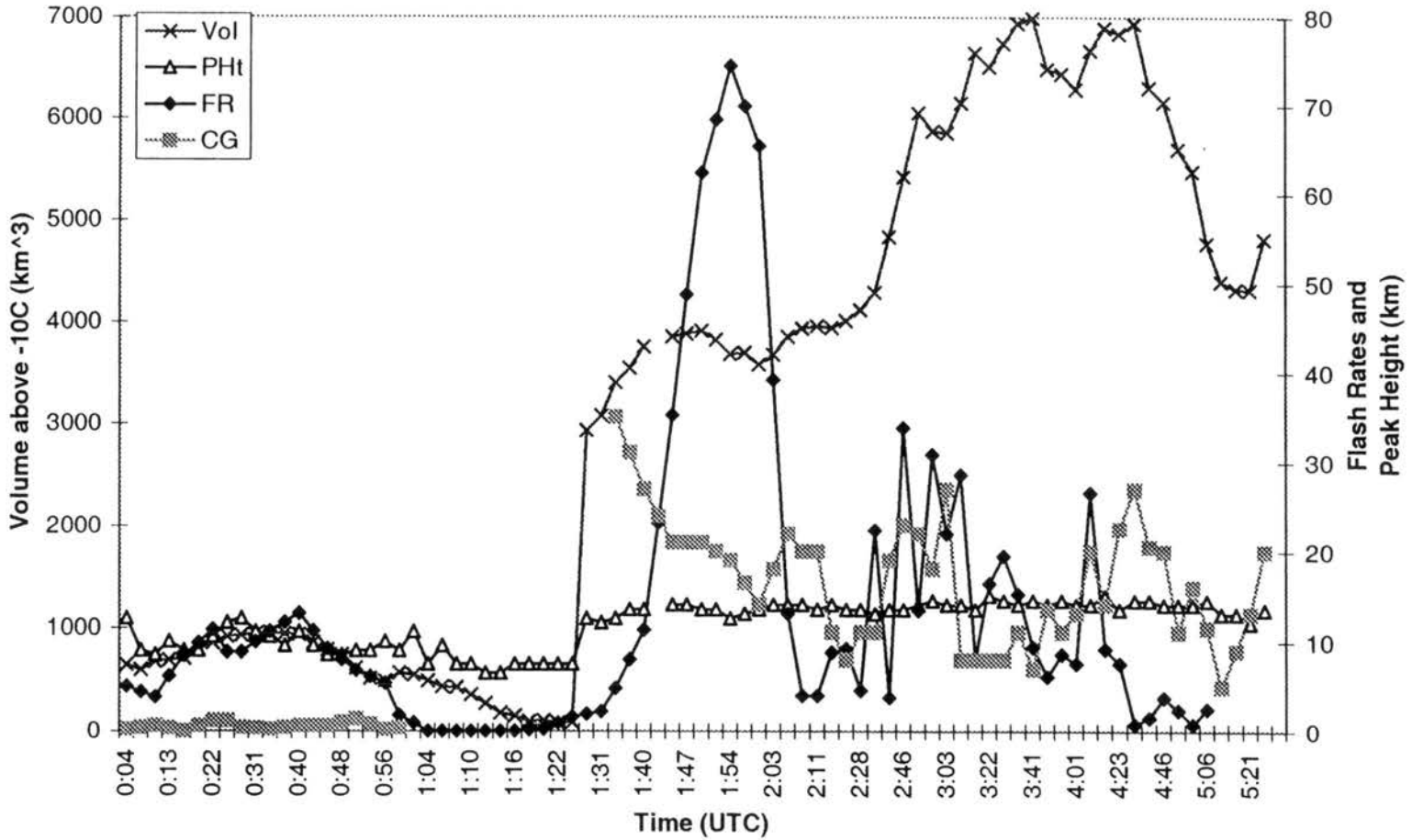

Figure 3.19(b) Time series of radar and lightning variables: 0004 July 31, 1996 through 0530 UTC July 31, 1996. Radar variables calculated using 30 dBZ and -10°C thresholds. Flash rates are five minute averages.

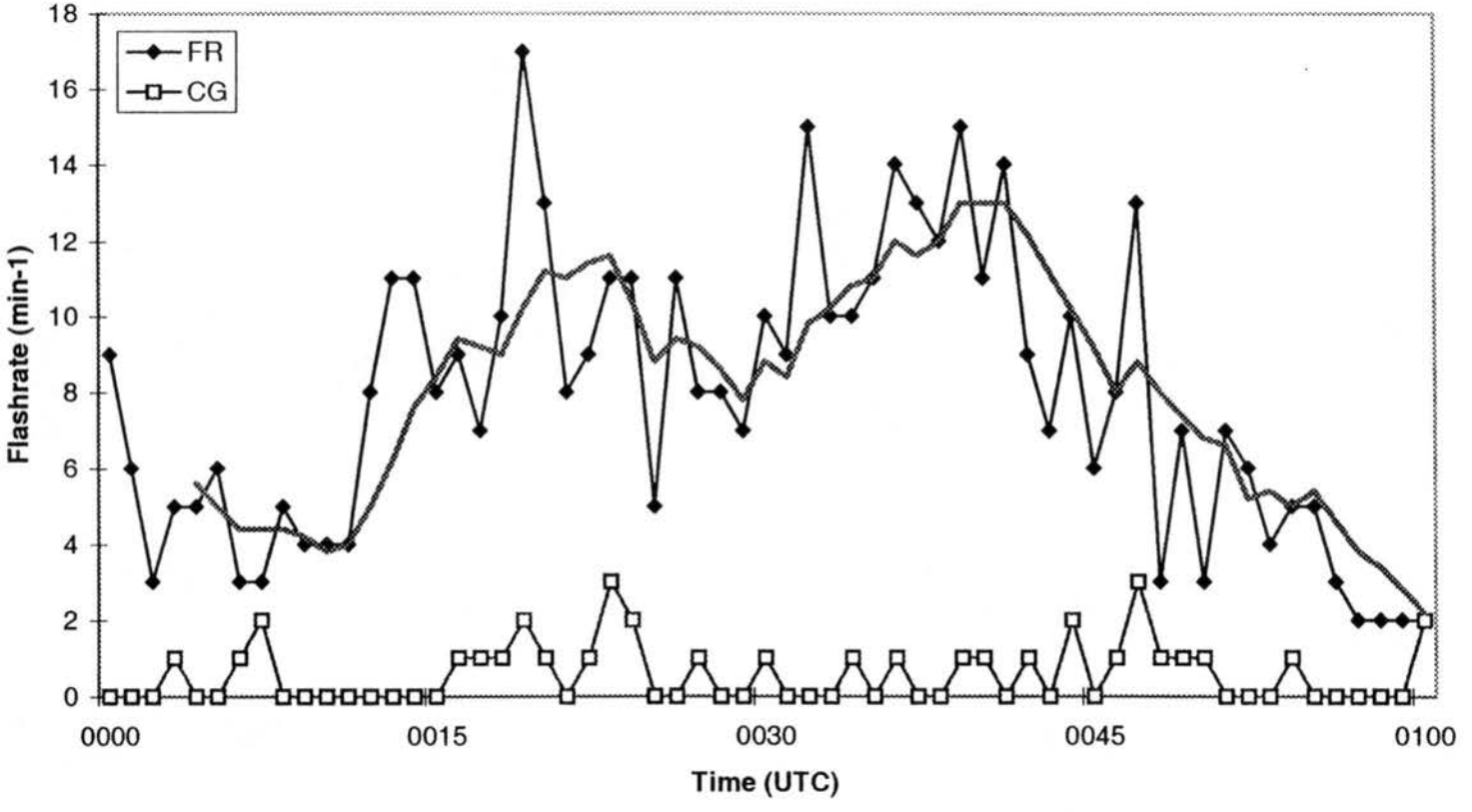

Figure 3.20(a) Time series of lightning flashrates from 30 July 1996 case, part a, 0000 to 0100 UTC. FR indicates total flash rate (min^{-1}). Five minute moving average of FR shown in thick gray line. CG indicates cloud-to-ground flash rate (min^{-1}).

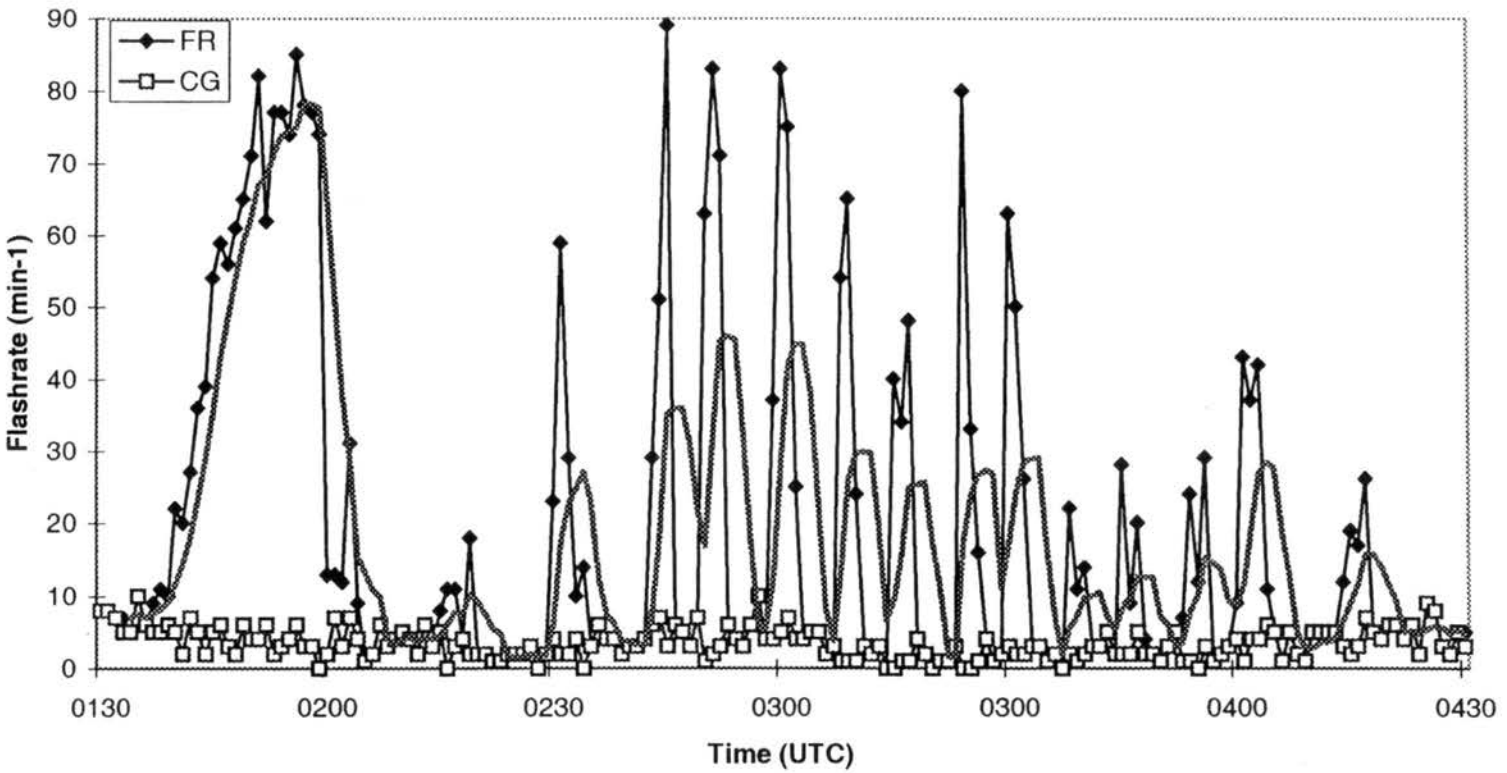

Figure 3.20(b) Time series of lightning flashrates from 30 July 1996 case, part b, 0130 to 0430 UTC. FR indicates total flash rate (min^{-1}). Five minute moving average of FR shown in thick gray line. CG indicates cloud-to-ground flash rate (min^{-1}).

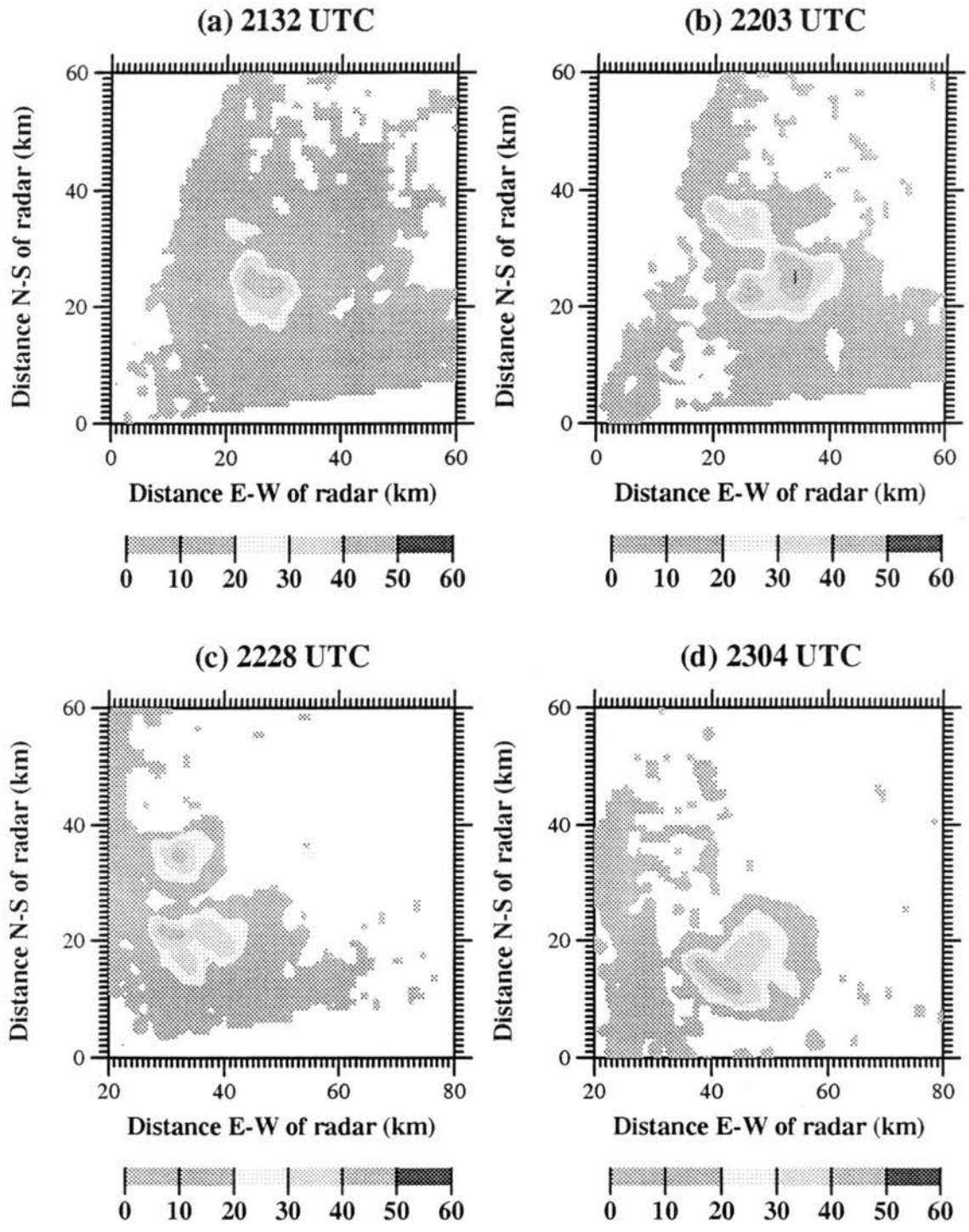

Figure 3.21 (a-d) Horizontal radar reflectivity cross sections at height of 1.5 km from the CSU-CHILL radar for: a) 2132 UTC; August 9, 1996; b) 2203 UTC; August 9, 1996; c) 2228 UTC; August 9, 1996; d) 2304 UTC; August 9, 1996. Notice changes in scale.

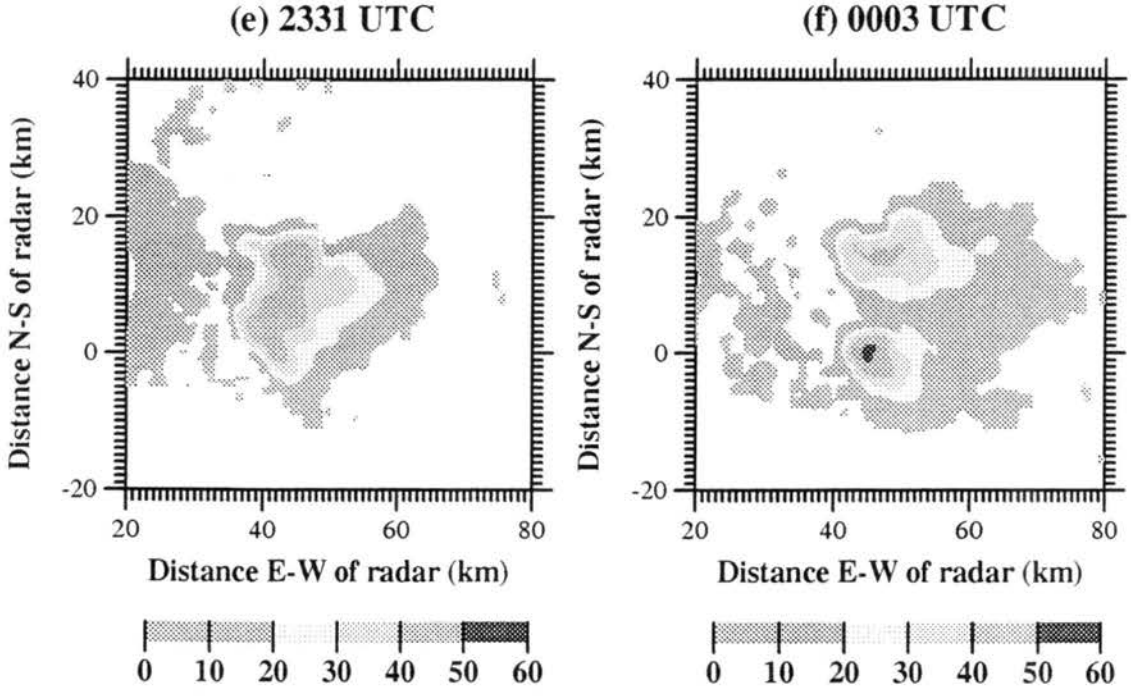

Figure 3.21 (e-f) Horizontal radar reflectivity cross sections at height of 1.5 km from the CSU-CHILL radar for: e) 2331UTC; August 9, 1996; f) 0003 UTC; August 10, 1996. Notice changes in scale.

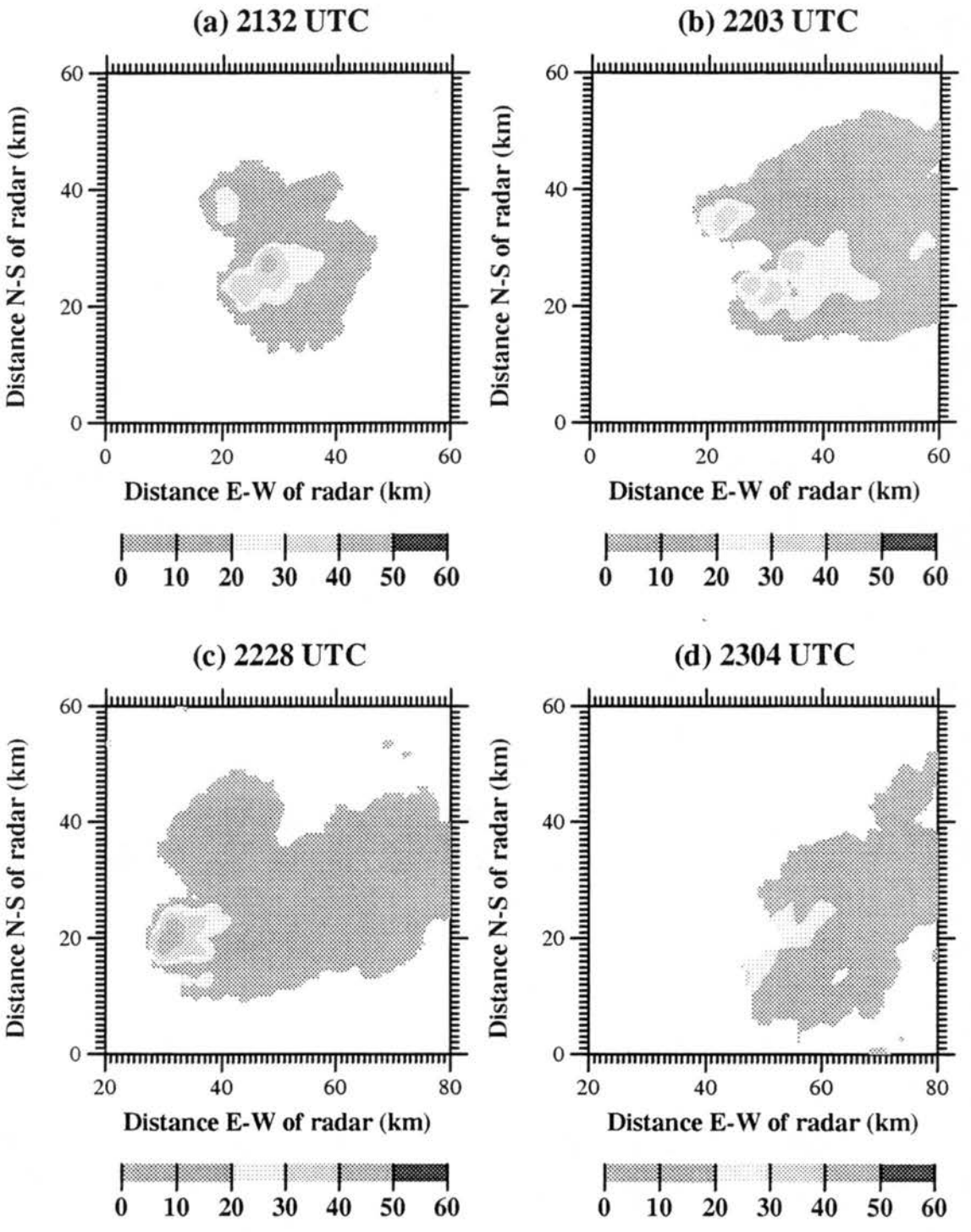

Figure 3.22 (a-d) Horizontal radar reflectivity cross sections at height of 7 km from the CSU-CHILL radar for: a) 2132 UTC; August 9, 1996; b) 2203 UTC; August 9, 1996; c) 2228 UTC; August 9, 1996; d) 2304 UTC; August 9, 1996. Notice changes in scale.

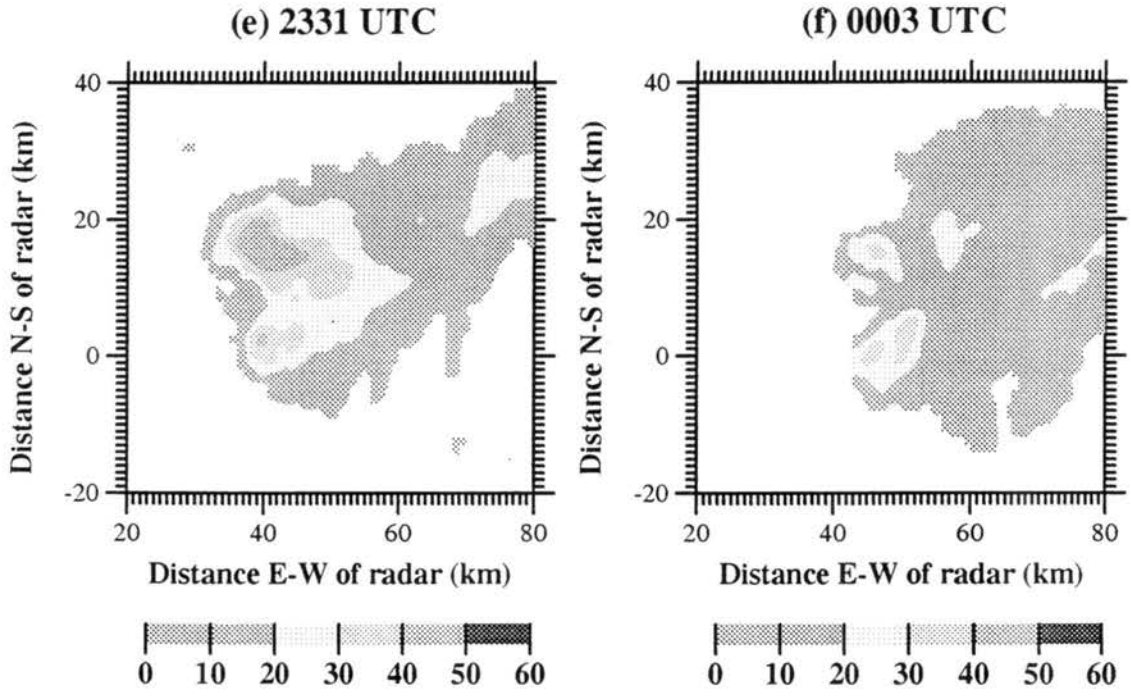

Figure 3.22 (e-f) Horizontal radar reflectivity cross sections at height of 7 km from the CSU-CHILL radar for: e) 2331UTC; August 9, 1996; f) 0003 UTC; August 10, 1996. Notice changes in scale.

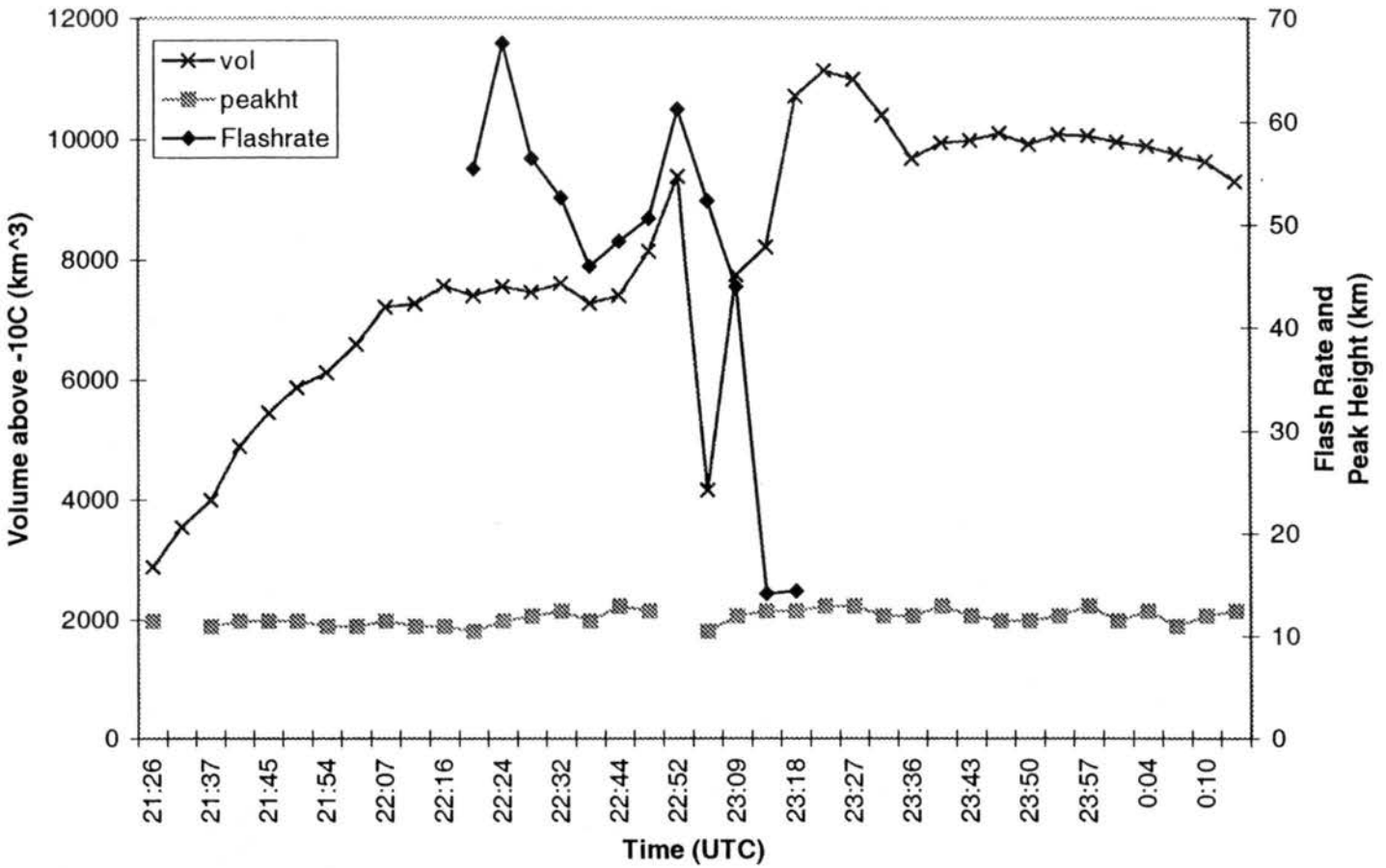

Figure 3.23(a) Time series of radar and lightning variables: 2126 August 9, 1996 through 0013 UTC August 10, 1996. Radar variables calculated using 0 dBZ and -10°C thresholds. Flash rates (min^{-1}) is a five minute average.

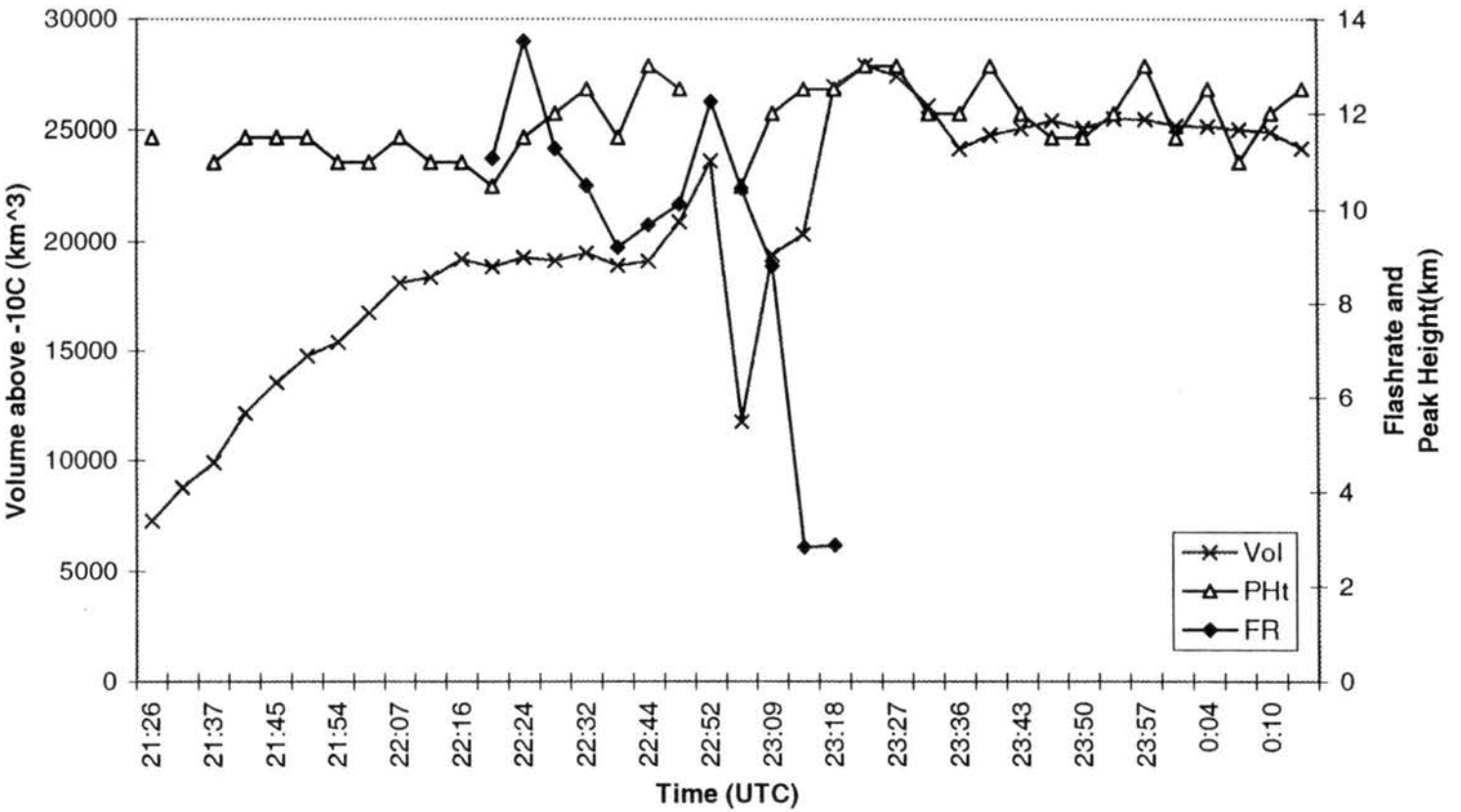

Figure 3.23(b) Time series of radar and lightning variables: 2126 August 9, 1996 through 0013 UTC August 10, 1996. Radar variables calculated using 30 dBZ and -10°C thresholds. Flash rate (min^{-1}) is a five minute average.

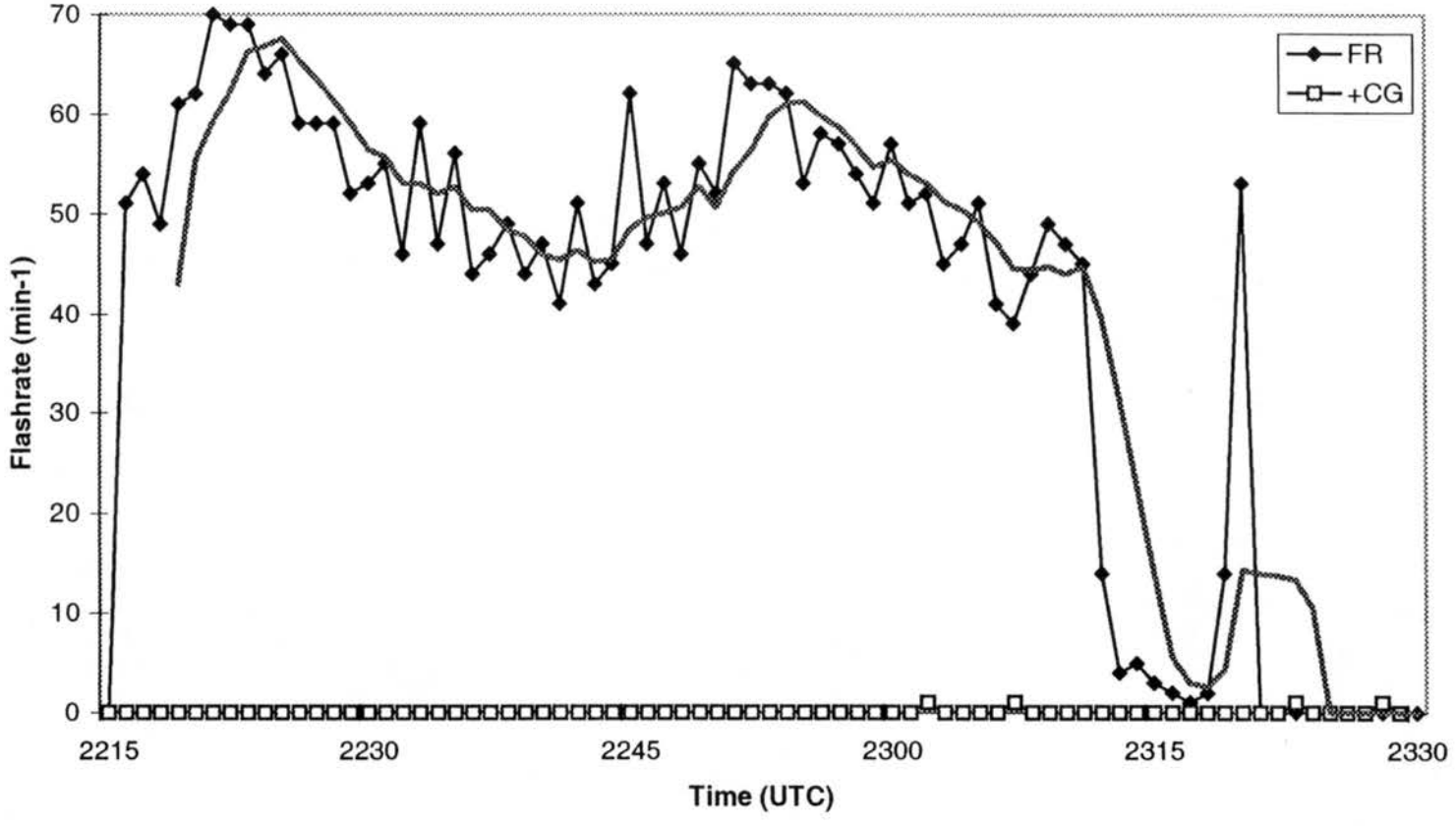

Figure 3.24 Time series of lightning flashrates from 9 August 1996, 2215 to 2330 UTC. FR indicates total flash rate (min^{-1}). Five minute moving average of FR shown in thick gray line. CG indicates cloud-to-ground flash rate (min^{-1}).

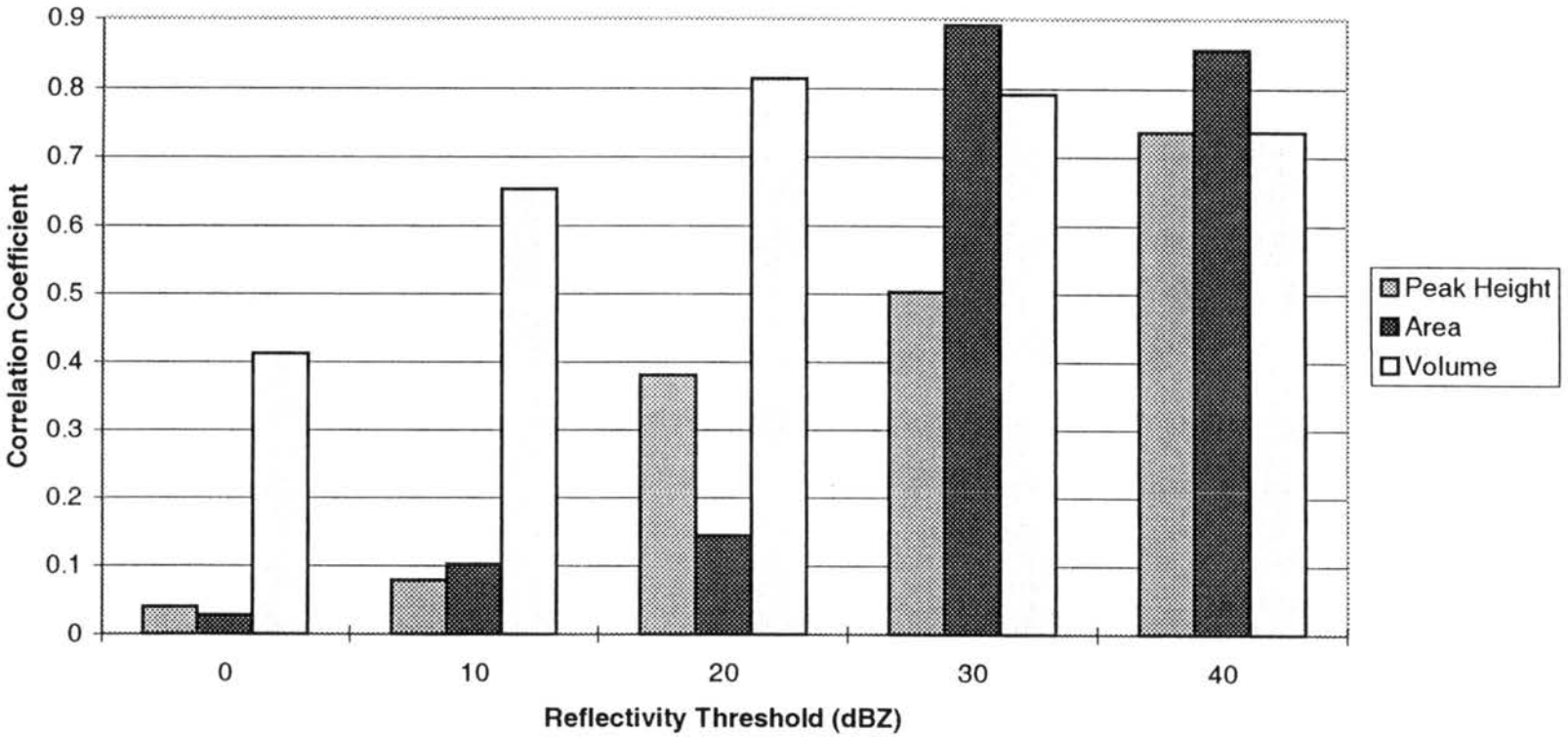

Figure 3.25 Linear regression correlation coefficients of peak radar parameters (height, area and volume) vs. peak total flash rate for all northeast Colorado cases (except A9). Bars represent radar parameters coefficients grouped by reflectivity threshold.

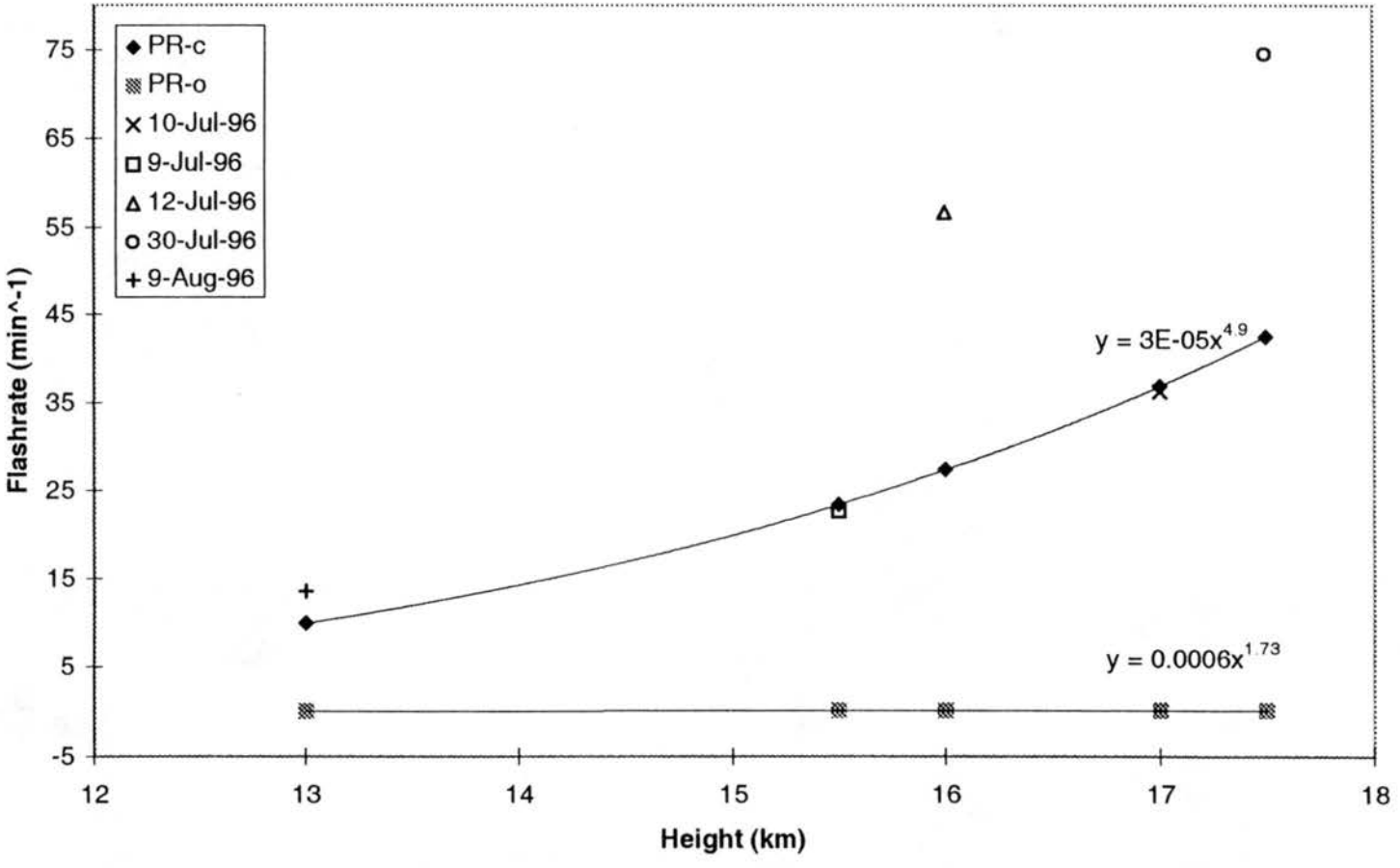

Figure 3.26 Total flashrate on the ordinate and cloud top height (as determined by the peak radar height for the case at 0 dBZ) on the abscissa. PR92 continental (PR-c) and maritime (PR-o) parameterizations are solid curves with solid diamonds or squares. Northeast Colorado cases are plotted as described in legend.

CHAPTER 4

TROPICAL CASES FROM NORTHERN AUSTRALIA

In this chapter we analyze three storms from tropical Northern Australia during the southern hemisphere summer wet seasons of 1995 and 1998. We investigate the relationships between the radar parameters and lightning observations in a similar fashion as in Chapter 3. We also address the issue of effective detection range of the FCM by performing sensitivity tests varying the range thresholding of the radar data.

4.1 November 23, 1995

On November 23, 1995 (N23), convection was under way over the Tiwi islands by 0527 UTC. Figure 4.1 illustrates the sounding from 0304 UTC. The CAPE was calculated as 1508 J kg^{-1} by considering the first 500 m as the mixed layer and the Lifted Index was -2°C (D. Ahijevych, personal communication 1998). The Bulk Richardson Number (R), a ratio of the atmospheric instability versus the low level shear magnitude, is given by:

$$R = \frac{CAPE}{\frac{1}{2}\mathbf{u}^2} \qquad (4.1)$$

where **u** is the difference in the mean wind vectors between the 6 km and 0.5 km levels. To accurately represent the tropical environment, especially the low level shear associated with the trade wind flow regime, Keenan (1990) used the mean horizontal wind at 3 km instead of at 6 km. In this manner, R (0.5 to 3.0 km) was calculated as 494, much lower than the standard calculation of 898. Weisman and Klemp (1986) have shown the high R is generally associated with ordinary cellular convection. In addition, high R

does not tend to lead to long-lived convection since the high CAPE also leads to strong downdrafts that can outrun the mean relative inflow, isolating the convection from the undisturbed air. The N23 case developed much as these parameters suggested.

Figure 4.2 (a-d) shows low level (1.5 km) horizontal cross sections of reflectivity approximately every half hour from 0527 to 0659 UTC. Figure 4.3 (a-d) shows upper level (9 km) horizontal cross sections of reflectivity from corresponding volume scans. The formation of several low reflectivity cores to the north and northeast of the radar had occurred by 0527 UTC. Some of the cells from 0527 to 0659 UTC were barely within the FCM's 40 km range (the FCM is located at the radar site). The upper level cross sections show the formation of an anvil between 0527 and 0601 UTC. The southeast flow aloft continued to advect hydrometeors downstream, creating a persistent anvil through the end of the data period. The cells from the storm remained at distances close to the edge of the FCM effective range.

One difficult issue to address with the small range of the FCM is the storm area which influences the flash rate detected by the FCM. The detection of stronger flashes at further distances complicates the quantification of the effective detection range. In Chapter 2, the range was established as approximately 40 km. The filtering of the radar data to the reflectivity associated with the flashes will be addressed by filtering the data to different ranges and determining if trends between the resulting radar parameters and flash-rates are observed. In addition, as in Chapter 3, different temperature parameters (the base of the area and volume radar variables) will be used to determine which is best suited for matching the flash-rate data.

Three types of radar variables were considered: peak height, area bounded by a reflectivity threshold above the height of a temperature threshold, and volume bounded by a reflectivity threshold above the height of a temperature threshold. These variables were calculated for each reflectivity threshold, temperature threshold and range filter from the radar site. Then, linear regressions between the time series pairs of these variables and the total flash rate were performed. Figure 4.4 shows one of the best examples of correlation for these linear regressions for the 20 dBZ reflectivity threshold, the -10°C parameter and a filter from the radar site of 50 km. The correlation coefficients from these linear regressions for the different temperature parameters at a range of 40 km are shown in Figure 4.5. The peak height is not calculated using this temperature parameter, and varies only with reflectivity in this figure. Peak height has

its highest correlation, a weak correlation of $R^2 = 0.32$, at the 10 dBZ threshold. The area parameter has its highest correlation of $R^2 = 0.59$ with the -10°C parameter at the 20 dBZ threshold, while volume peaks at $R^2 = 0.55$ with the -10°C parameter at the 10 dBZ threshold. Volume tends to correlate best at either -10°C or -20°C for the lower reflectivity thresholds, and at 0°C for the higher reflectivity thresholds. This correlation could be a simple function of the lack of volume above the colder temperature parameters for the higher reflectivity thresholds. Conversely, significantly greater volumes exist above the temperature cutoffs for the smaller reflectivity thresholds (see Table 4.1), and the colder temperature parameter becomes a better measure for these thresholds.

The variation of the radar variables with range from the radar site and the corresponding correlation coefficients are shown for reflectivities of 0 and 10 dBZ in Figures 4.6 and for 20 and 30 dBZ reflectivities in Figure 4.7. The temperature parameter used here was -10°C. The correlation tends to increase with increasing range threshold on the radar data, sometimes reaching a maxima for a certain range and falling for larger ranges. In general, the radar parameters have the best correlation for ranges of 45 or 50 km. The best correlation for the case, a strong correlation of $R^2 = 0.89$ for the area variable and $R^2 = 0.82$ for the volume variable, occurred for the range of 50 km at the 20 dBZ threshold. A time series plot of this series of parameters is shown in Figure 4.8. In this figure, we can see the peak in the radar variable one radar volume (approximately 6 minutes) before the peak in total flash rate and the trend in these variables is obvious.

The lightning flash rates from the storm are shown in Figure 4.9. The flash rates in this figure are per minute and the total flash rate reaches a maximum of 61 flashes during both 0552 and 0553 UTC. The cloud-to-ground flash rate reaches a maximum of 20 flashes at 0528 UTC (the total flash rate at this time is 22 flashes per minute). The in-cloud to total flash rate ratio reaches its lowest value at this time, 0.1, whereas this ratio typically remains around 0.8 to 0.9 during the most active portion of the storm (0520 through 0630 UTC). The total production of the storm, from the FCM and ALDF data, was 2821 IC flashes and 238 CG flashes, for a total of 3044 flashes. Thus, 92.7% of the flashes were IC flashes. Of the CG flashes, 223 lowered negative charge to ground and 15, or 6.3%, lowered positive charge to ground. A brief

discussion in Section 4.4 and further discussion in Chapter 5 addresses the relationship between the total lightning production and the radar parameters for the Australia cases.

4.2 November 27, 1995

By 0334 UTC on November 27, 1995 (N27), convection was occurring over the Tiwi Islands. Figure 4.10 illustrates the sounding from 0258 UTC. The sounding exhibited a CAPE of 703 J kg^{-1}; a R (0.5 to 3 km shear layer) of 112 and an LI of -2°C. This sounding, like the N23 case, also points to the formation of short-lived, non-severe cellular convection. Though the sounding indicates similar convective structures as the N23 sounding, the lower CAPE suggests that weaker updrafts and less intense electrification would occur in this case.

Figure 4.11 (a-l) shows low level (1.5 km) horizontal cross sections of reflectivity approximately every half hour. Figure 4.12 (a-l) shows the corresponding upper level cross sections (9 km). Initially, the storm formed in an east-west line immediately north of the radar. As opposed to the N23 case, many of the cells were forming much closer to the radar site. The convection began to diminish around 0601 UTC and had almost dissipated by 0830 UTC. The westerly upper level winds are weaker than the N23 case and do not succeed in creating such an extensive anvil. This could also be a function of the reduced intensity of the N27 case, as indicated by radar cross sections and the CAPE, resulting in a lower production of convective debris to be lofted.

Once again, the radar variables were calculated over different ranges, temperature parameters and reflectivity thresholds. The resulting linear regressions for different temperature parameters using a range of 40 km are presented in Figure 4.13. The results of reflectivity threshold variation in this figure show much lower correlations at 20 and 30 dBZ thresholds. The correlations show a weak trend toward being higher for the -10°C and -20°C parameters. The correlation coefficients for the range variations are shown for the 0 and 10 dBZ thresholds in Figure 4.14 and for the 20 and 30 dBZ threshold in Figure 4.15. Just as in the temperature tests, the highest correlations is for volume at 10 dBZ. The correlations increase with the larger ranges, peaking at $R^2 = 0.41$ (weak correlation) for the area variable and $R^2 = 0.43$ for the volume

variable. A time series of the radar variables and the five minute averaged total flash rate for the 10 dBZ reflectivity, -10°C temperature parameter, and 50 km range is shown in Figure 4.16. This figure illustrates the many brief peaks in total flash rate over the storm's lifetime. The last peak in total flash rate is unaccompanied by a dramatic rise in radar variables, as one might expect.

The lightning flash-rates for N27 are shown in Figure 4.17. The 1-minute total flash rate peaks at a rate of 50 min^{-1} at 0622 UTC, but has secondary peaks of 33 min^{-1} at 0433 UTC, 26 min^{-1}at 0523 UTC, and 24 min^{-1} at 0556 UTC. The CG 1-minute flash rate peaks at 7 min^{-1} at 0442 UTC, with several other minor periods of CG production either during or directly after periods of intense IC production. The FCM and ALDF data indicate the storm's total production was 2410 total flashes, 100 of these being CG for an in-cloud to total-flash-rate ratio of 0.96. In addition, only one of the 100 CG strikes lowered positive charge to ground.

4.3 January 9, 1998

Figure 4.18 (a-h) shows low level (2 km) horizontal cross sections of reflectivity from 0700 to 1030 UTC. Figure 4.19 (a-h) shows the corresponding upper level (7 km) horizontal cross sections of reflectivity. A collection of cells about 40 km to the west of the radar, initially at 0700 UTC, formed into a line of cells and propagated through the research area. Upper level cross sections, at 7 km, show little convective debris after the cells propagated through the area. The precipitation during the JA29 case formed predominately by warm-cloud processes, since the cells rarely exceeded 30 dBZ at the 7 km level, which corresponds to -10°C. Moderate westerly mid-level winds caused the rain-bands which formed to quickly move through the research area. No sounding data were available for this event.

With the visual observations of no flashes during the time period between 0800 and 1000 UTC, all the radar variables attained by this storm are correlated with the lack of lightning and will be used as such for comparison to other cases. See Table 4.1 in Section 4.4 for maximum radar variables attained in this case for each reflectivity threshold for the 40 km range and -10°C temperature threshold. The 40 km range was used to ensure the radar variables excluded portions of other storms which may have had lightning.

4.4 Comparison of Cases from Northern Australia

Now that we have examined the correlations of total flash rate with radar variables (peak height, area and volume) for all of the cases, we will draw comparisons between these cases. We found that for the N23 and N27 cases, the highest correlations between radar variables and total flash rate were found using larger radar ranges (45 or 50 km) than the estimated effective range of the FCM (40 km). Another factor which led to higher correlations was a reflectivity threshold of 10 or 20 dBZ, this held true for volume for the N27 case but not peak height or area. Like in the mid-latitude cases, the peak heights, especially those at 0 dBZ (i.e. cloud top height), had much weaker correlation than the area and volume parameters. As in Chapter 3, later in this section we will also examine the relationship between the total flash rate and the product of the volume and area radar variables (this parameter is aimed at being a more accurately scaled version of H^5). We will also look at where our maximum flash rate and cloud top height, as determined by 0 dBZ, compares to the Price and Rind (1992) parameterization. However before doing this, we first examine the maximum observed values of the radar and lightning variables.

Table 4.1 lists the maxima of the radar variables for the three cases using the temperature parameter of -10°C, varying the reflectivity threshold and using a 50 km range for the MCTEX cases and a 40 km range for the visual based JA29 case. From the upper level cross sections of JA29, Figure 4.20, as well as from the values for JA29 in Table 4.1, the JA29 case is much less vertically developed than the two MCTEX cases. The parameter maxima for the two MCTEX cases are very similar. The N23 case has higher areas and volumes at the higher 20, 30 and 40 dBZ thresholds, while the N27 case generally has higher values at the 0 and 10 dBZ thresholds. This reversal is interesting since the N23 case was generally at the edge of the FCM effective range, and it had greater flash rates for both IC and CG lightning. Table 4.2 details the total lightning production of the different storms. The N23 case was a lightning producer (as far as the FCM measurements went) from 0500 to 0730 UTC while the N27 case produced significant lightning from 0345 to 0645 UTC. The greater production by the N23 case of both total and CG flashes corresponds to greater radar variable magnitudes (see Table 4.1) at higher reflectivity thresholds. The lower value radar variables (see Table 4.1) for the N23 case, as compared to the N27 case, at the lower

reflectivity thresholds may have been due to the large distance of the cells from the FCM/radar site. These trends seen in the correlations between the radar variables and the total flash-rates are discussed in relation to both the mid-latitude and tropical cases in Chapter 5, Section 1.

Table 4.1 Maximum Radar Variable values Attained for Variations in Radar Threshold at Range of 50 km and Temperature Parameter of -10°C

Nov. 23 dBZ	**Peak Height (km)**	**Area (km^2)**	**Volume (km^3)**
0	19.5	2200	20000
10	19	1500	11000
20	18.5	790	4900
30	17	340	1600
40	12.5	130	210
Nov. 27			
0	18	3400	21000
10	18	2600	12400
20	17.5	740	3000
30	17	290	950
40	12	83	210
Jan. 29			
0	15	2400	9600
10	14	1100	2800
20	11.5	260	280
30	8.5	98	72
40	7	23	19

Table 4.2 Total Lightning Parameters for Australian Cases

Case	**Total Flashes**	**Hours**	**Total Production (flashes hr^{-1})**	**Cloud-to-Ground (flashes)**	**CG Production (flashes hr^{-1})**
N23	3044	2.5	1218	238	95.2
N27	2410	3	803	100	33.3
JA29	0	2	0	0	0

The product of the volume and area is listed in Table 4.3. The first product is the product of the maxima of volume and area, the second is the average of the product during each time series. The average product follows a different trend than the maxima product, as seen in Table 4.4. Also, this trend varies from case to case. This relationship is also compared to the lightning parameters for the complete set of cases in Chapter 5.

Table 4.3 Product of Volume and Area for Australian Cases

N23 dBZ	Maxima Product (km^5)	Avg. Product (km^5)	N27 dBZ	Maxima Product (km^5)	Avg. Product (km^5)	J29 dBZ	Maxima Product (km^5)	Avg. Product (km^5)
0	4.5×10^7	2.6×10^7	0	7.1×10^7	2.9×10^7	0	2.3×10^7	9.7×10^6
10	1.6×10^7	8.6×10^6	10	3.2×10^7	9.8×10^6	10	3.2×10^6	6.7×10^5
20	3.8×10^6	1.2×10^6	20	2.2×10^6	6.4×10^5	20	7.3×10^4	3.1×10^4
30	5.4×10^5	1.9×10^5	30	2.7×10^5	4.8×10^4	30	7.1×10^3	3.3×10^3
40	2.8×10^4	7.8×10^3	40	1.8×10^4	2.8×10^3	40	4.4×10^2	7.7×10^1

Table 4.4 Ratio of Maxima Product to Average Product for Australian Cases

dBZ	Nov. 23 MP/AP	Nov. 27 MP/AP	Jan. 29 MP/AP
0	1.69	2.45	2.40
10	1.86	3.25	4.78
20	3.07	3.48	2.39
30	2.81	5.68	2.15
40	3.59	6.34	5.68

Finally, in Figure 4.20 we examine the three Australian cases compared to the PR92 parameterization. We see that the JA29 null case falls on the maritime parameterization. The N23 case falls nearly on the continental parameterization, and the N27 case falls between the parameterizations. These results provide a perfect example of the shortcomings when using the PR92 parameterization in a region having both continental and maritime influences on convection.

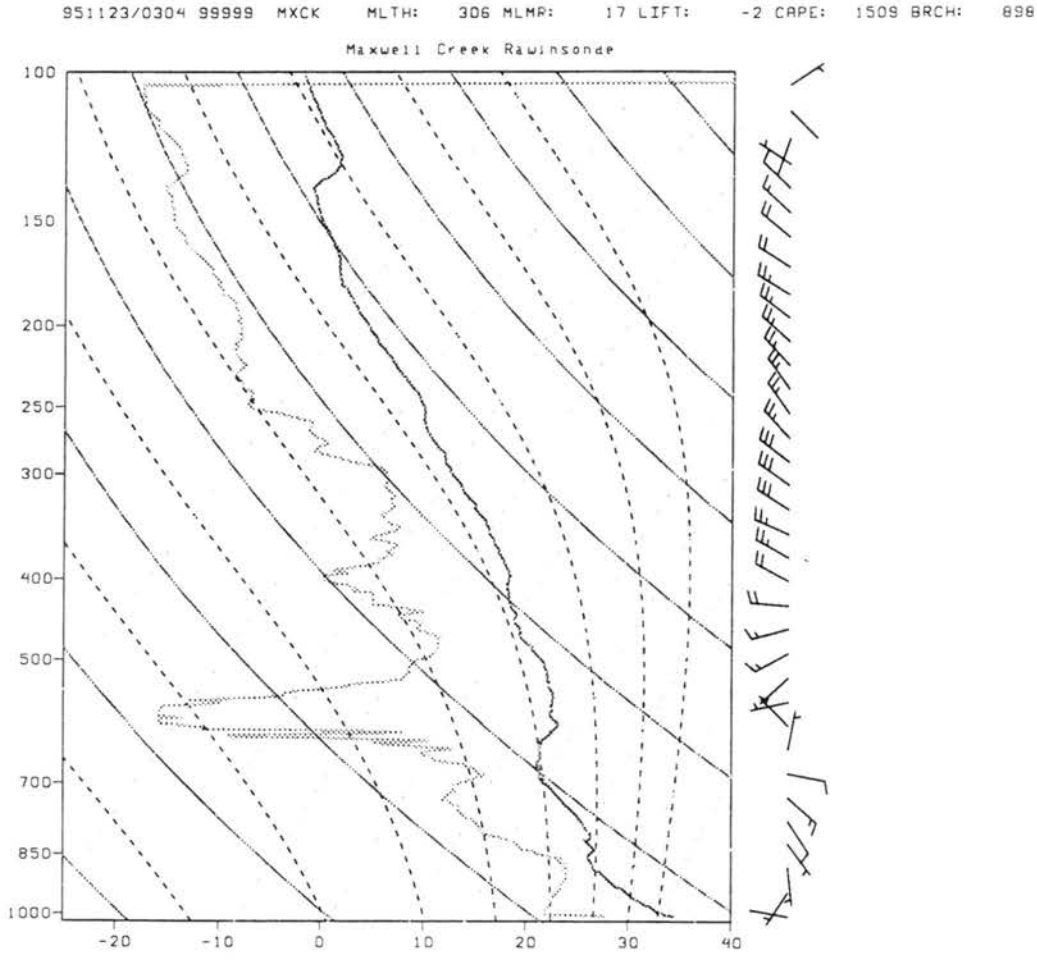

Figure 4.1 MCTEX Sounding 23 November 1995 at 0304 UTC.

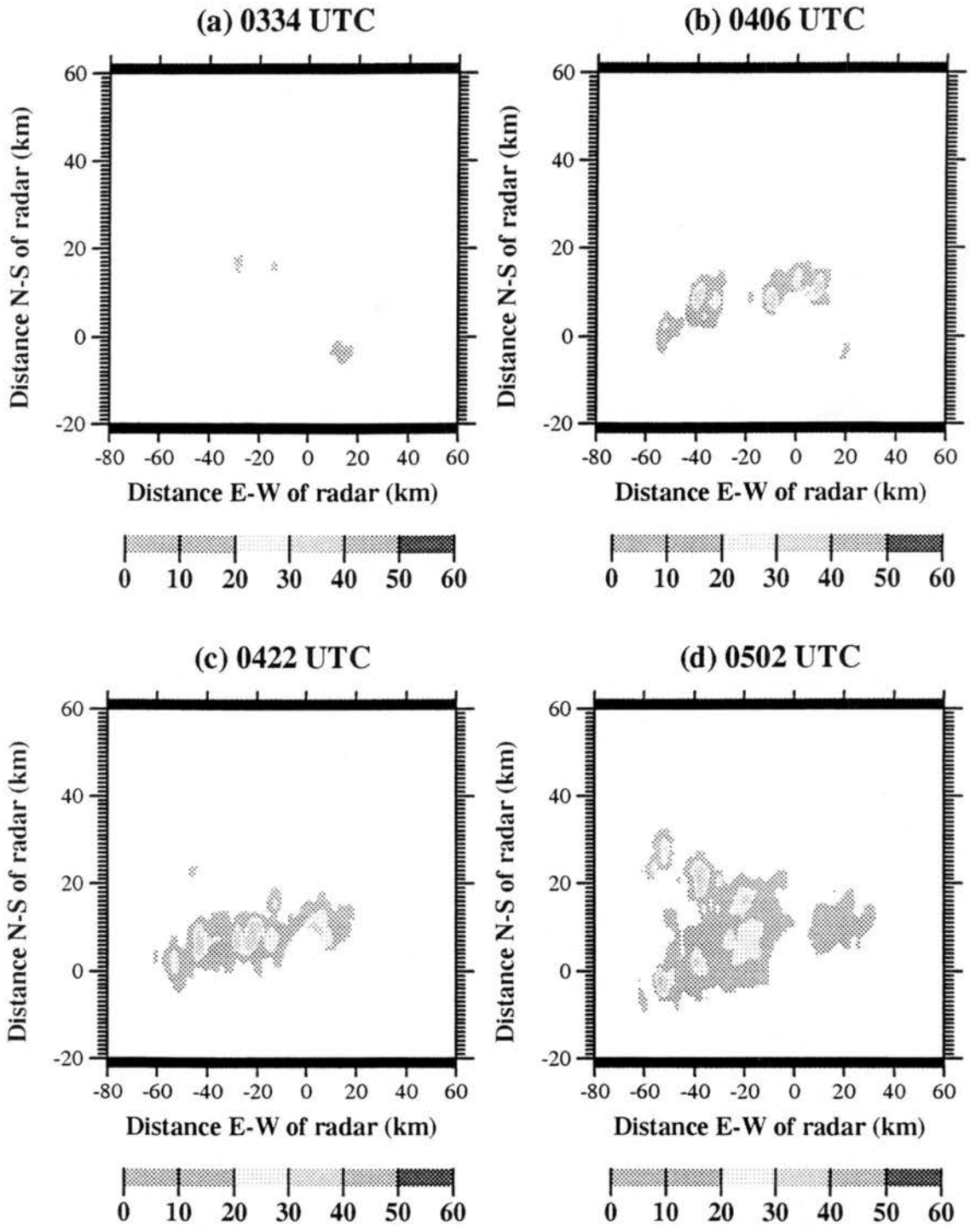

Figure 4.2 (a-d) Horizontal radar reflectivity cross sections at height of 1.5 km from the CPOL radar for: a) 0527 UTC; 23 November 1995; b) 0601 UTC; 23 November 1995; c) 2331 UTC; 23 November 1995; d) 0003 UTC; 23 November 1995.

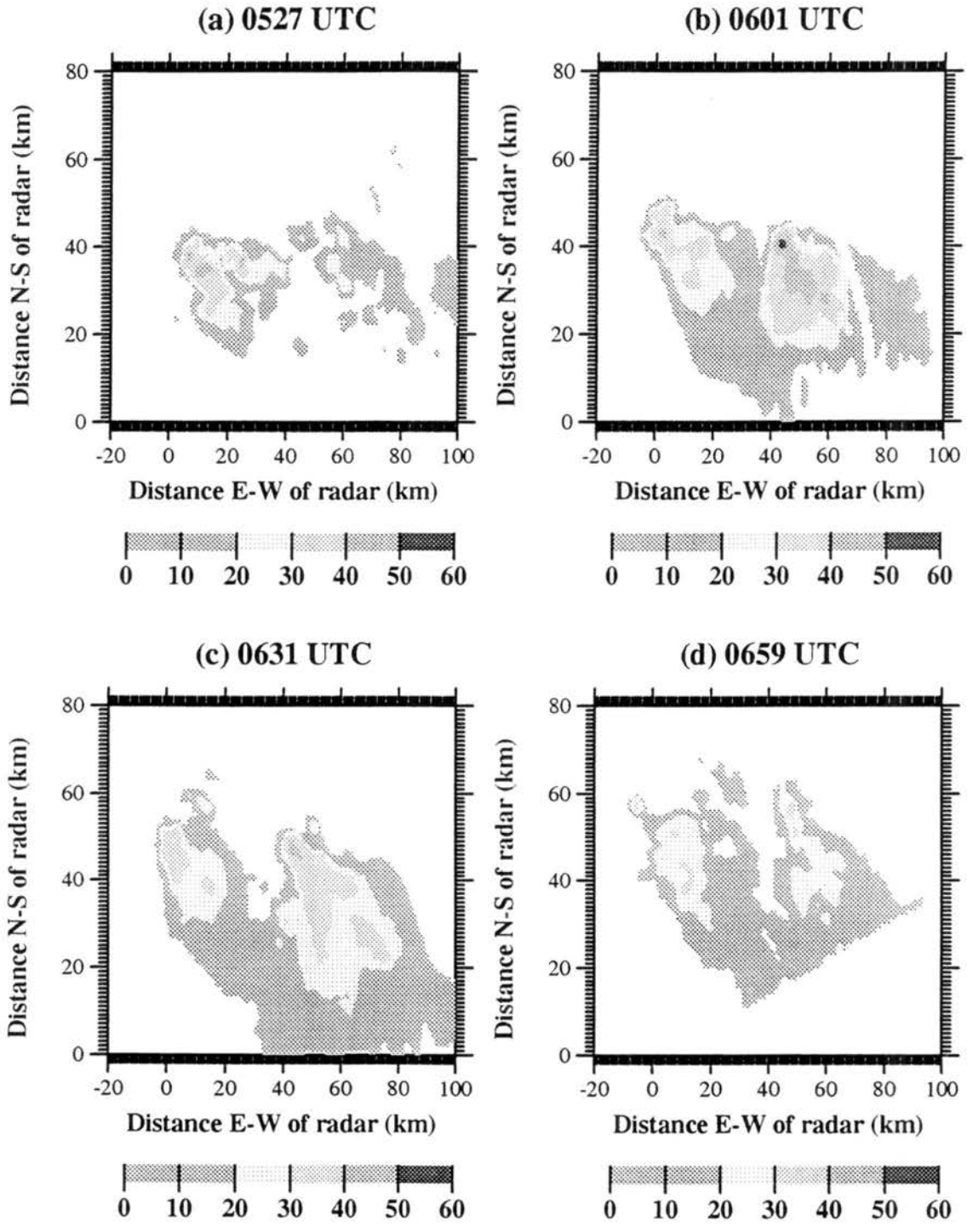

Figure 4.3 (a-d) Horizontal radar reflectivity cross sections at height of 9 km from the CPOL radar for: a) 0527 UTC; 23 November 1995; b) 0601 UTC; 23 November 1995; c) 2331 UTC; 23 November 1995; d) 0003 UTC; 23 November 1995.

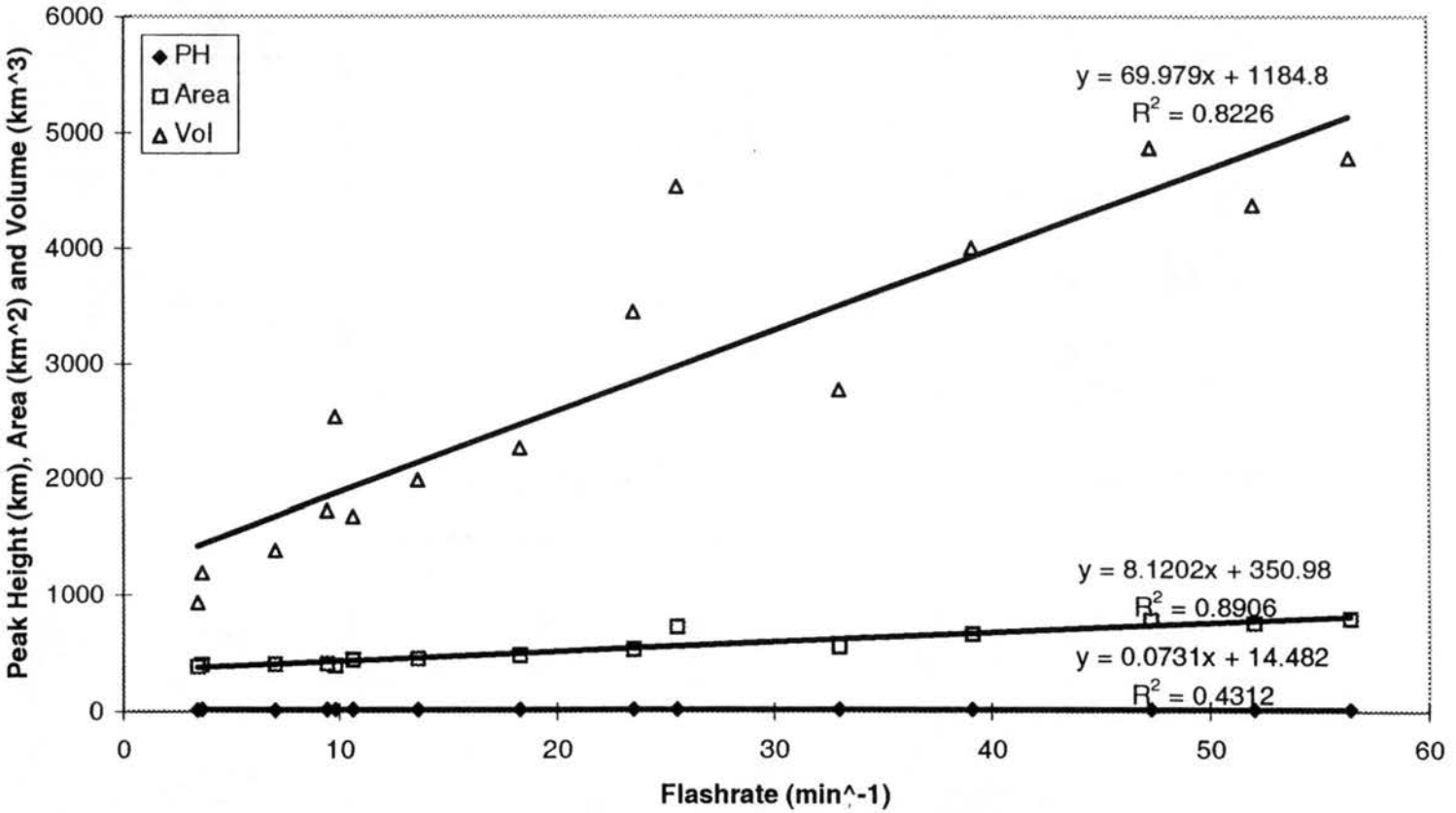

Figure 4.4 Scatter plot and linear regression between flash rate and radar variables calculated using 20 dBZ and -10°C thresholds, using 50 km range for filtering radar data, for 23 November 1995 case. Radar variables are peak height, area and volume. Equations and correlation coefficient are shown.

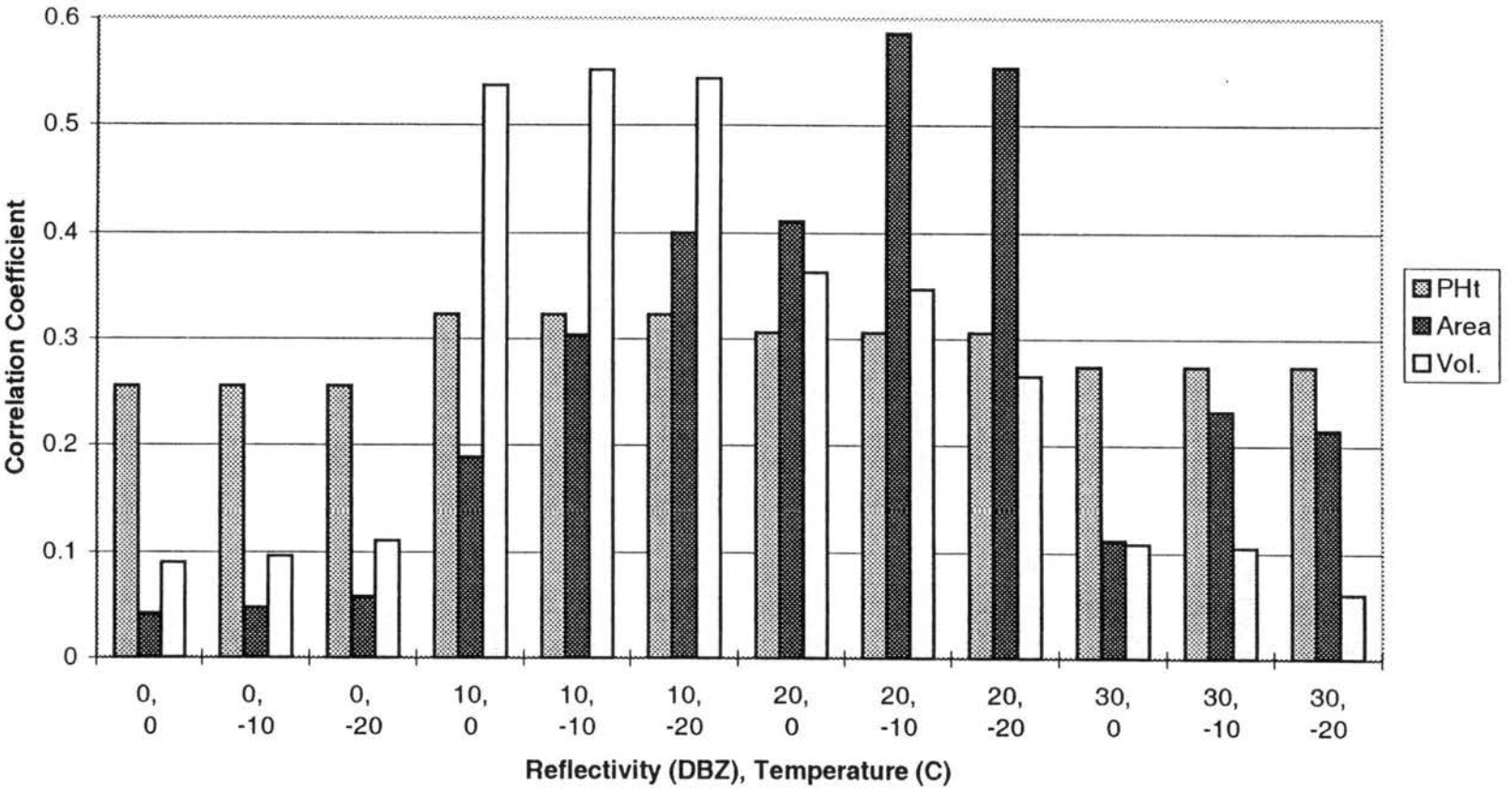

Figure 4.5 Correlation coefficients from linear regressions while varying temperature threshold for 23 November 1995 case.

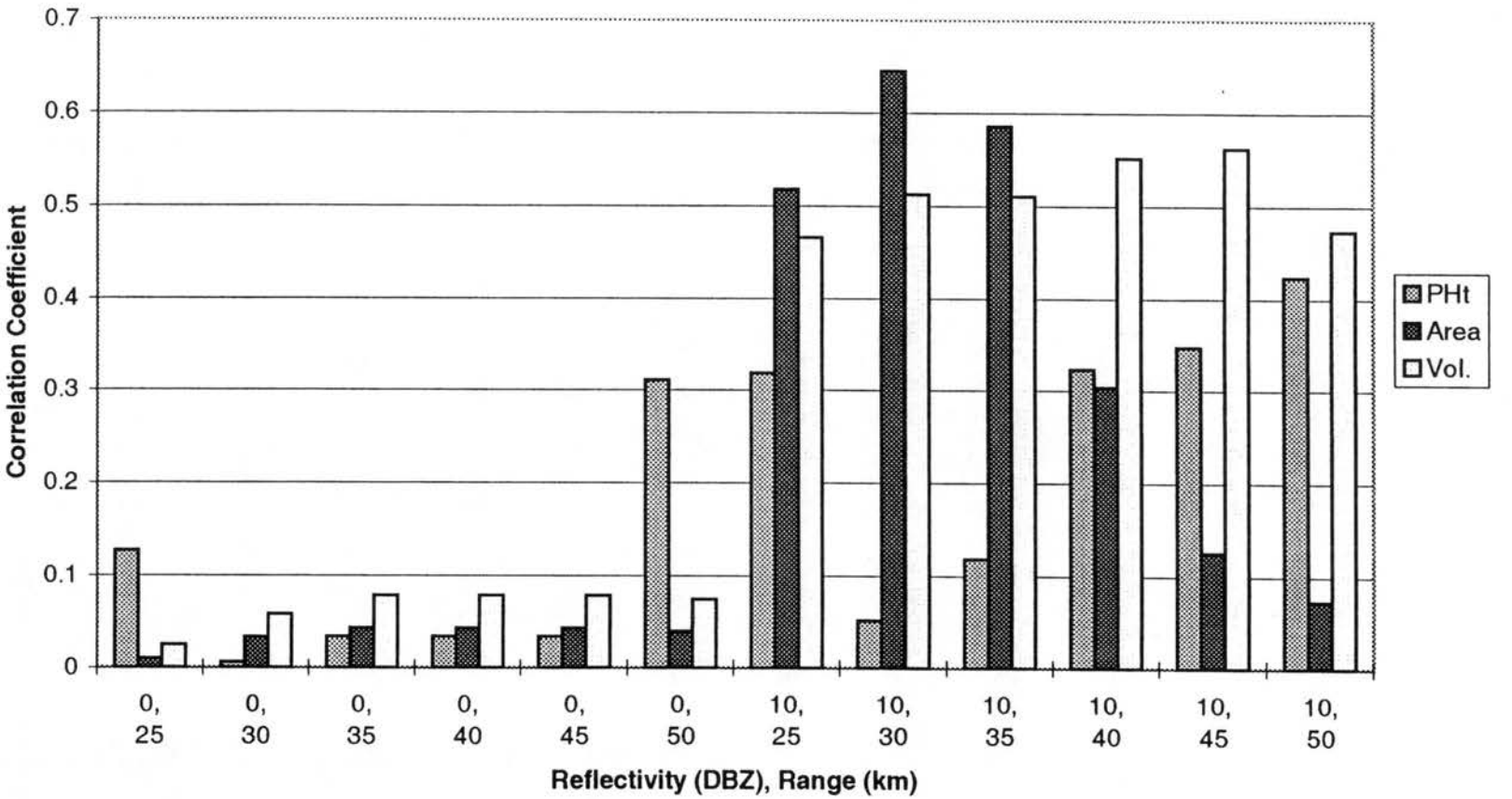

Figure 4.6 Correlation coefficients from linear regressions while varying range radar data were filtered. Shown are results for 0 and 10 dBZ for 23 November 1995 case.

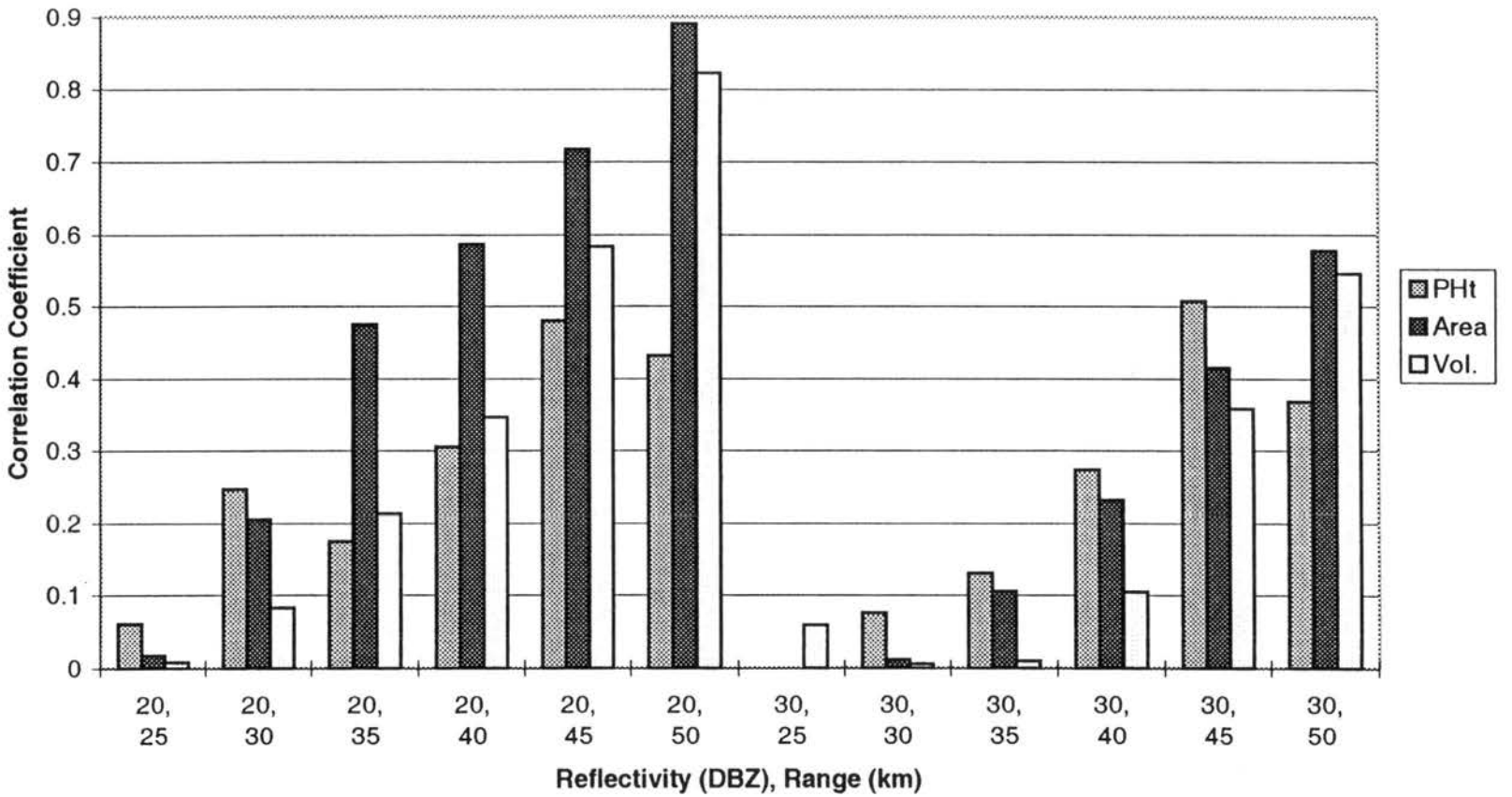

Figure 4.7 Correlation coefficients from linear regressions while varying range radar data were filtered. Shown are results for 20 and 30 dBZ for 23 November 1995 case.

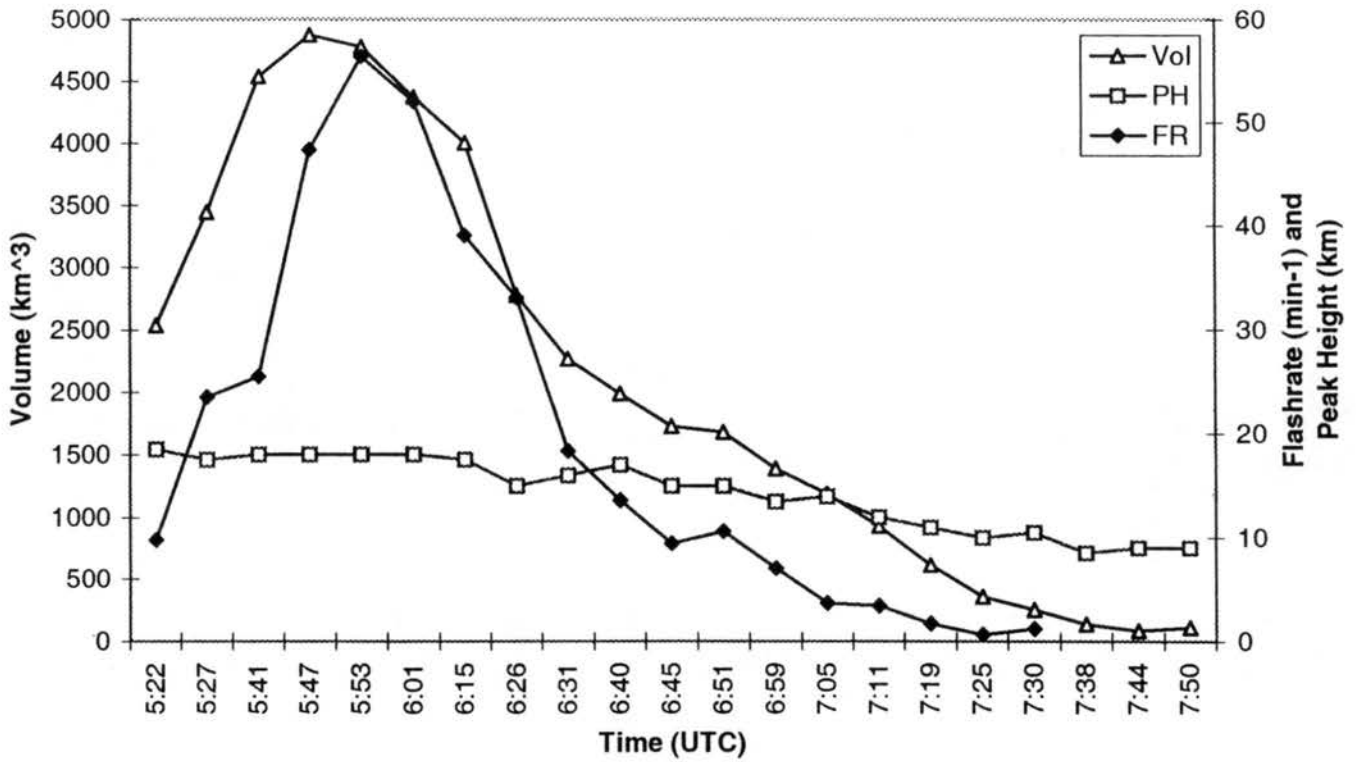

Figure 4.8 Time series of radar and lightning variables: 0522 through 0750 UTC 23 November 1995. Radar variables calculated using 50 km range filter and 20 dBZ and -10°C thresholds. Flash rates (min^{-1}) are five minute averages.

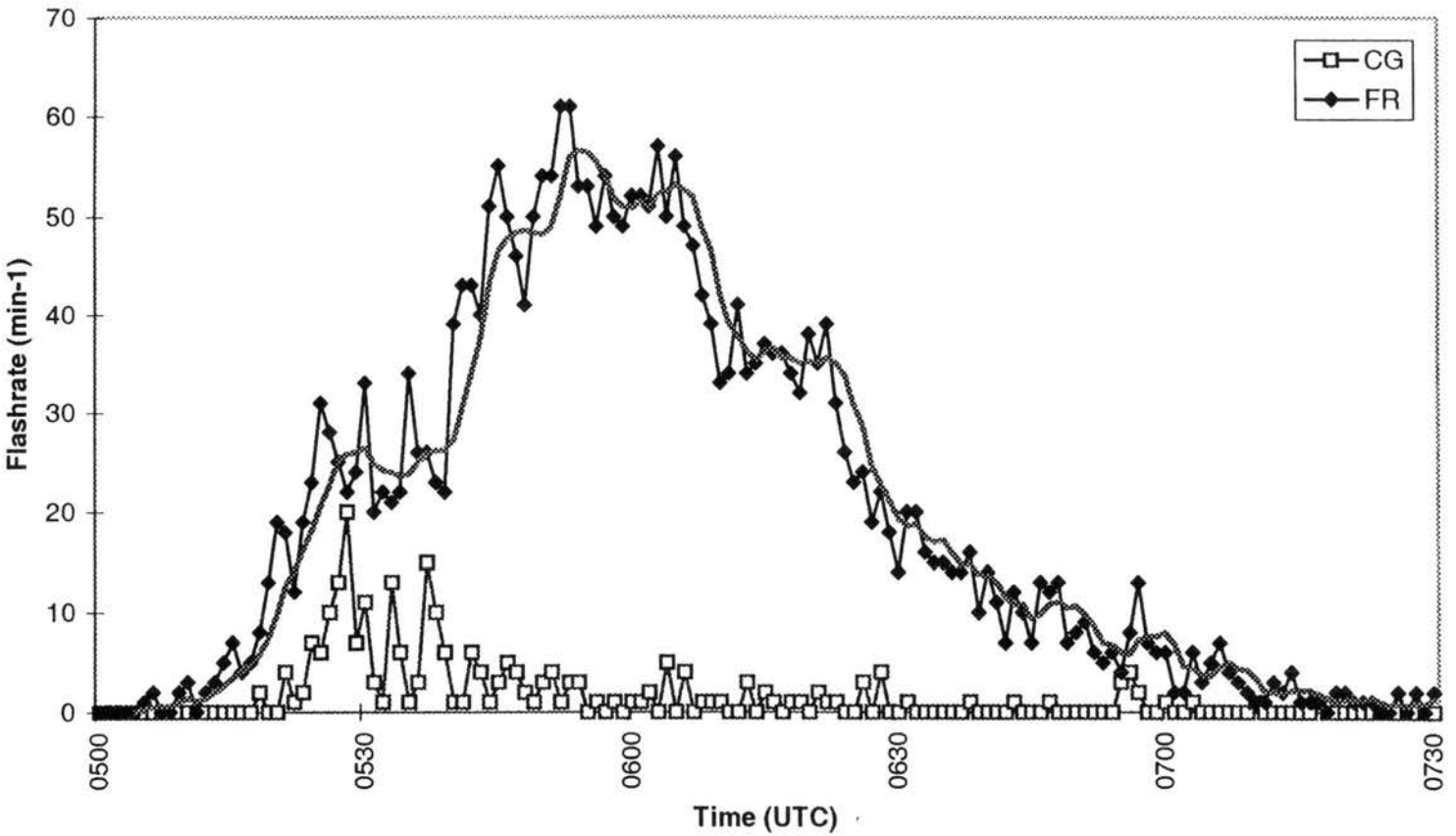

Figure 4.9 Time series of lightning flash rates from 23 November 1995 case. FR indicates total flash rate (min^{-1}). Five minute moving average of FR shown in thick gray line. CG indicates cloud-to-ground flash rate (min^{-1}).

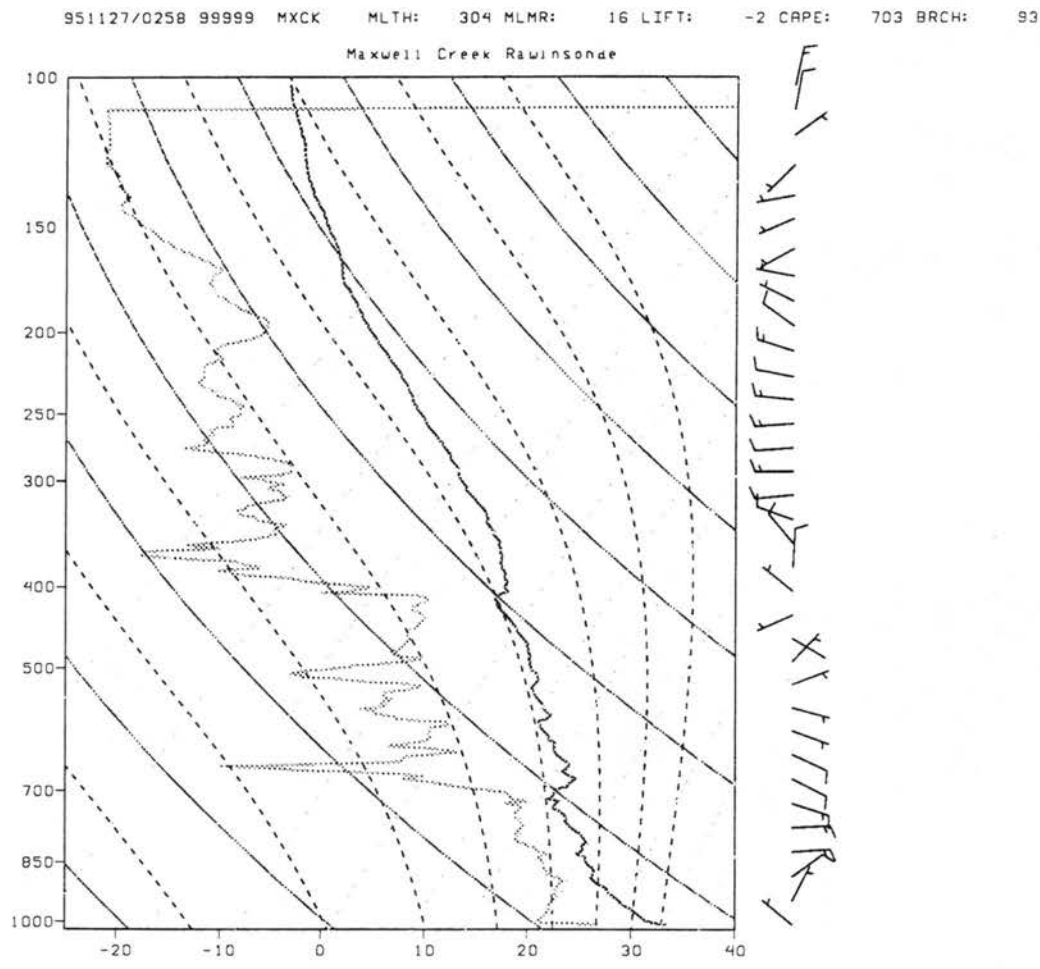

Figure 4.10 MCTEX sounding from 0258 UTC 27 November 1995.

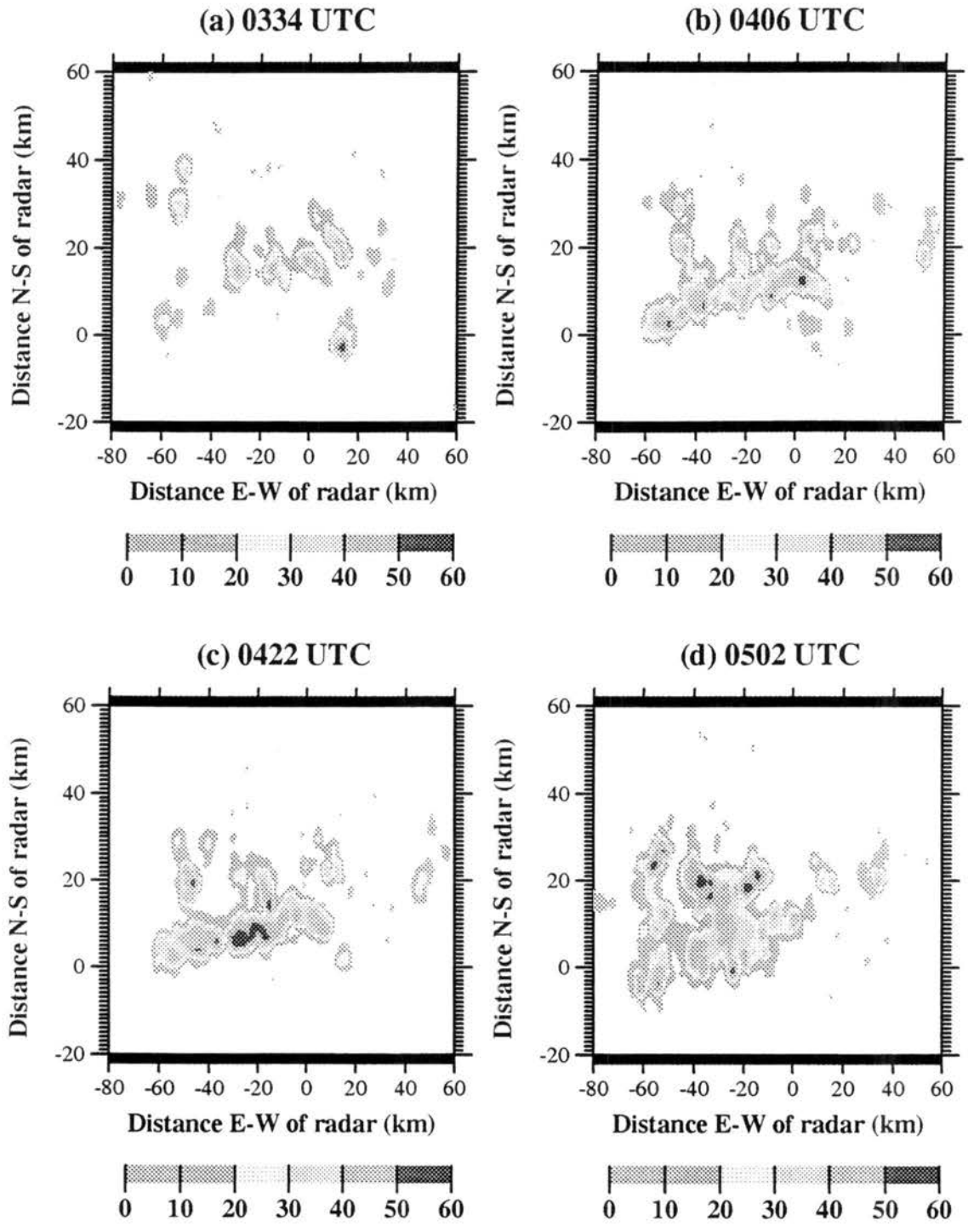

Figure 4.11 (a-d) Horizontal radar reflectivity cross sections at height of 1.5 km from the CPOL radar for: a) 0334 UTC; 27 November 1995; b) 0406 UTC; 27 November 1995; c) 0422 UTC; 27 November 1995; d) 0502 UTC; 27 November 1995.

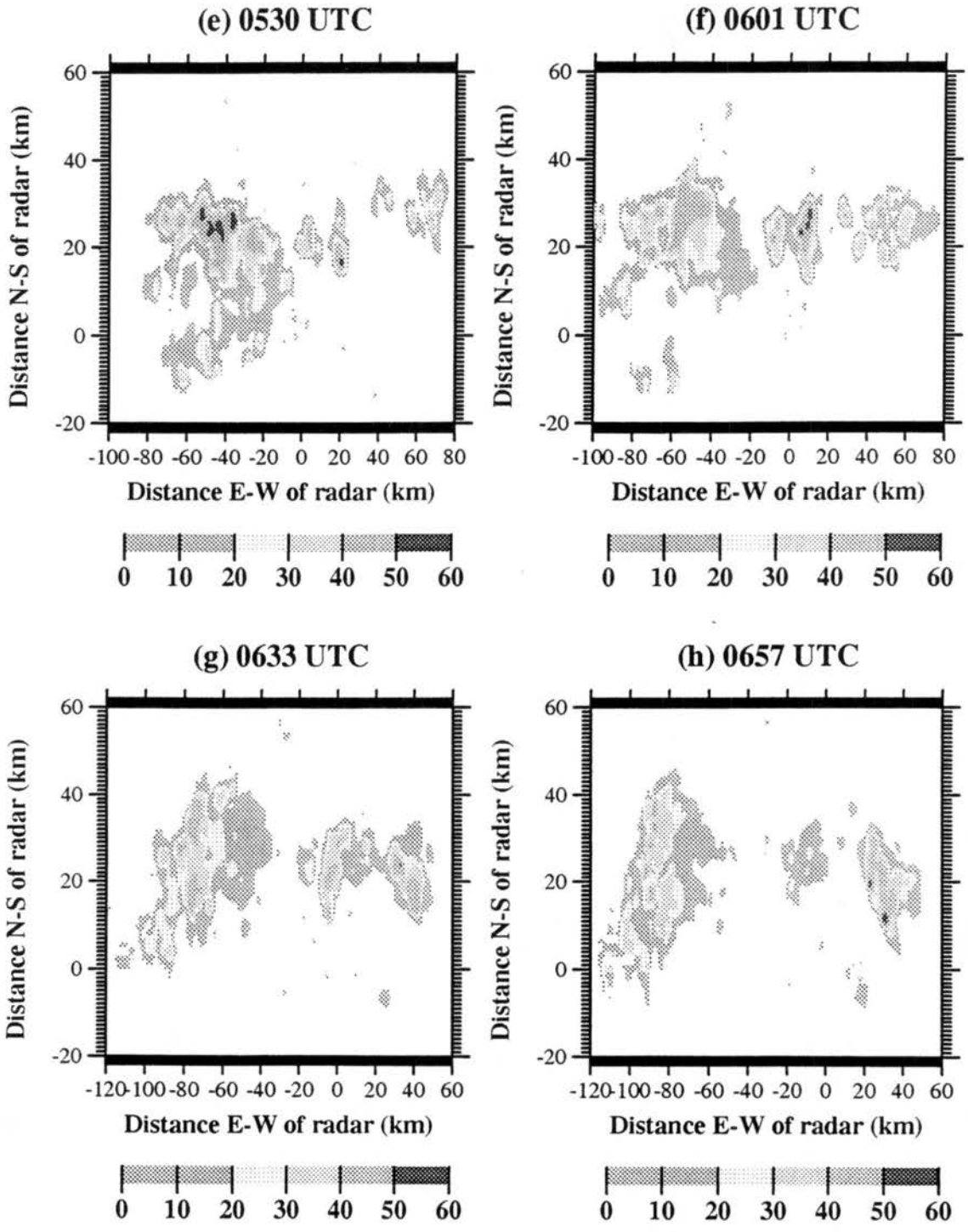

Figure 4.11 (e-h) Horizontal radar reflectivity cross sections at height of 1.5 km from the CPOL radar for: e) 0530 UTC; 27 November 1995; f) 0601 UTC; 27 November 1995; g) 0633 UTC; 27 November 1995; h) 0657 UTC; 27 November 1995. Notice changes in scale.

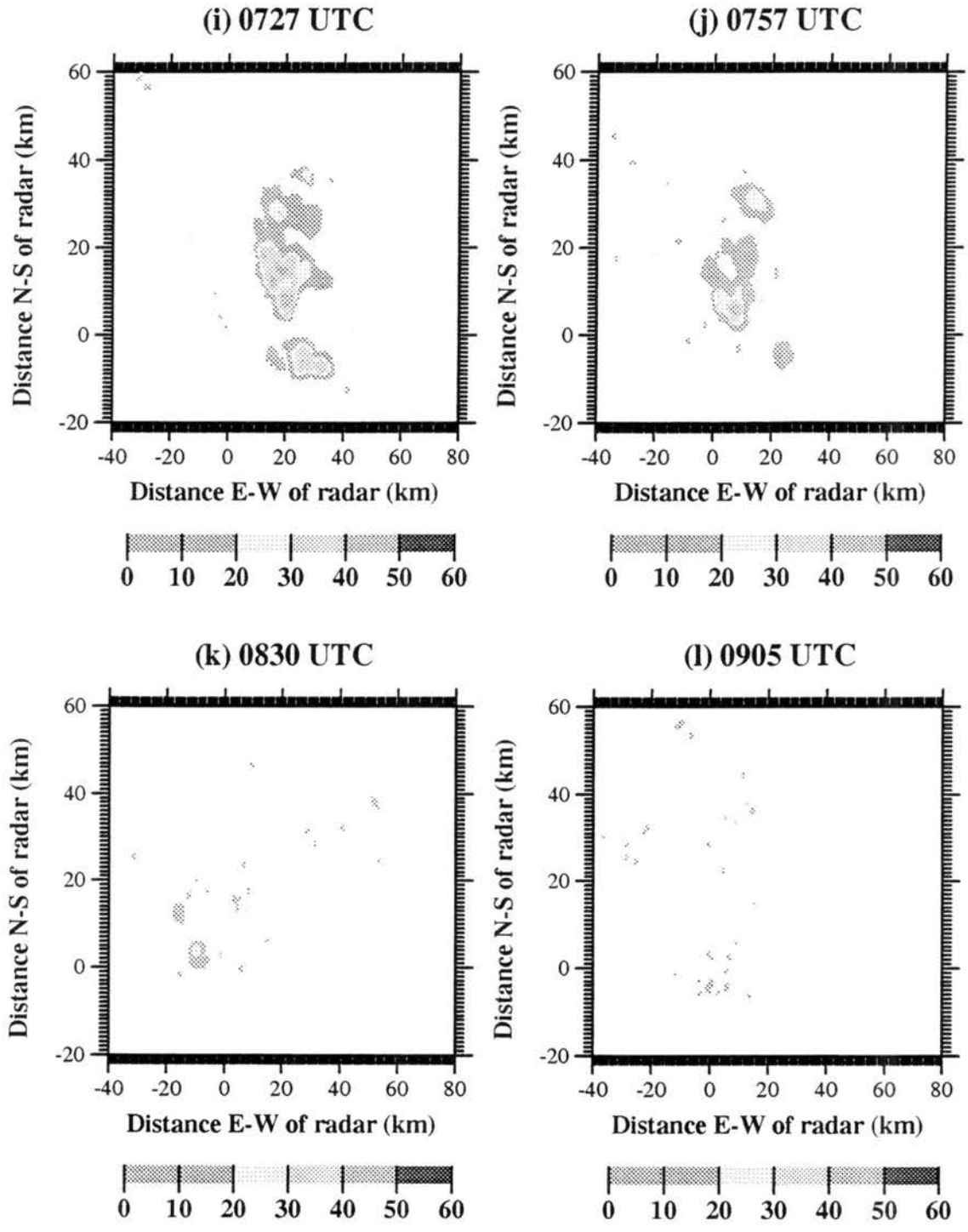

Figure 4.11 (i-l) Horizontal radar reflectivity cross sections at height of 1.5 km from the CPOL radar for: i) 0530 UTC; 27 November 1995; j) 0601 UTC; 27 November 1995; k) 0633 UTC; 27 November 1995; l) 0657 UTC; 27 November 1995. Notice changes in scale.

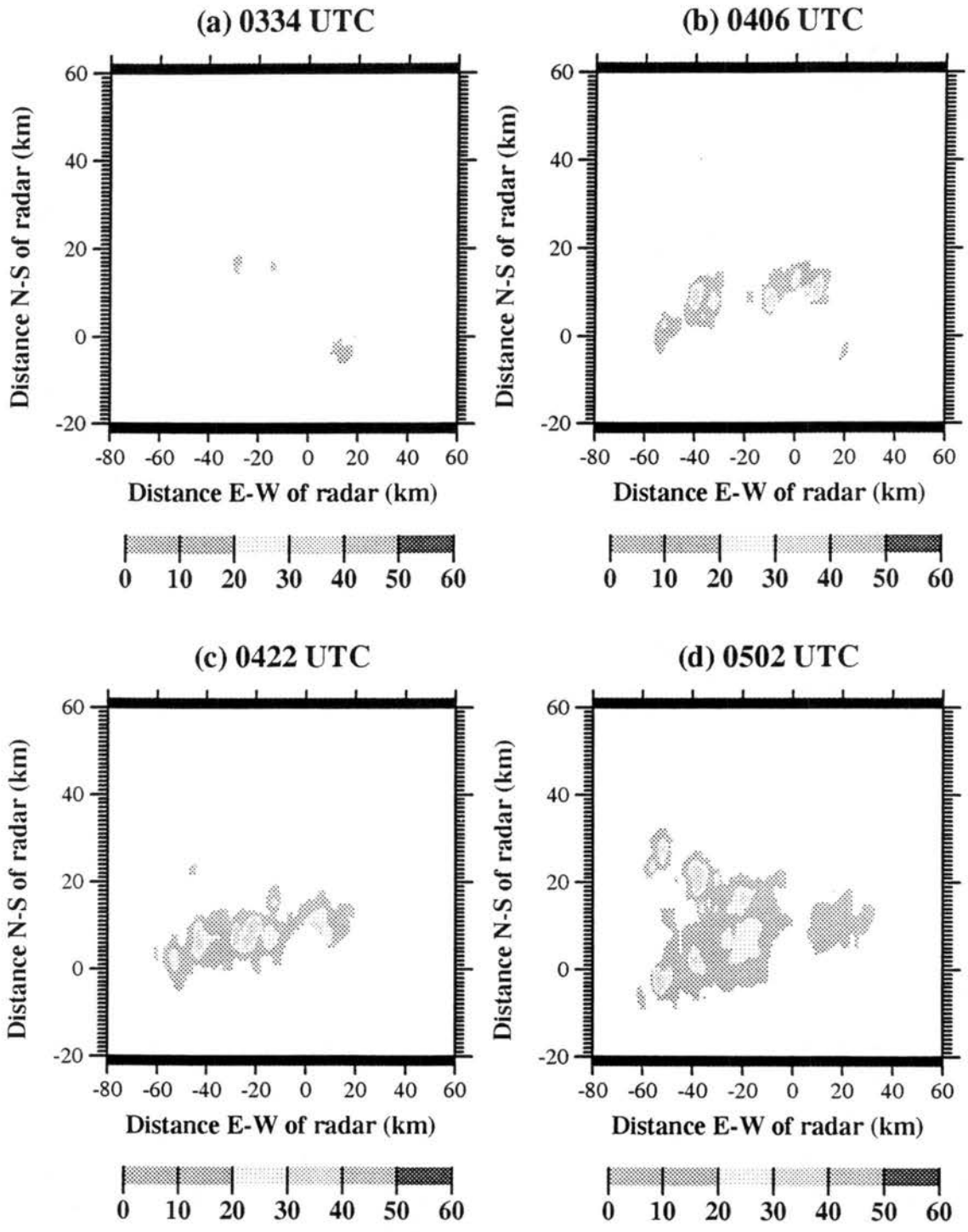

Figure 4.12 (a-d) Horizontal radar reflectivity cross sections at height of 9 km from the CPOL radar for: a) 0334 UTC; 27 November 1995; b) 0406 UTC; 27 November 1995; c) 0422 UTC; 27 November 1995; d) 0502 UTC; 27 November 1995.

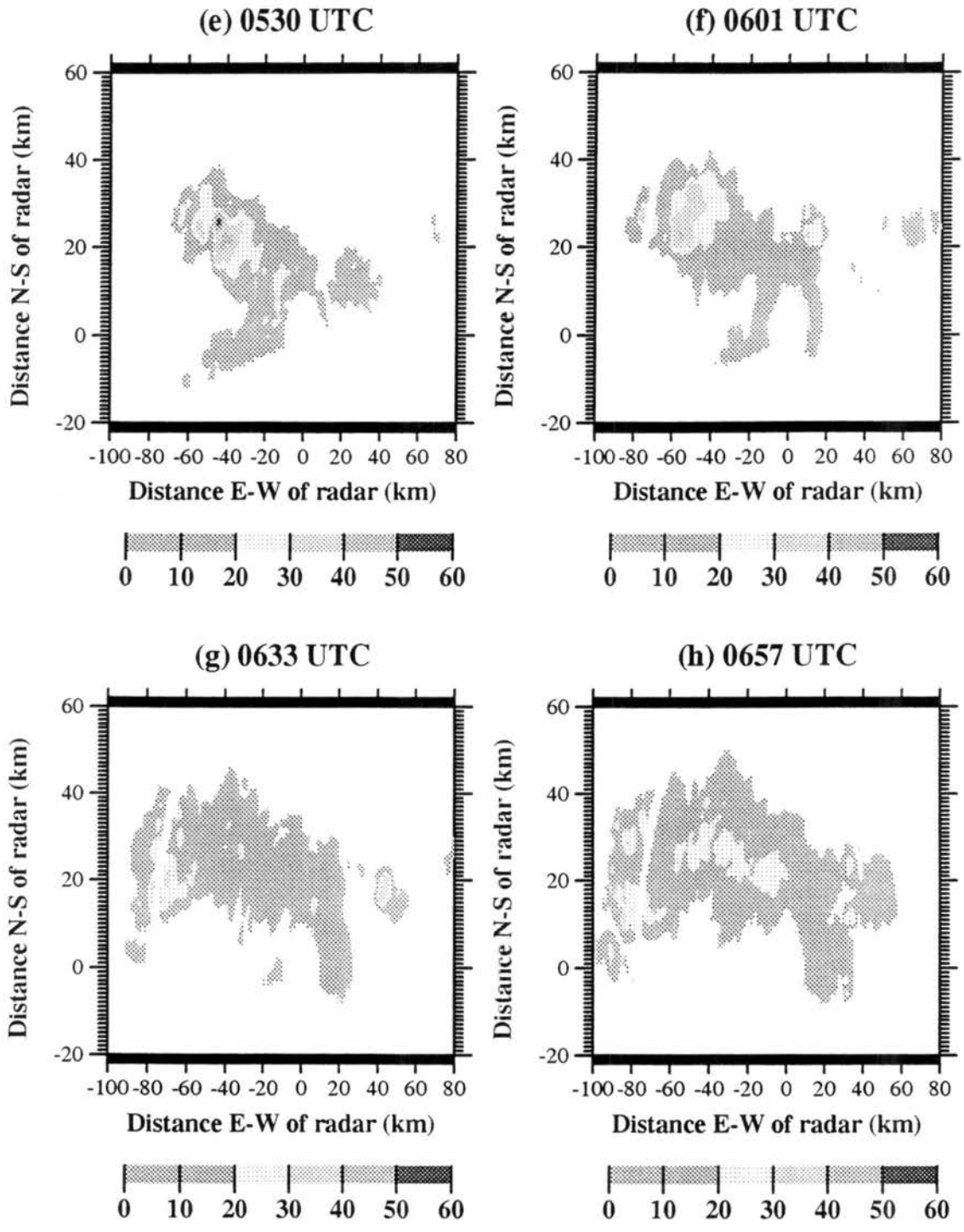

Figure 4.12 (e-h) Horizontal radar reflectivity cross sections at height of 9 km from the CPOL radar for: e) 0530 UTC; 27 November 1995; f) 0601 UTC; 27 November 1995; g) 0633 UTC; 27 November 1995; h) 0657 UTC; 27 November 1995. Notice changes in scale.

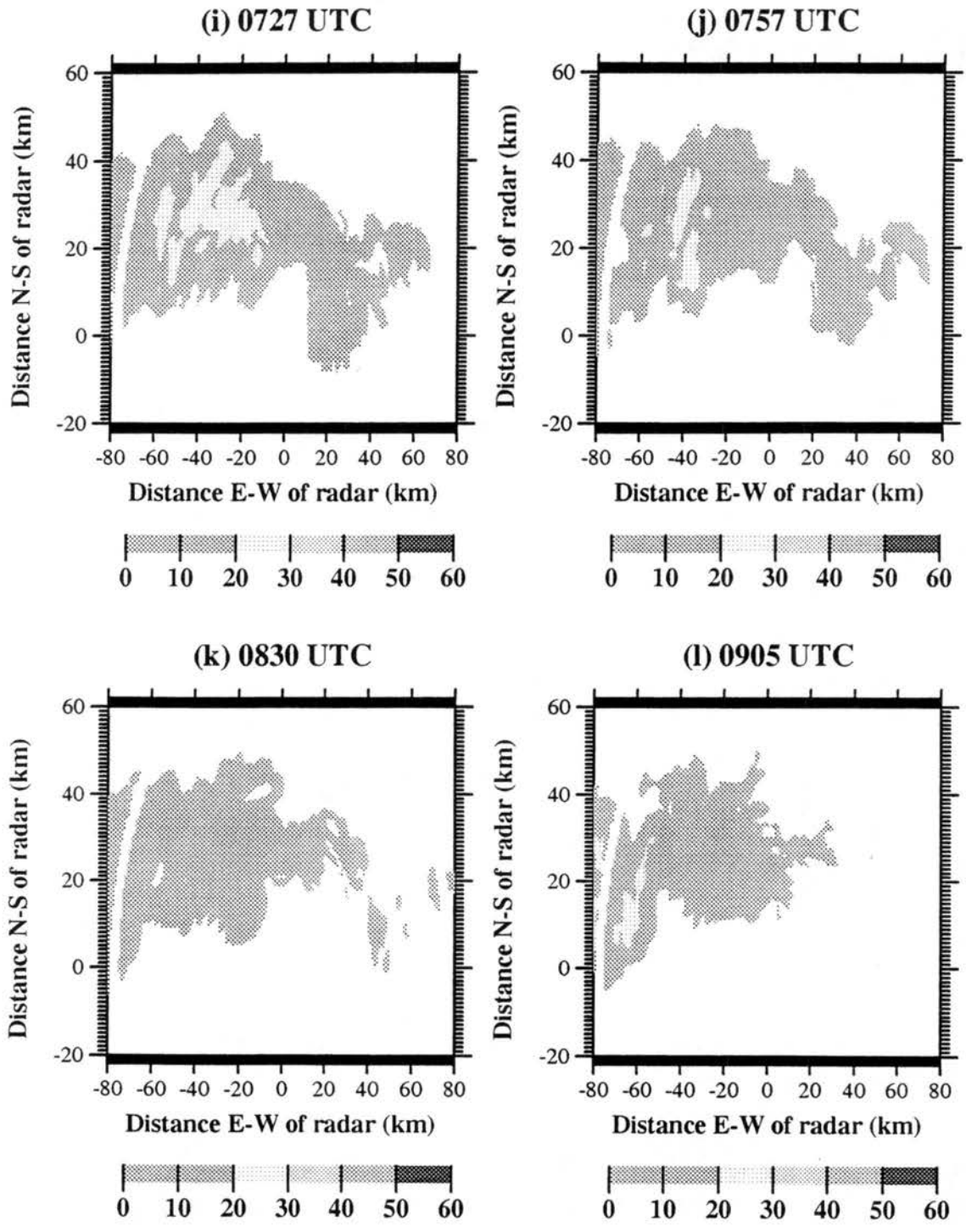

Figure 4.12 (i-l) Horizontal radar reflectivity cross sections at height of 9 km from the CPOL radar for: i) 0530 UTC; 27 November 1995; j) 0601 UTC; 27 November 1995; k) 0633 UTC; 27 November 1995; l) 0657 UTC; 27 November 1995. Notice changes in scale.

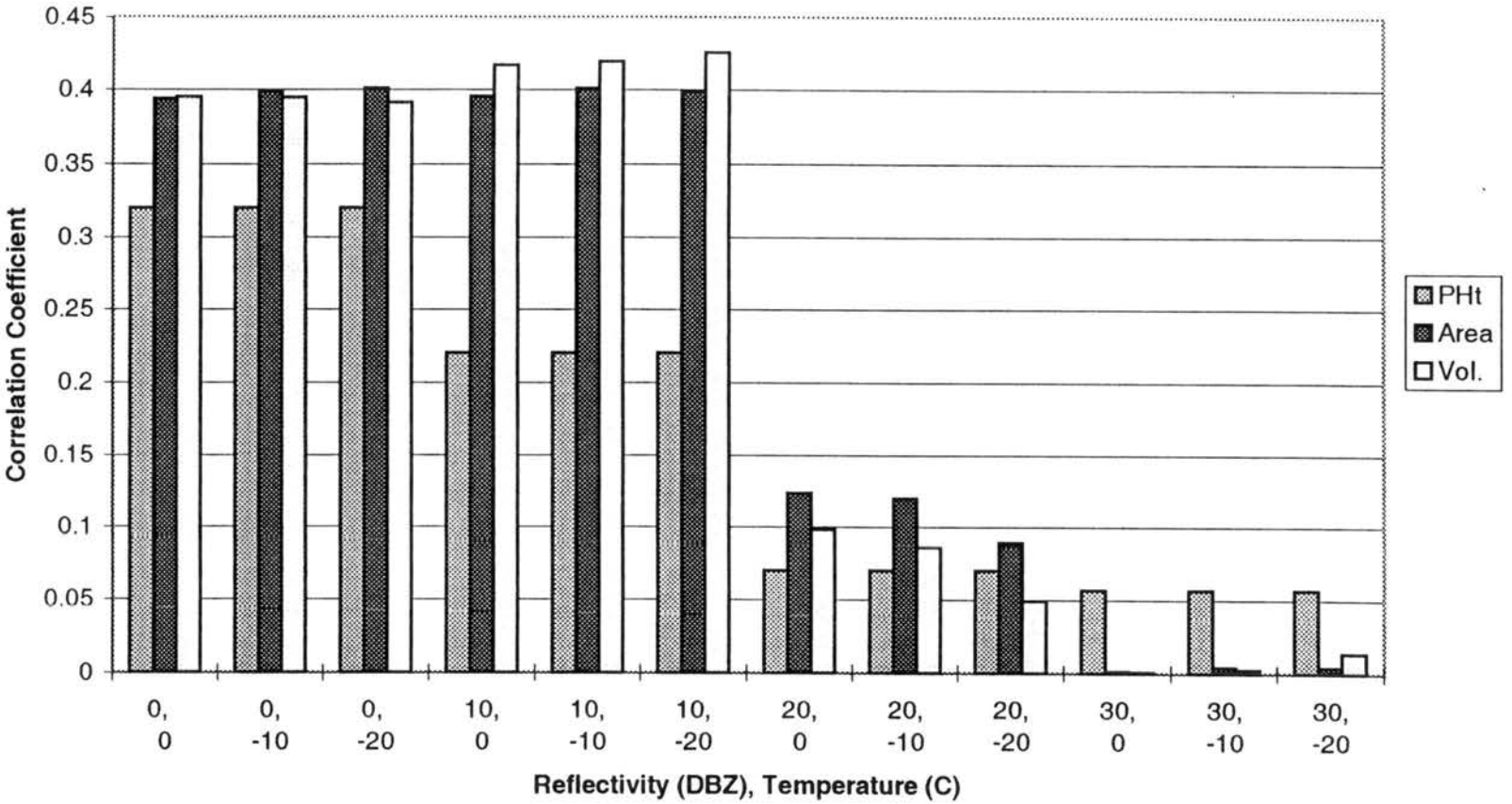

Figure 4.13 Correlation coefficients from linear regressions while varying temperature threshold for 27 November 1995 case.

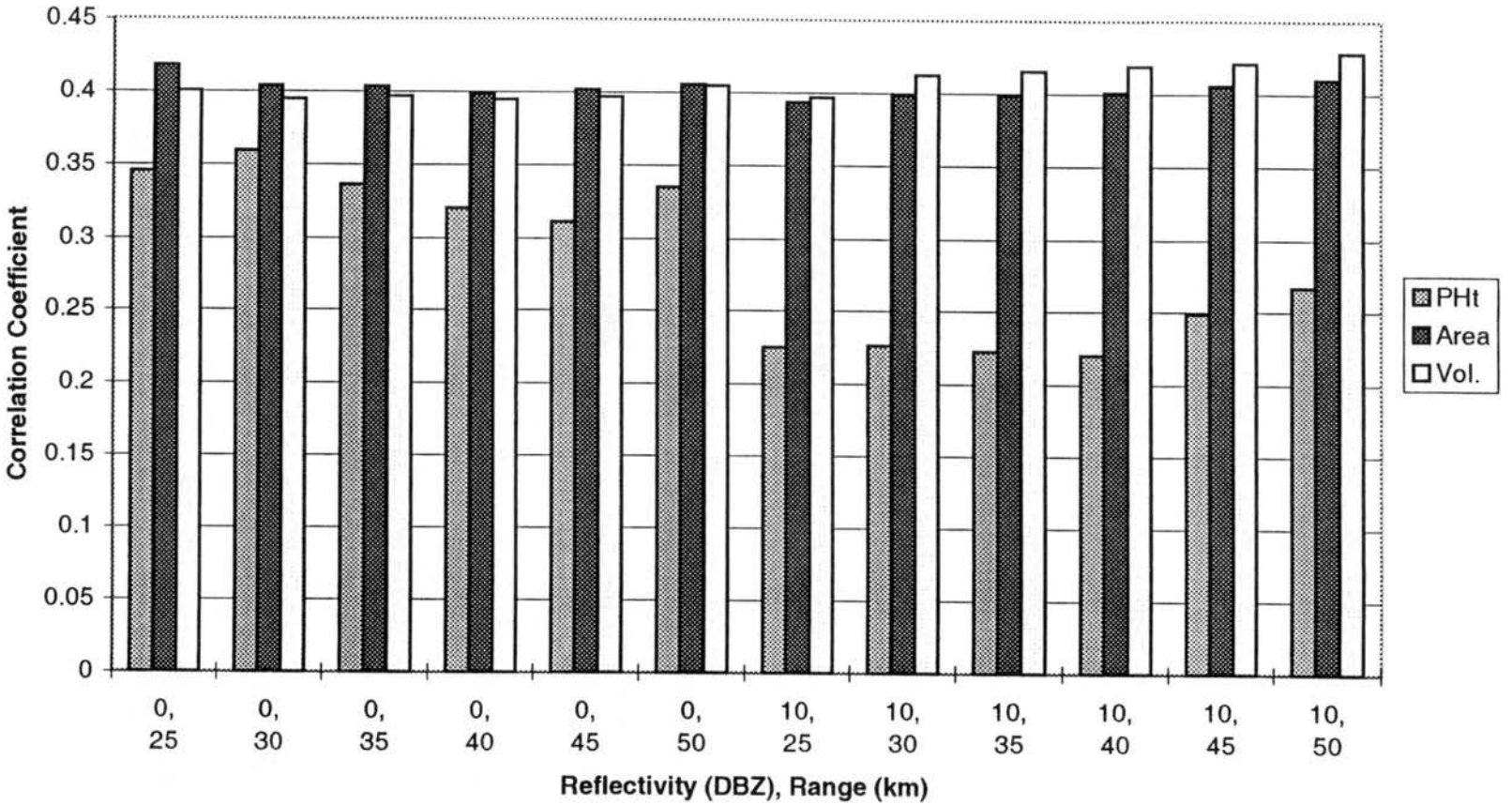

Figure 4.14 Correlation coefficients from linear regressions while varying range radar data were filtered. Shown are results for 0 and 10 dBZ for 27 November 1995 case.

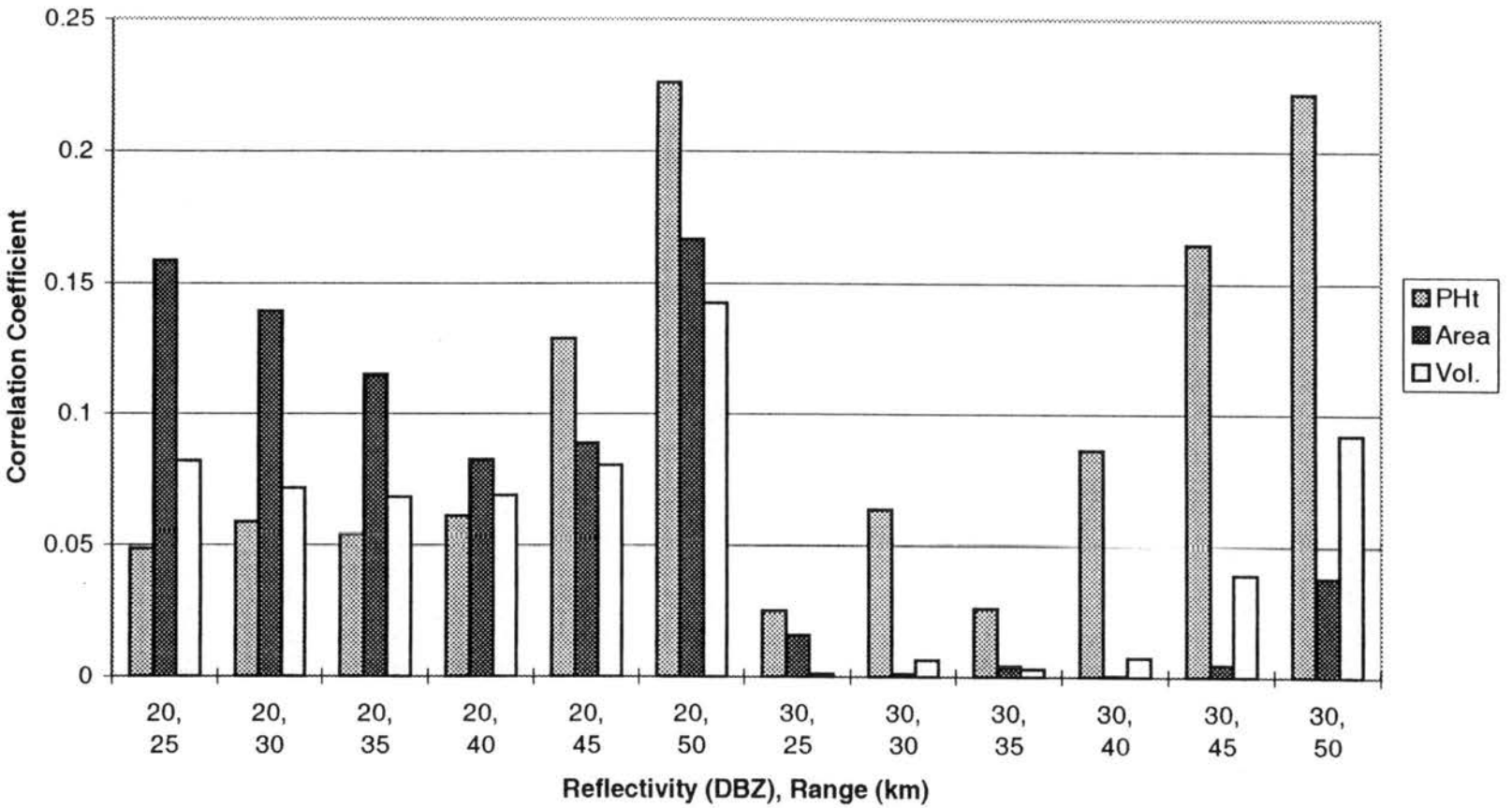

Figure 4.15 Correlation coefficients from linear regressions while varying range radar data were filtered. Shown are results for 20 and 30 dBZ for 27 November 1995 case.

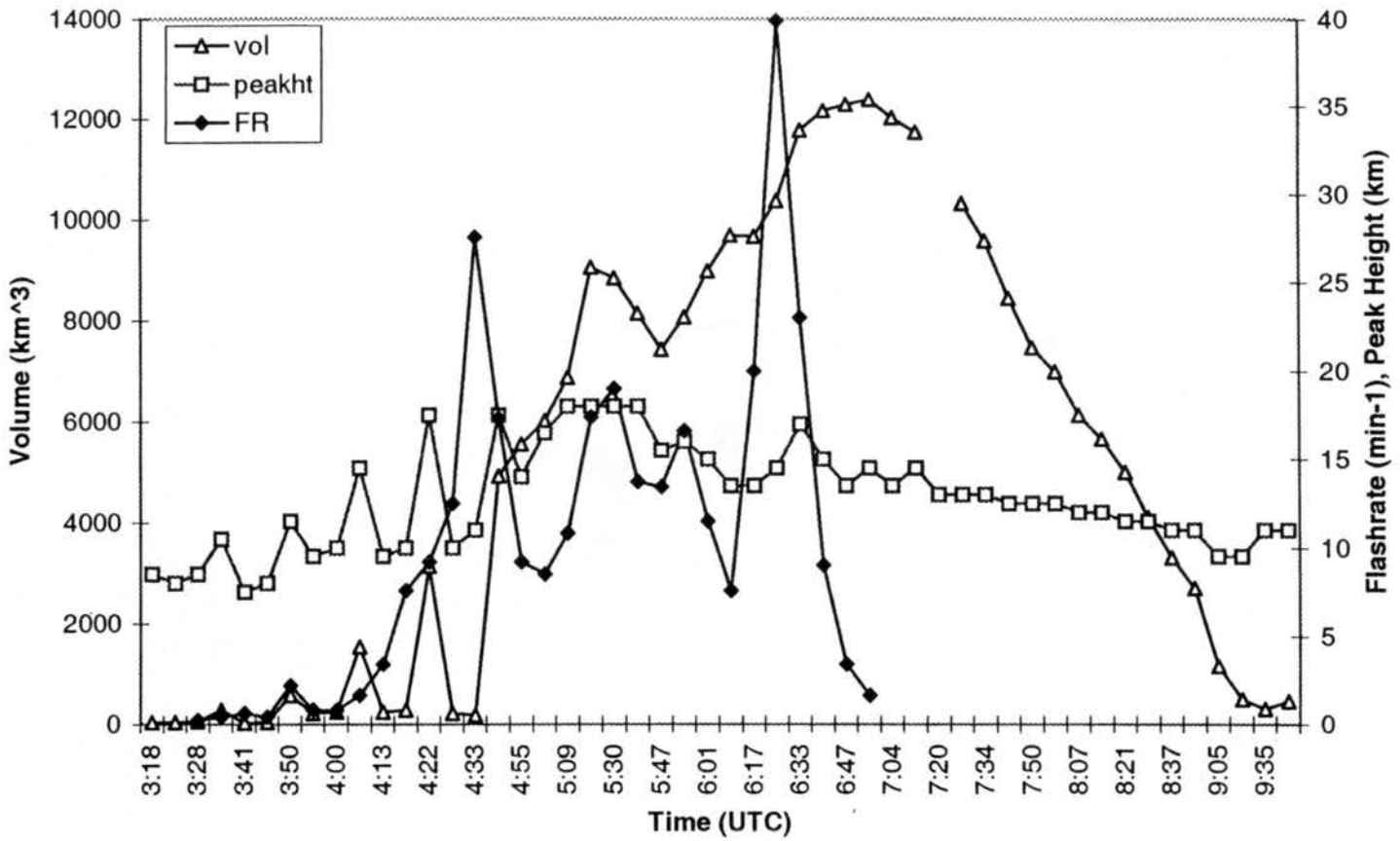

Figure 4.16 Time series of radar and lightning variables: 0318 through 0935 UTC 27 November 1995. Radar variables calculated using 50 km range filter and 10 dBZ and -10°C thresholds. Flash rates (min^{-1}) are five minute averages.

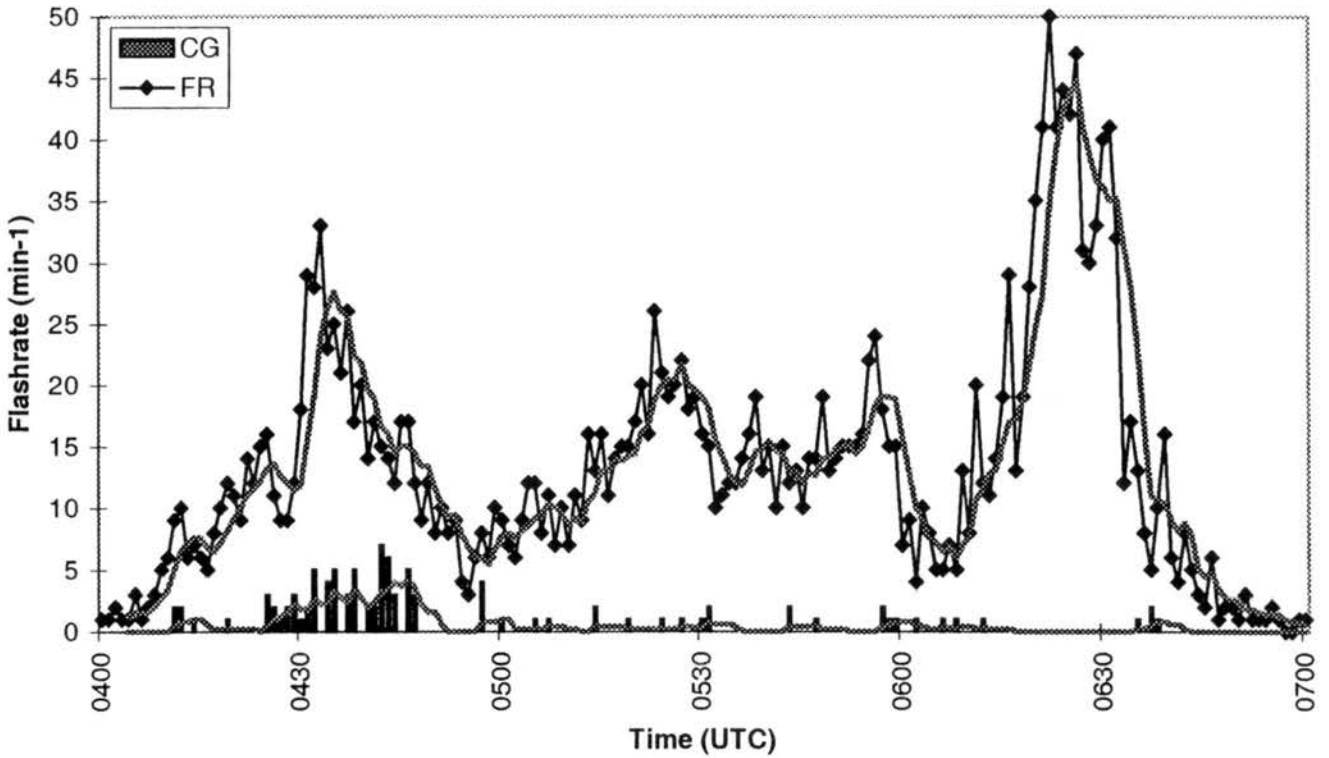

Figure 4.17 Time series of lightning flash rates from 27 November 1995 case. FR indicates total flash rate (min^{-1}). Five minute moving average of FR shown in thick gray line. CG indicates cloud-to-ground flash rate (min^{-1}).

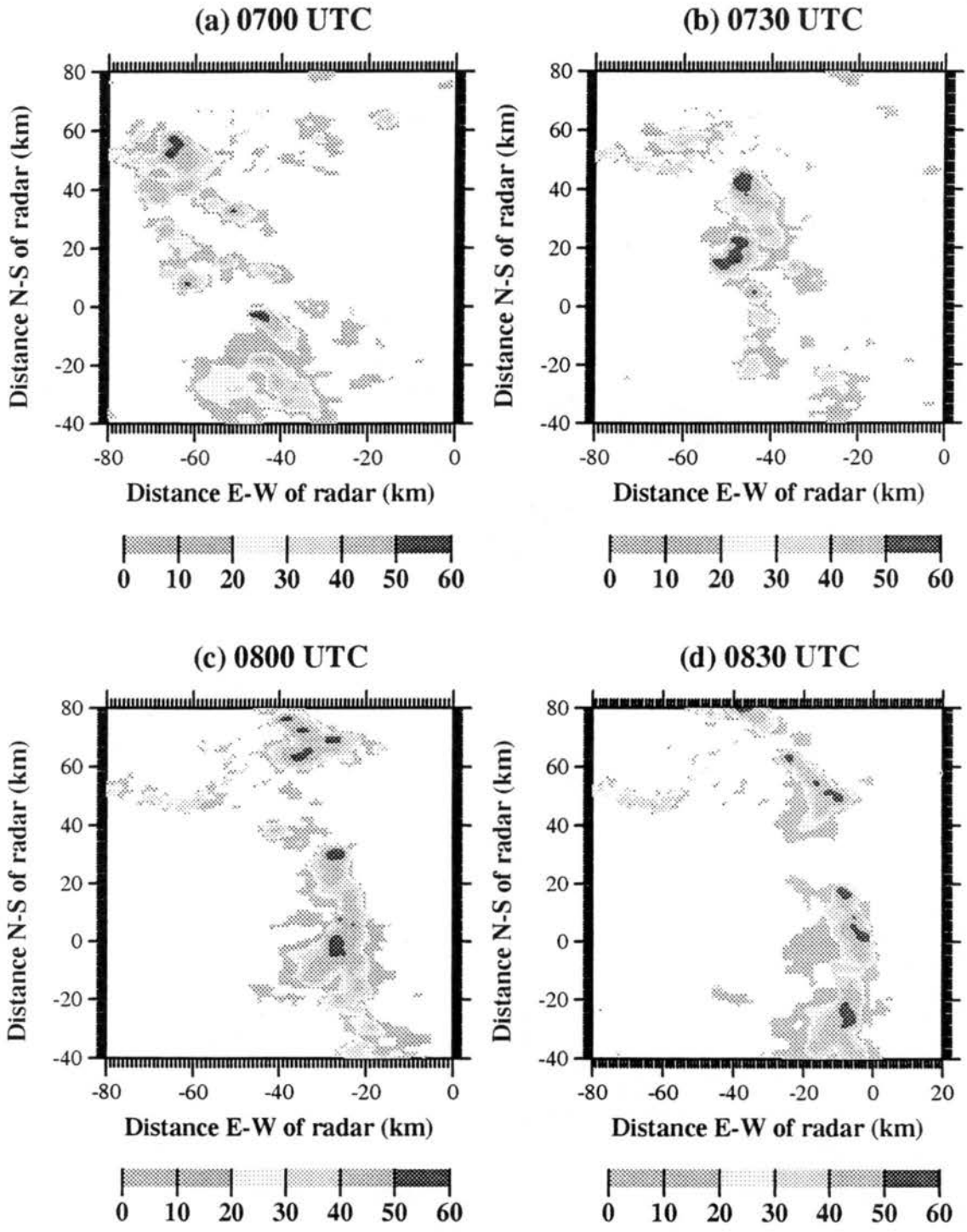

Figure 4.18 (a-d) Horizontal radar reflectivity cross sections at height of 1.5 km from the CPOL radar for: a) 0700 UTC; 29 January 1998; b) 0730 UTC; 29 January 1998; c) 0800 UTC; 29 January 1998; d) 0830 UTC; 29 January 1998.

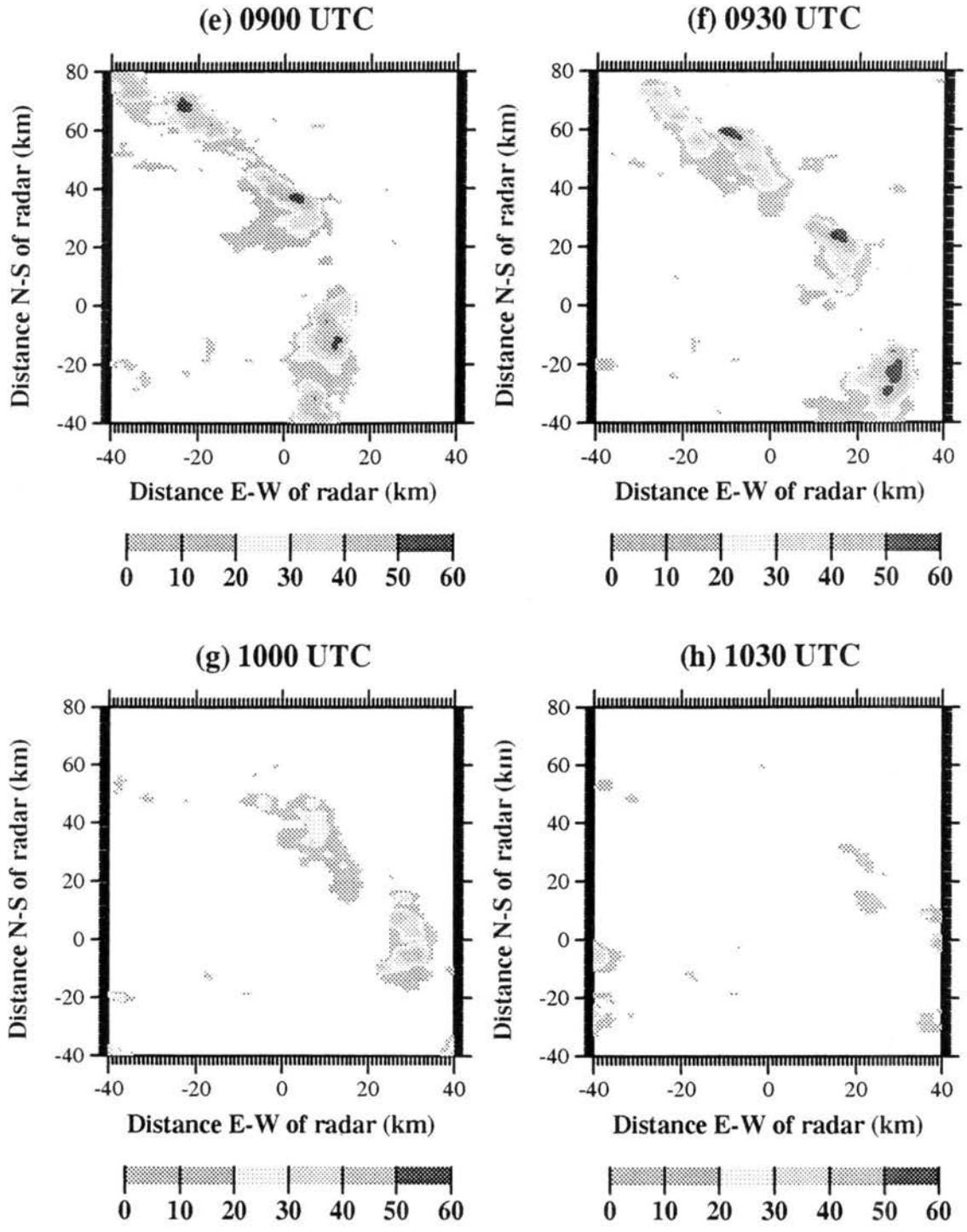

Figure 4.18 (e-h) Horizontal radar reflectivity cross sections at height of 1.5 km from the CPOL radar for: e) 0900 UTC; 29 January 1998; f) 0930 UTC; 29 January 1998; g) 1000 UTC; 29 January 1998; h) 1030 UTC; 29 January 1998. Notice changes in scale.

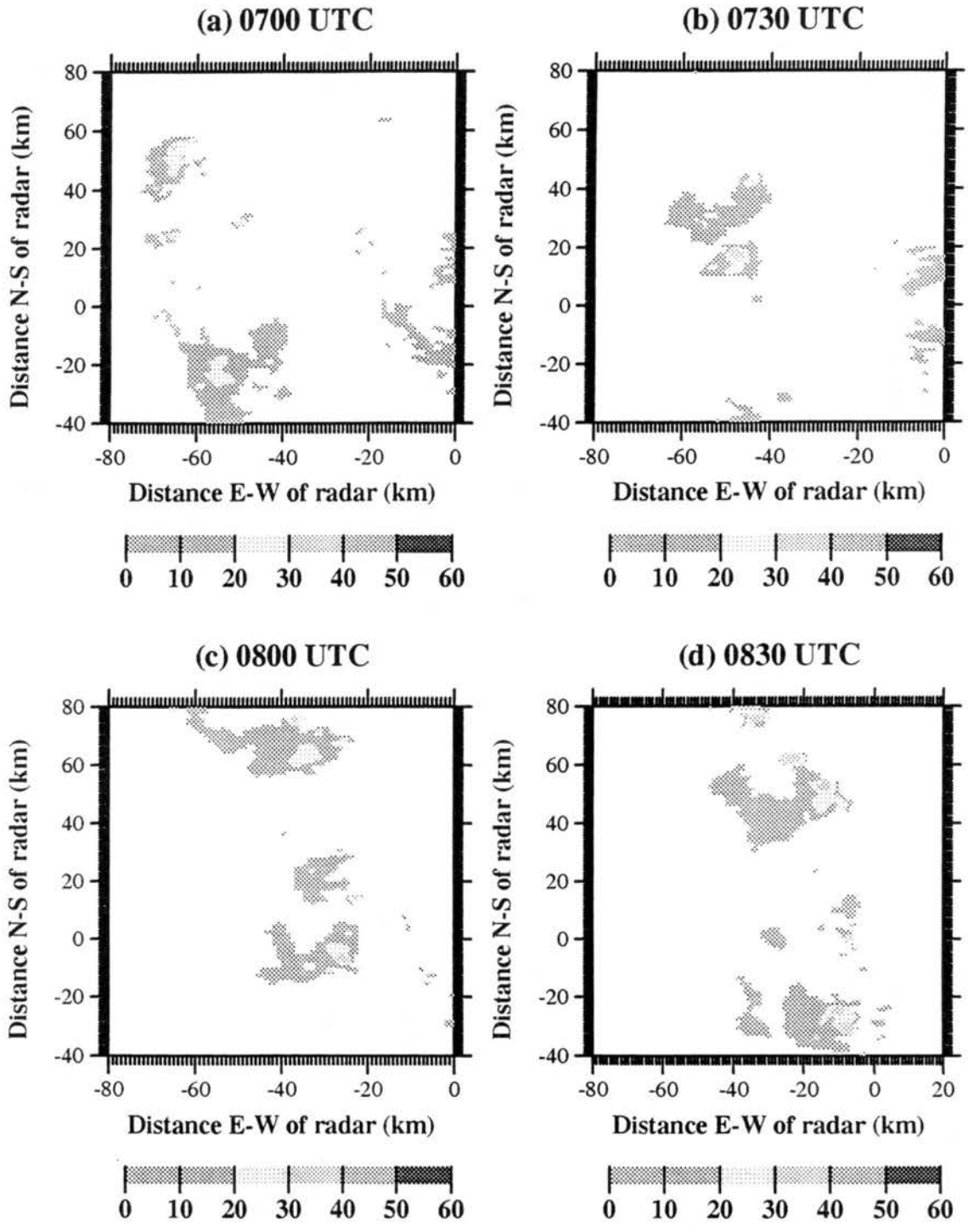

Figure 4.19 (a-d) Horizontal radar reflectivity cross sections at height of 7 km from the CPOL radar for: a) 0700 UTC; 29 January 1998; b) 0730 UTC; 29 January 1998; c) 0800 UTC; 29 January 1998; d) 0830 UTC; 29 January 1998.

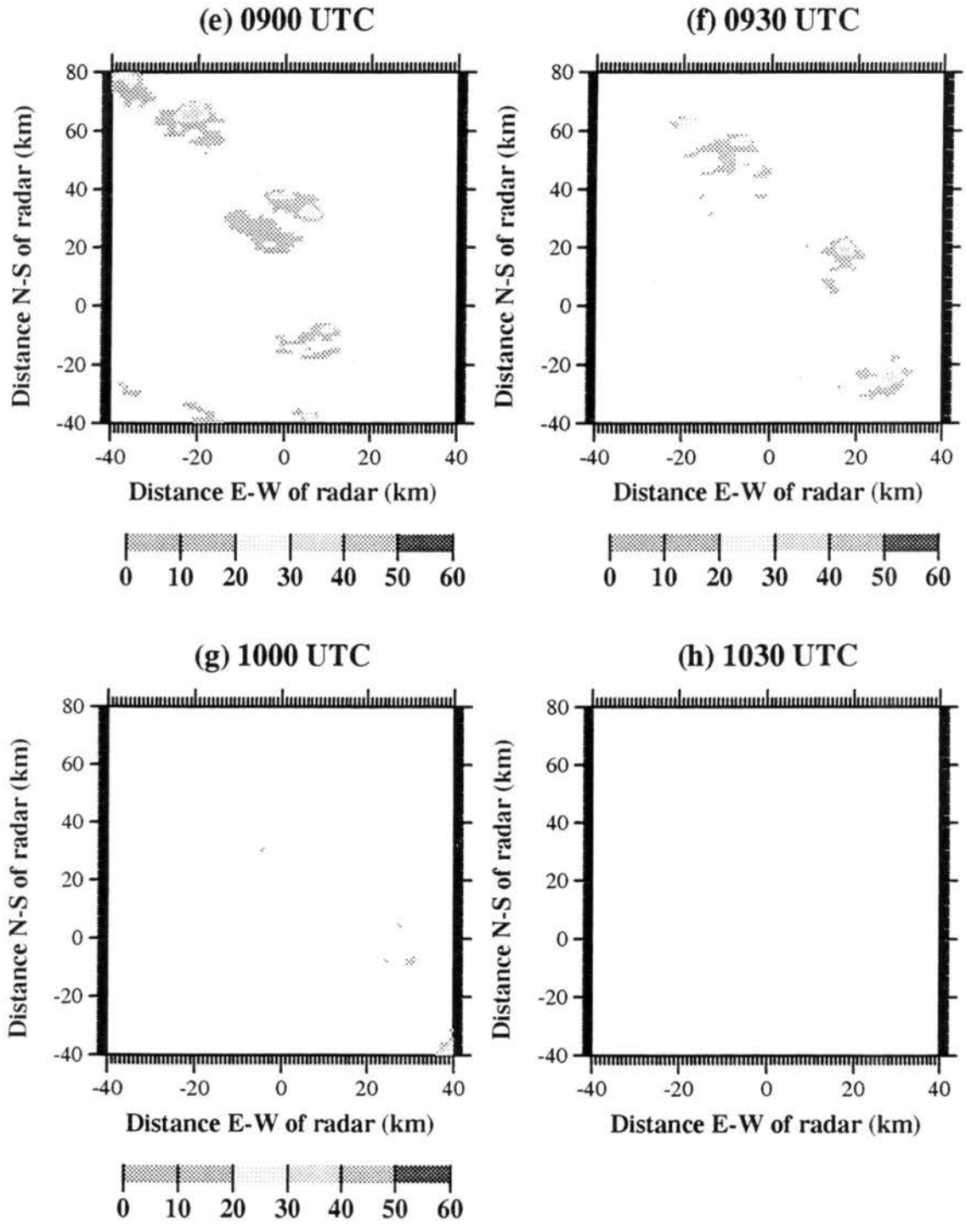

Figure 4.19 (e-h) Horizontal radar reflectivity cross sections at height of 7 km from the CPOL radar for: e) 0900 UTC; 29 January 1998; f) 0930 UTC; 29 January 1998; g) 1000 UTC; 29 January 1998; h) 1030 UTC; 29 January 1998. Notice changes in scale.

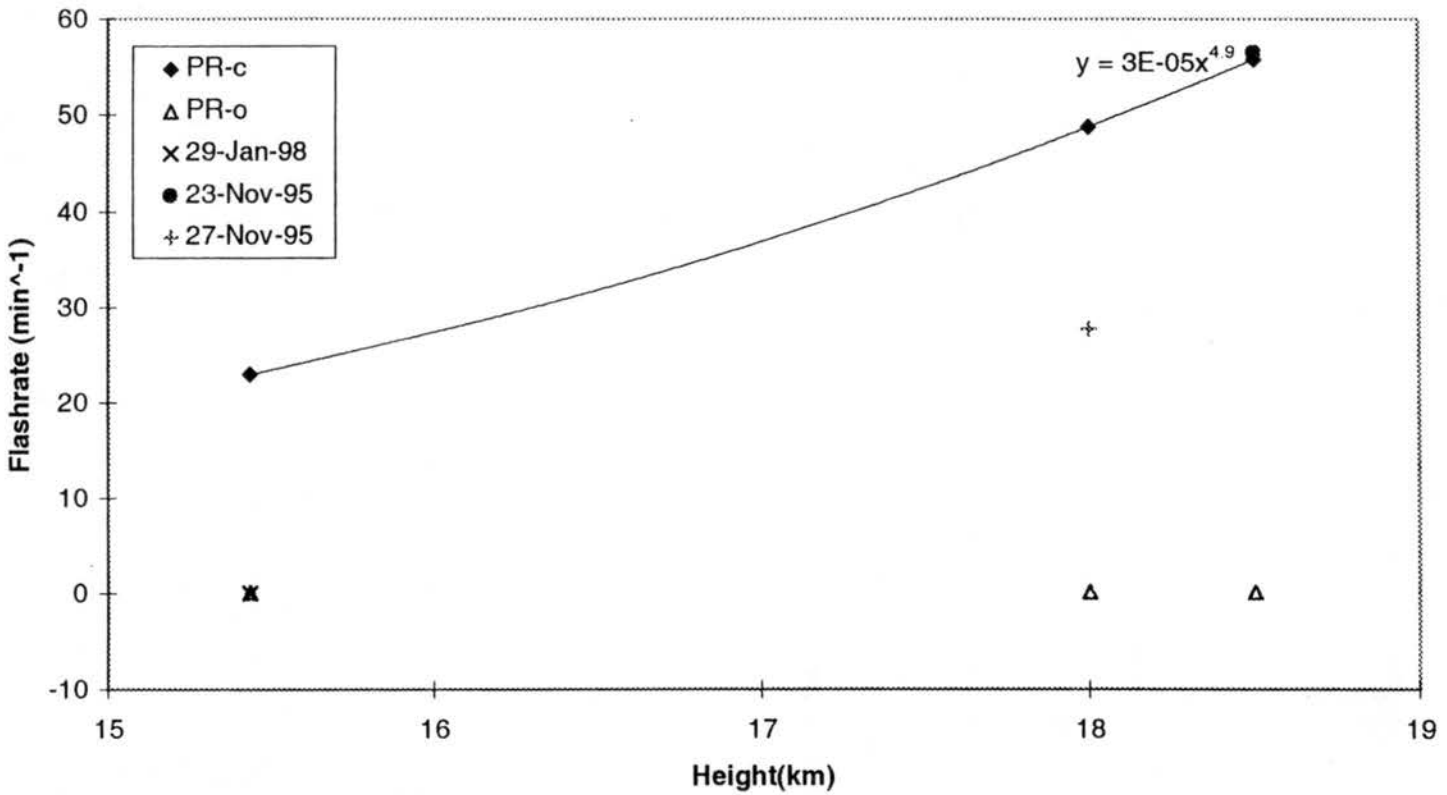

Figure 4.20 Total flashrate on the ordinate and cloud top height (as determined by the peak radar height for the case at 0 dBZ) on the abscissa. PR92 continental (PR-c) parameterization is solid curve with solid diamonds, while maritime (PR-o) parameterization is denoted by open triangles. The tropical Australian cases are plotted as described in legend.

CHAPTER 5

COMPARISONS AND CONCLUSIONS

Eight case studies have been presented, five mid-latitude and three tropical cases. In each case radar derived variables—height, area and volume as described in Chapter 2—and lightning characteristics were presented and compared. Here we will provide an overview of these cases as they relate to each other. We will then examine the trends between the lightning characteristics and several radar derived variables. Finally we will compare the results to past literature results and make suggestions for further research.

5.1 Trends between lightning and radar variables for all cases

In Chapters 3 and 4, we examined the detailed time series for the eight cases. We will now compare the radar and thermodynamic variables to the lightning variables for all the cases. Table 5.1 lists characteristics of each storm examined in this study. Abbreviations in this table are defined as follows: R, convective bulk Richardson number; LI, lifted index; mFR, peak total flash rate; TLIG, total storm flashes divided by storm duration in hours; TCG, total storm CG flashes divided by duration; %TM, percent total storm production rate (TLIG) divided by peak total flash rate (mFR); %IC, percent total storm IC flashes divided by total flashes; %+CG, percent total positive CG flashes divided by total CG flashes; Z, ratio of total IC flashes to CG flashes; CCTh, cold cloud thickness—the distance between the peak cloud top (defined as 0 dBZ) and the 0°C level; mHt, peak radar height; mA, area (defined in Ch. 2); mV, Volume (defined in Ch. 2); mVA, product of maximum volume and area; aVA, each time series product of volume and area averaged over storm duration; mHt^5, peak radar height raised to the fifth power.

Table 5.1 Overview of All Cases

Date	9 July	10 July	12 July	30 July-a	30 July-b	9 Aug.	23 Nov.	27 Nov.	29 Jan.	Units
Struct.	M_a	M_b/S_a	M_b	M_c	M_b	M_c	M_d	M_d	M_e	-
Dur.	1.8	4.3	3.5	1	3	1.1	2.5	3.3	2	hr
CAPE	236	792	441	-	-	-	1508	703	-	Jkg^{-1}
R	9.7	7.7	4.7	-	-	-	494	112	-	-
LI	-0.9	-2.8	-3.5	-	-	-	-2	-2	-	°C
mFR	30	42	67	17	89	70*	61	50	0	min^{-1}
TLIG	771	841	1352	477	1132	2797*	1217	752	0	hr^{-1}
TCG	273	17.9	102.6	35	206	3.6	95.2	30.8	0	hr^{-1}
%TM	43	33	34	47	21	-	33	25	-	-
%IC	65	98	92	93	82	99*	92	96	0	-
%+CG	5.9	17	10	0	39	100	6.3	1	0	-
Z	1.8	46	12.2	12.6	4.5	-	11.8	23.5	-	-
CCTh	11	12.5	10.5	10.5	13	-	14	12.5	9.5	km
mHt 0 dBZ	15.5	17	15	15	17.5	13	19.5	18	15	km
mHt 30 dBZ	12	14.5	13	12.5	15	12	17	17	8.5	km
mA 0 dBZ	7765	3291	5539	2829	5005	2714	2240	3415	2436	km^2
mA 30 dBZ	439	492	640	301	1250	156	340	287	98	km^2
mV 0 dBZ	$3.7x10^4$	$2.3x10^4$	$2.7x10^4$	$1.2x10^4$	$4.0x10^4$	$1.1x10^4$	$2.0x10^4$	$2.1x10^4$	$9.6x10^3$	km^3
mV 30 dBZ	$9.3x10^2$	$2.0x10^3$	$1.7x10^3$	$6.5x10^2$	$5.6x10^3$	$3.8x10^2$	$1.6x10^3$	$9.5x10^2$	$7.2x10^1$	km^3
mVA 0 dBZ	$2.9x10^8$	$7.5x10^7$	$1.5x10^8$	$3.5x10^7$	$2.0x10^8$	$2.9x10^7$	$4.5x10^7$	$7.1x10^7$	$2.3x10^7$	km^5
mVA 30 dBZ	$4.1x10^5$	$1.0x10^6$	$1.1x10^6$	$1.9x10^5$	$7.0x10^6$	$6.0x10^4$	5.410^5	$2.7x10^5$	$7.1x10^3$	km^5
aVA 0 dBZ	$1.4x10^8$	$4.9x10^7$	$9.9x10^7$	$2.9x10^7$	$1.0x10^8$	$1.8x10^7$	2.710^7	$2.9x10^7$	$9.7x10^6$	km^5
aVA 30 dBZ	$1.6x10^5$	$4.3x10^5$	$6.2x10^5$	$1.2x10^5$	$4.1x10^6$	$5.6x10^4$	$1.9x10^5$	4.810^4	$3.3x10^3$	km^5
mHt^5 0 dBZ	$9.0x10^5$	$1.4x10^6$	$7.6x10^5$	$7.6x10^5$	$1.6x10^6$	$3.7x10^5$	$2.8x10^6$	1.910^6	$7.6x10^5$	km^5
mHt^5 30 dBZ	$2.5x10^5$	$6.4x10^5$	$3.7x10^5$	$3.1x10^5$	$7.6x10^5$	$2.5x10^5$	$1.4x10^6$	$1.4x10^6$	$4.4x10^4$	km^5

M_a-multicellular embedded within stratiform; M_b-multicellular severe; M_c -multicellular non-severe
M_d-multicellular tropical non-propagating; M_e -multicellular tropical propagating
S_a- 'quasi'-supercellular; * For qualitative purposes only

All the cases exhibited multi-cellular structure during their lifetimes. However, the convective organization varied greatly among the cases. The organizational variations between the cases included a case with convection embedded within stratiform precipitation (J9), severe mid-latitude cases (J10, J12, J30b), a case with a period of "quasi-supercellular" structure (J10), non-severe mid-latitude cases (J9, Au9, J30a), tropical island cases (N23, N27), and a tropical rain-band case (JA29). The non-severe cases tended to have shorter lifetimes. The CAPE measured from soundings for the northeast Colorado cases did not seem to accurately represent the atmospheric instability. The high R (convective Richardson number) of the tropical island cases was consistent with convective structure and life-cycle characteristics (multicellular structure as opposed to supercellular, and shorter lived). The duration of the northeast Colorado cases (see Table 5.1) was a function of the length of time the storm existed in the ONERA Interferometer domain.

None of the case studies captured the entire lifetime of a storm. Especially short periods were captured for the J9 and A9 cases. The low R, driven by low level shear, caused the northeast Colorado cases to persist in organized convective complexes. Thus, R relates to the lightning production of storms by extending the lifetime and allows for higher production.

With the complex interactions between storm structure and the limited number of cases presented in this thesis, we can identify two general trends. First, mid-latitude severe storms (J10, J12 and J30b) produce greater peak total flash rates and total lightning production rates than non-severe mid-latitude storms. Current research indicates severe storms are accompanied by greater peak total flash rates than non-severe storms. More specifically, severe stages of storm life-cycle are preceded by intense increases in total flash rate (personal communication, S. Hodanish, 1998; P. Richard, 1996; W. Taylor, 1985). Second, some non-severe tropical island storms can have peak total flash rates and total lightning production rates equivalent to severe mid-latitude storms.

The lightning characteristics of the storms varied substantially. As mentioned in Chapter 3, the 9 August 1996 case will be considered only in a qualitative sense with regard to its flatplate derived total flash data. The storm production rate of all flashes ranged from 477 to 1352 per hour (except for 0 hr^{-1} for J29). The peak flash rate ranged from 17 to 89 flashes per minute (except for 0 min^{-1} for J29). The percent of IC flashes varied from 65% to 98%. Another way of expressing the IC fraction is Z, the IC to CG ratio. In

Section 5.2 we examine the relationship between Z and the cold cloud thickness (CCTh, defined as distance from cloud top to the 0°C level).

An example of the weakness of the PR92 parameterization follows. A comparison between the 0 dBZ reflectivity radar variables for the N23 and N27 cases (See Table 5.1) reveals that the values are similar or higher for the N27 case. At the higher thresholds (30 dBZ is shown in Table 5.1), the N23 case has distinctly higher values of the radar variables—particularly the area, volume and their product. The maximum flash-rate of the N23 case is 61 min^{-1} versus 50 min^{-1} for the N27 case. The total production rate is 1.6 times that of the N27 case (1712 hr^{-1} vs. 752 hr^{-1}). In this example, using mHt^5 , we would predict the total flash rate to be higher for the N27 case. However, the opposite is true.

Now we will examine the relationship between the radar variables and lightning flash rates. For the radar variables, we will use those which scale to the fifth dimension of length. The argument in Chapter 3 showed that the lightning flash rate, via the electrical power of the storm, was proportional to peak height raised to the fifth power (PR92) and also to the product of the area and volume of the storm. Linear regressions were calculated between data pairs from each case (excluding the A9 case). Six comparisons were made between three radar derived variables and two types of flash rate. The three radar derived variables included mVA, the product of the peak radar volume and peak radar area; aVA, the averaged value of the product of the volume and area; and mHt^5, the peak height raised to the fifth power. The two lightning flash rates were mFR, peak total flash rate, and TLIG, the average total storm flash production rate. These regressions were calculated for the different radar reflectivity thresholds using a -10°C temperature threshold. The -10°C temperature threshold was used because the regression studies at different temperatures in Chapter 3 and 4 indicated that colder temperatures created stronger trends between radar and lightning variables. In addition, the presence of radar reflectivity above the -10°C temperature level has been shown to be a necessary condition for the onset of lightning (Workman and Reynolds, 1949; Peterson et al., 1996).

Correlation coefficients were calculated for each regression (see Figure 5.1). To identify the effect of the stratiform precipitation for the J9 case, regressions were performed without the J9 case (see Figure

5.2). Regressions were also computed without the J30b case (see Figure 5.3). The first trend we identify in Figures 5.1 and 5.2 is that the correlation is predominately weaker between all radar variables and TLIG than the mFR. The stronger correlation between the radar variables and mFR (over TLIG) indicates a strong link between the radar inferred convective structure and instantaneous electrical activity within storms. In addition, the mFR may be directly related to electrical power of the storm. When the J30b case is excluded (see Fig. 5.3), the coefficients are similar for the 30 and 40 dBZ thresholds between TLIG and mFR (e.g. the coefficients are nearly identical for TLIG vs. mVA and mFR vs. mVA at 30 and 40 dBZ). A difference between the lightning characteristics of the J30b case and the other cases is the abrupt peaks in total flash rate (see Figure 3.21b). This difference leads to a correspondingly lower TLIG rate for the J30b case. This low TLIG rate explains the regression statistics in Figure 5.3 where the J30b case has been excluded.

The correlation between both lightning flash rates (TLIG and mFR) and the mHt^5 variable increases with higher reflectivity thresholds. It is consistently higher than $R^2 = 0.6$ and as high as $R^2 = 0.79$ for the 40 dBZ reflectivity threshold. Correlation above $R^2 = 0.4$ occur between mFR and aVA for reflectivities 10 to 40 dBZ and between mFR and mVA for 20 to 40 dBZ for the regressions including all cases (see Fig. 5.1). As an explanation for the increase of correlation at higher reflectivity thresholds, the higher reflectivity threshold isolates the radar parameters (height, area or volume) most closely associated with the charge separation processes. For example, stronger reflectivities within the region of strongest charge separation (guaranteed by the -10°C temperature threshold), ensures the presence of precipitation sized ice particles and convective vigor. Furthermore, convective vigor, as indicated by high reflectivities, ensures updrafts and therefore supercooled water droplets. This completes our list of requirements for charge separation in thunderstorms (see Chapter 1 Section 1).

A general increase in correlations for low reflectivities in Figure 5.2 (the regressions that exclude the J9 case) is explained by dropping the points from the regression for the J9 stratiform precipitation case. This case includes large portions of low reflectivity associated with widespread non-convective precipitation, which does not participate significantly in electrification, thereby skewing the correlation between radar variables and lightning flash rates when the case is included in regression calculations. These

increases in correlation for low reflectivity are most significant for the aVA and mVA for (see Fig. 5.2). Most interestingly, the correlation between mFR and the 0 dBZ reflectivity column of mHt^5 is the equivalent to the PR92 parameterization. Stronger correlations are found for almost all other reflectivities for the mVA and aVA variables. These correlations point to the weakness in the PR92 scale argument which neglects variations in horizontal scale (see Chapter 3, Section 6). In addition, stronger correlation is found for almost all higher reflectivity thresholds for mHt^5, particularly the 40 dBZ threshold. Thus, we have shown that a stronger trend exists between the peak total flash rate (mFR) and mHt5 for higher reflectivities, aVA and mVA than the cloud top height raised to the fifth power (as derived from the peak height at 0 dBZ).

5.2 Comparison to Past Research

First, we compare the cases to the parameterization developed in Price and Rind (1992) between total flash rate and cloud top height. In the previous chapters, Figure 3.21 and Figure 4.21 depicted the total flash rate versus the cloud top height raised to the fifth power (as derived by the 0 dBZ reflectivity threshold). In Figure 5.4, the cases are plotted on a log-log scale. The continental parameterization (PR92c—open triangles joined by line) as well as the maritime parameterization (PR92m—crosses joined by line) are compared with the data points from our cases. The JA29 null case falls along the maritime parameterization. The other two Australian cases fall near the continental line. Two northeast Colorado cases, J12 and J30b, lie above the continental line, even in the log-log plot. With the understanding that we are comparing only a few cases to the PR92 parameterizations, Figure 5.4 identifies two results. First, we have shown that mid-latitude storms can produce higher flash rates than predicted by the PR92 continental parameterization. Second, for regions exhibiting both continental and maritime influences, such as coastal or island regions (e.g., the Darwin region), the PR92 parameterizations alone will not adequately predict the total flash rate.

Price and Rind (1993) examined 139 cases of the relationship between the cold cloud thickness (CCTh)—the distance between the 0°C level and the cloud top—and the Z ratio (total IC/total CG). Figure

5.5 shows the points from the seven cases (all but JA29 and AU9) in CCTh-Z space. The authors give a polynomial equation for predicting Z from CCTh ($Z= 0.021CCTh^4 - 0.648CCTh^3 + 7.493CCTh^2 - 36.54CCTh + 63.09$). All of our data points, except the J10 case, fall near the prediction. The J10 case exhibits a Z of 45.9 and a CCTh of only 12.5 km. These results are noteworthy since Price and Rind (1993) have only one comparable point in the region of high Z (Z of 47 and a CCTh of 14.5 km).

5.3 Conclusions and Suggestions for Future Research

The primary objective of this work was to determine if more effective predictors of lightning flash rates than cloud top height raised to the fifth power could be identified. In Chapters 3 and 4, we showed regressions for individual cases between radar variables (peak height, area, volume, and area volume products) and flash rates. These regressions exhibited stronger correlations than between total flash rate and cloud top height raised to the fifth power (derived from 0 dBZ peak height), especially at higher reflectivity thresholds. In this chapter, we examined radar derived variables scaled to the length raised to the fifth power. Linear regressions between our cases' radar variables and flash rates, both peak flash rate (mFR) and total production (TLIG), exhibited a number of correlations stronger than that of cloud top height raised to the fifth power (mHt^5 at 0 dBZ, denoted H_0^5). Correlations between mHt^5 at higher reflectivity thresholds and both mFR and TLIG were higher than H_0^5. In addition, correlations between both the product of the peak volume and area variables (mVA) and the averaged product of volume and area (aVA) and both of the flash rates (mFR and TLIG) were stronger than H_0^5. Thus, we have shown that the radar variables aVA, mVA and mHt^5—mHt^5 particularly at higher reflectivity thresholds—are more effective predictors of total flash rate than cloud top raised to the fifth power. The essential reason that these variables are better predictors at the higher reflectivity thresholds is they quantify the size of the charge generating regions of the storms.

The J9 case had large regions of low reflectivity associated with stratiform precipitation (see Fig 3.13a-h). These regions are not associated with significant charge generation and can be partitioned when using the radar variables to predict total flash rates by using higher reflectivity thresholds. By using radar variables at higher reflectivities, total flash rates could be predicted for complex convective structures that

may have associated stratiform precipitation or even upper level low reflectivity anvil regions not associated with charge generation.

We found that there is a difference in the correlations between the radar variables and the two lightning flash rate variables (mFR and TLIG). An example of this difference is exhibited by the J30b case. This case, which had very periodic lightning cycle, showed a disparity compared to other cases in its averaged production of flashes (TLIG) and the peak flash rate (mFR). This disparity caused an increase in correlation between the radar variables and the averaged production of flashes (TLIG) when the case was omitted from the regression analysis. A general trend was found toward an increased correlation between all radar variables and the mFR over TLIG. The mFR is directly related to the instantaneous convective structure (which relates more directly to the radar variables than the TLIG) and to the electrical power of the storm than the TLIG. If investigating the impact of lightning on the NO_x chemical budget over longer time scales, we would prefer to predict TLIG rather than mFR. This work has shown that correlations still exist between TLIG and radar variables, even if they are weaker than those between mFR and radar variables.

The emphasis of this work was to determine variables which can predict the lightning behavior, recognizing that a variety of storm structures can be observed. Some regions see different regimes under which specific conditions may warrant different prediction techniques of lightning flash rate. An example of such a region is the Darwin area. This coastal region can have both continental and maritime influences. Obviously, these influences can have a profound impact on the electrical nature of convective events. The three cases in this study from the Darwin region have shown that it is possible to have total flash rates characteristic of both continental or maritime storms. The examination of these three cases has not been an attempt to quantify the trends between flash rates in this region, or in the tropics. Rather, these cases were included to add to the investigation of the relationship between the radar variables and lightning flash rates, and to illustrate that significant deviations from PR92 can occur in coastal regions.

The results of this thesis suggest that for modeling lightning production, especially on regional or smaller scales, caution should be taken when assuming simple cloud top parameterizations of flash rates. In addition, more complex parameterizations are needed for regions that encounter both continental and

maritime influences. This work has identified radar derived variables which are more closely linked to thunderstorm electrification than cloud top height. Further research could investigate relating modeling-generated variables, for example mixing ratios and radar reflectivity, generated by bulk-microphysical models, to lightning flash rates (e.g. Ferrier,1994; Ferrier et al., 1995). Further improvements in lightning parameterization could also be investigated by using the multi-parameter radar data to characterize the bulk microphysics in electrified thunderstorms. Additionally, future investigation with the addition of dual-doppler radar data sets could produce predictors tied to variables such as divergence, updraft speeds and mass fluxes. These variables could be linked to convective parameterization in global climate models to improve prediction over simple cloud height parameterizations.

Improving knowledge of lightning flash-rates in storms will help researchers assess the effect of a time dependent NO_x source from lightning (LNO_x). Due to the short lifetime of NO_x in the atmosphere coupled with the injection altitudes of the lightning source, the uncertainty in the LNO_x is that much more important to unravel. In addition to addressing the lightning frequency, it is also important to address the issue of NO_x production per flash for both IC and CG lightning. This issue is under investigation from a combined observational and modeling approach with the STERAO-A project (personal communications, K. Pickering, 1998; Skamarock, 1998). Any improvements in the estimates of the LNO_x source will further the understanding of NO_x chemistry on the atmosphere's oxidizing capacity, global climate change and the tropospheric ozone budget.

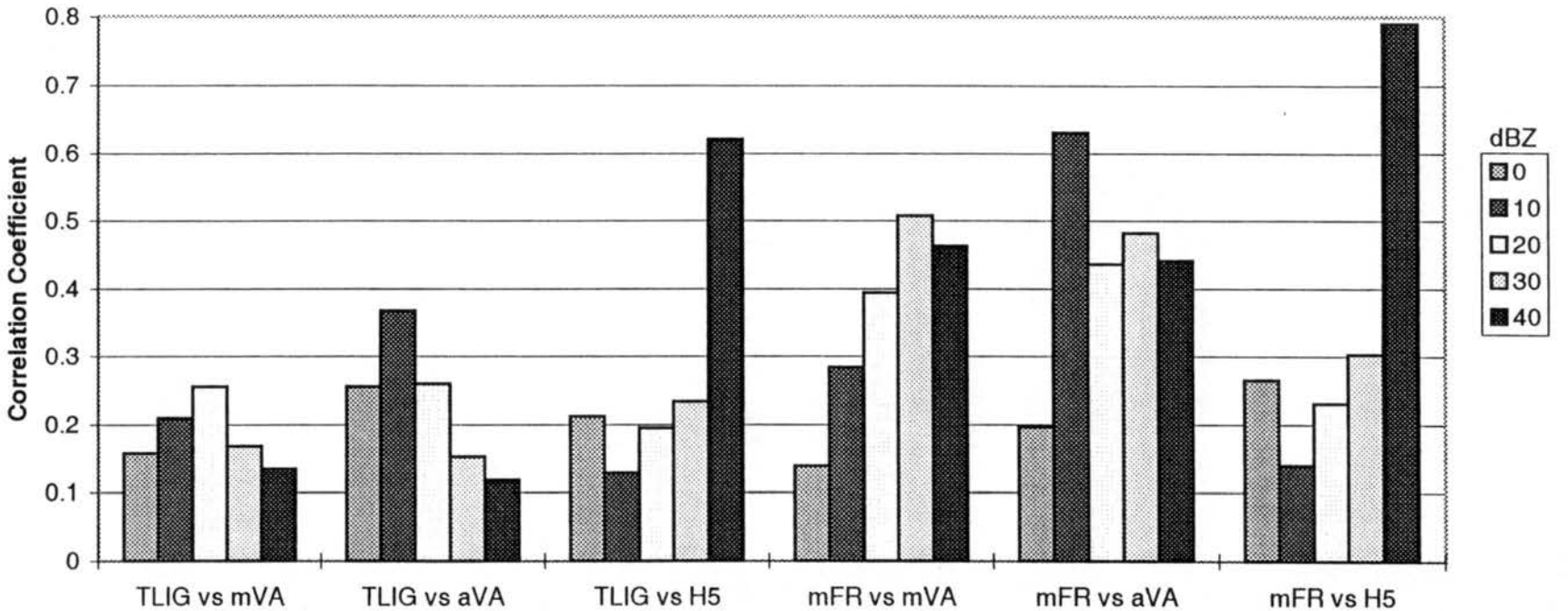

Figure 5.1 Correlation coefficients between lightning variables and radar variables, for all cases except A9. TLIG: production rate of total lightning; mFR: peak total lightning flash rate; mVA: peak volume, area product; aVA: averaged volume, area product; H5: peak height raised to fifth power.

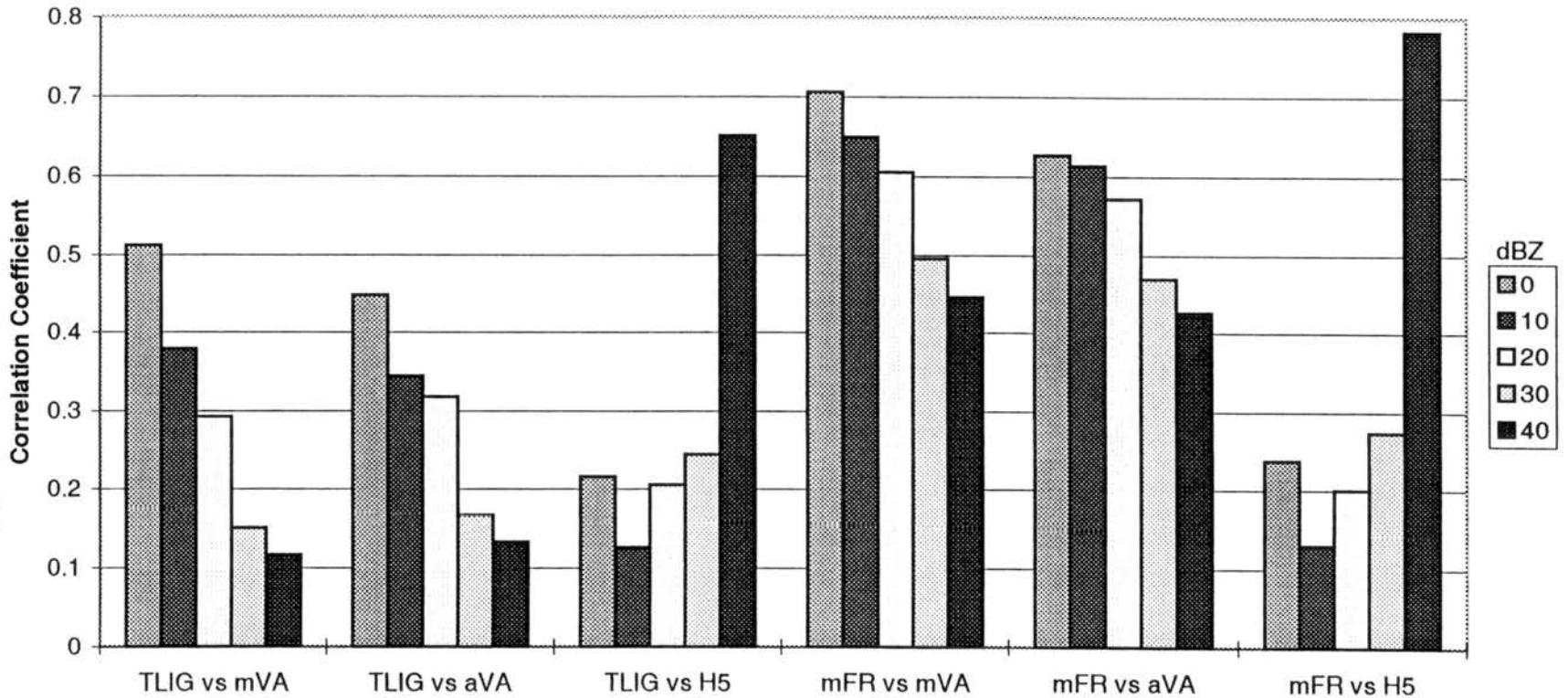

Figure 5.2 Correlation coefficients between lightning variables and radar variables, for all cases except A9 and J9. Abbreviations as in Fig. 5.1.

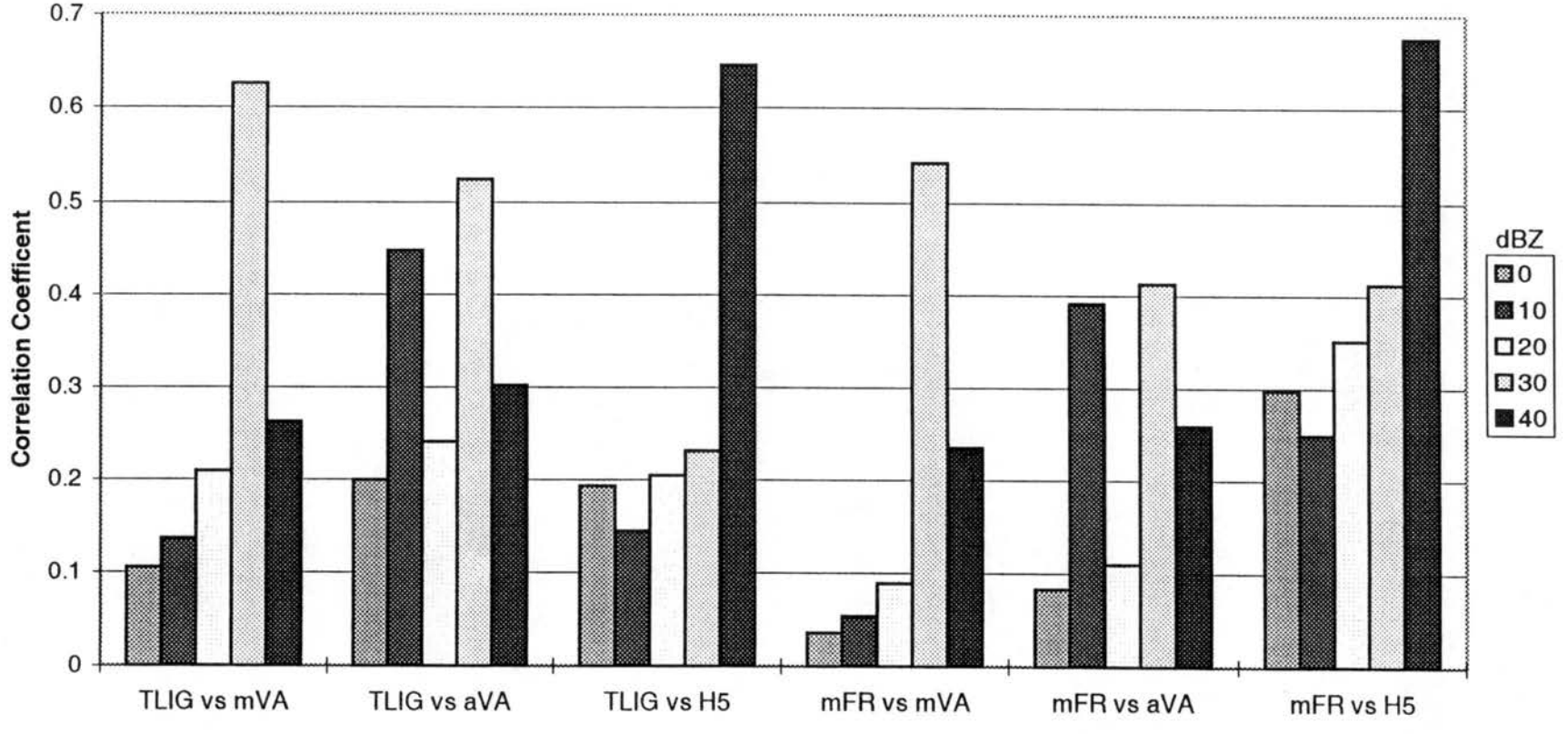

Figure 5.3 Correlation coefficients between lightning variables and radar variables, for all cases except A9 and J30b. Abbreviations as in Fig. 5.1.

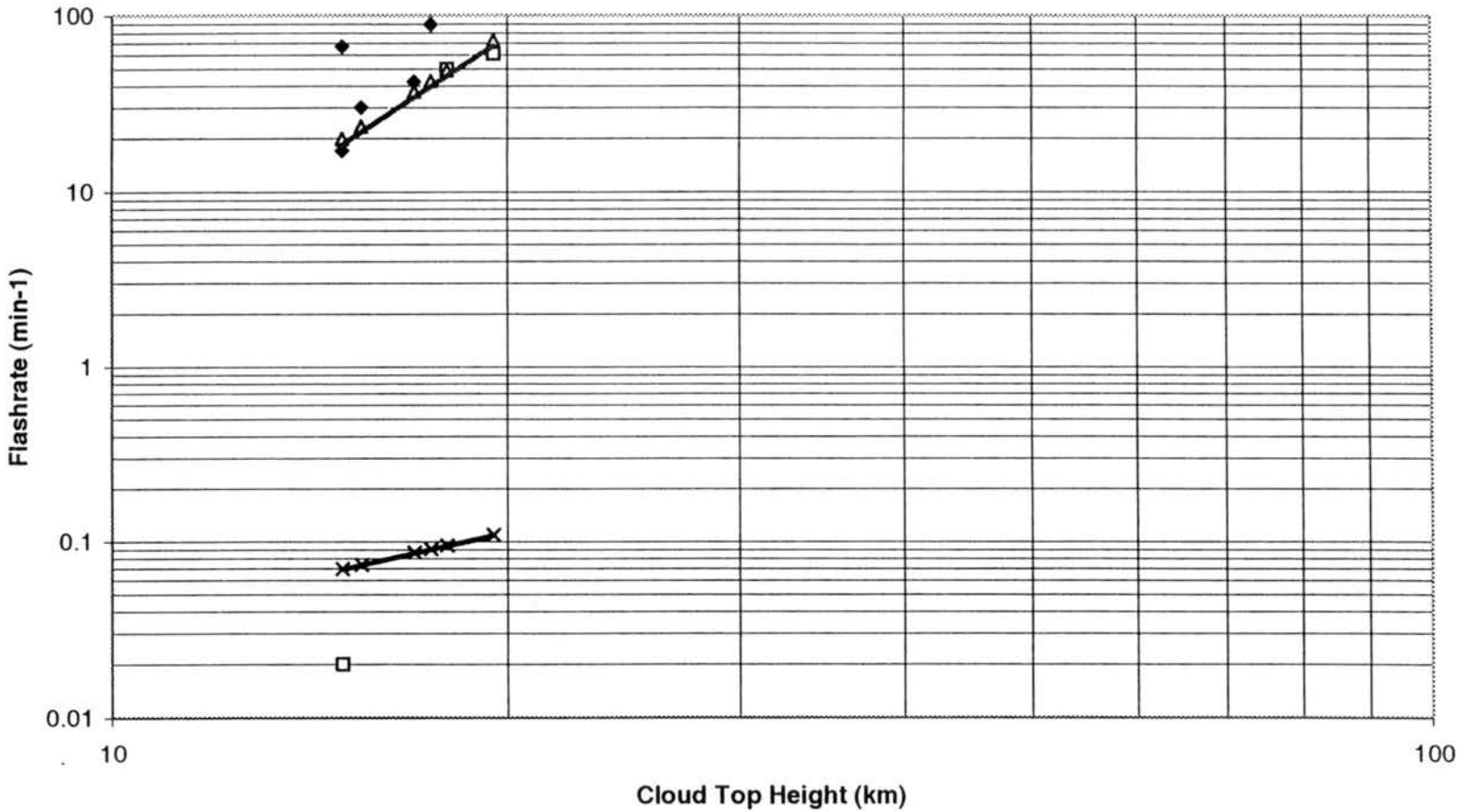

Figure 5.4 Cloud top height (derived via 0 dBZ radar peak height) on ordinate, log scale. Total flash rate on abscissa, log scale.

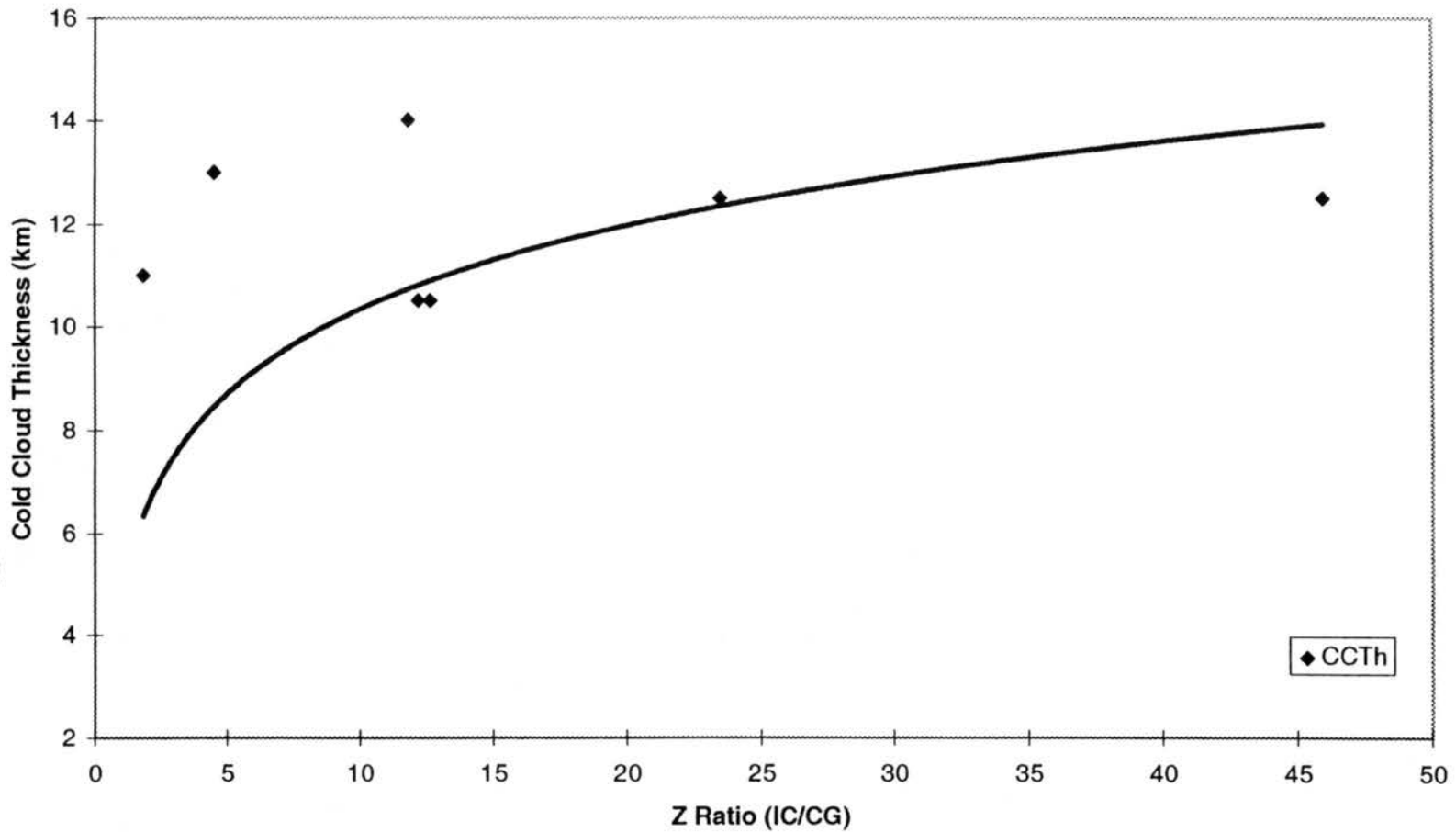

Figure 5.5 Cold cloud thickness (distance between cloud top and 0°C level) on ordinate. Z ratio (ratio of total number of IC flashes to CG flashes) on abscissa. PR93 parameterization is shown as black line.

REFERENCES

Buechler, D. E., P. D. Wright, and S. J. Goodman, 1990: Lightning/Rainfall relationships during COHMEX. Preprints. *J. Rech. Atmos.*, **16**, 295-320.

Oye, R., and R. E. Carbone, 1981: Interactive Doppler editing software. *Preprints, 20th Conf. Radar Meteor.*, Boston, Massachusetts, Amer. Meteorol. Soc., 683-689.

Carey, L. D., and S. A. Rutledge, 1996: A multiparameter radar case study of the microphysical an kinematic evolution of a lightning producing storm. Meteorol. Atmos. Phys., 59, 33-64.

Carey, L. D. and S. A. Rutledge, 1998: Electrical and multiparameter radar observations of a severe hailstorm. *J. Geophys. Res.*, **103**, 13979-14000.

Cressman, G. P., 1959: An operational objective analysis system. *Mon. Wea. Rev.*, **87**, 367-374.

Crook, N.A., T.L. Clark, and M.W. Moncrieff, 1990: The Denver Cyclone. Part I: Generation in low Froude number flow. *J. Atmos. Sci.*, **47**, 2725-2742.

Crook, N.A., T.L. Clark, and M.W. Moncrieff, 1991: The Denver Cyclone. Part I: Interaction with the convective boundary layer. *J. Atmos. Sci.*, **48**, 2109-2126.

Cummins, K. L., M. J. Murphy, E. A. Bardo, W. L. Hiscox, R. B. Pyle, and A. E. Pifer, 1998: A combined TOA/MDF technology upgrade of the U.S. National Lightning Detection Network. *J. Geophys. Res.*,**103**, 9035-9044.

Doviak, R.J, and D.S. Zrnic, 1993: Doppler radar and weather observations. Academic Press Inc., 562 pp. 562.

Ferrier, B. S., 1994: A double moment multiple phase four-class bulk ice scheme. Part 1: Description. *J. Atmos. Sci.*, **51**, 249-280.

Ferrier, B. S., W.-K. Tao, and J. Simpson, 1995: A double-moment multiple-phase four-class bulk ice scheme. Part II: Simulations of convective storms in different large-scale environments and comparisons with other bulk parameterizations. *Mon. Wea. Rev.*, **52**, 1001-1033.

Flatøy, F., and Ø. Hov, 1997: NO_x from lighting and the calculated chemical composition of the free troposphere. *J. Geophys. Res.*, **102**, 21373-21381.

Helsdon, J. H., Jr., G. Wu and R. D. Farley, 1992: An intracloud lightning parameterization scheme for storm electrifcation model. *J. Geophys. Res.*, **97**, 5865-5884.

Hubbert, J., V. Chandrasekar, V.N. Bringi, and P. Meischner, 1993: Processing and interpretationof coherent dual-polarized radar measurements. *J. Atmos. Oceanic Technol.*, **10**, 155-164.

Kasibhatla, P. S., H. Levy, II, and W. J. Moxim, 1993: Global NO_x, HNO_3, PAN, and NO_y distributions from fossil fuel combustion emissions: a model study, *J. Geophys. Res.*, **98**, 7165-?.

Kawakami, S., Y. Kondo, M Koike, H. Nakajima, G. L. Gregory, G. W. Sachse, R. E. Newell, E. V. Browell, D. R. Blake, J. M. Rodrigues, and J. T. Merril, 1997: Impact of lightning and convection on reactive nitrogen in the tropical free troposphere. *J. Geophys. Res.*, **102**, 28367-28384.

Keenan, T., R. Carbone, S. Rutledge, J. Wilson, G. Holland, and P. May, 1996: The Maritime Continent Thunderstorm Experiment (MCTEX): Overview and initial results. Preprints, Seventh Conference on Mesoscale Processes, 9-13 September, Reading, UK.

Keenan, T., K. Glasson, and F. Cummings, 1998: The BMRC/NCAR C-Band Polarimetric (C-POL) Radar System. *J. Atmos. Oceanic Technol.*, **15**, 871-886.

Lang, T., 1997: Relationship between storm structure and lightning activity in Colorado convection observed during STERAO-A. Master's Thesis, Colorado State University, Fort Collins, Colorado, pp. 167.

Laroche, P., A. Bondiou, P. Blanchet, J. Pigere, M. Weber, and B. Boldi,1994: 3D mapping of lightning discharge within storms. *International Aerospace and Ground Conf. On Lightning and Static Electricity*, Mannheim, Germany.

Lawrence, M. G., W. L. Chameides, P. S. Kasibhatla, H. Levy, II, and W. Moxim, 1995: Lightning and Atmospheric Chemistry: The rate of atmospheric NO production, in *Handbook of Atmospheric Electrodynamics*, vol. 1, edited by H. Volland, pp. 189-202, CRC Press, Boca Raton, Fla.

Levy, II, H., and W. J. Moxim, 1996: A global three-dimensional time-dependent lighting source of tropospheric NO_x. *J. Geophys. Res.*, **101**, 22911-22922.

Logan, J. A., 1983: Nitrogen oxides in the troposphere: global and regional budgets. *J. Geophys. Res.*, **88**, 10,785-10,807.

Marshall, J. S., and S. Radhakant, 1978: Radar precipitation maps as lightning indicators. *J. App. Met.*, **17**, 206-212.

Mazur, V., E. Williams, R. Boldi, L. Maier, and D.E. Proctor, 1997: Initial comparison of lightning mapping with operational time-of-arrival and interferometric systems. *J. Geophys. Res.*, **102**, 11071-11085.

Molinié, J., and C. A. Pontikis, 1995: A climatological study of tropical thunderstorm clouds and lightning frequencies on the French Guyana coast. *Geophys. Res. Lett.*, **22**, 1085-1088.

Orville, R. E., and D. W. Spencer, 1979: Global lightning flash frequency. *Mon. Wea. Rev.*, **107**, 934-943.

Penner, J. E., C. S. Atherton, J. Dignon, S. J. Ghan, J. J. Walton, and S. Hameed, 1991: Tropospheric nitrogen: a three-dimensional study of sources, distributions, and deposition. *J. Geophys. Res.*,**96**, 959-990.

Peterson, W.A., S. A. Rutledge, and R. E. Orville, 1996: Cloud-to-ground lightning observations from TOGA/COARE: selected results and lightning location algorithms. *Mon. Wea. Rev.*, **124**, 602-620.

Petersen, W. A., and S. A. Rutledge, 1998: On the relationship between cloud-to-ground lightning and convective rainfall. *J. Geophys. Res.*, **103**, 14025-14040.

Pickering, K. E., Y. Wang, W. Tao, and C. Price, 1998: Vertical distributions of lightning NO_x for use in regional and global chemical transport models. Submitted to *J. Geophys. Res.*

Pierce, E. T., 1970: Latitudinal variation of lightning parameters. *J. Appl. Meteorol.*, **9**, 194-195.

Prentice, S. A., and D. Mackerras, 1977: The ratio of cloud to cloud-ground lightning flashes in thunderstorms. *J. Appl. Meteorol.*, **16**, 545-550.

Price, C., and D. Rind, 1992: A simple lightning parameterization for calculating global lightning distributions. *J. Geophys. Res.*, **97**, 9919-9933.

Price, C., and D. Rind, 1993: What determines the cloud-to-ground lightning fraction in thunderstorms? *Geophys. Res. Lett.*, **20**, 463-466.

Price, C., and D. Rind, 1994: Modeling global lightning distributions in a general circulation model. *Mon. Wea. Rev.*, **122**, 1930-1939.

Price, C., and J. Penner, 1997a: NO_x from lightning 1. Global distribution based on lightning physics. *J. Geophys. Res.*,**102**, 5929-5941.

Price, C., and J. Penner, 1997b: NO_x from lightning 2. Constraints from the global atmospheric electric circuit. *J. Geophys. Res.*,**102**, 5943-5951.

Richard, P., 1996: Severe thunderstorm nowcasting: example of tornadic storm observed with a total lightning detection system. *Proceedings of the WMO Technical Conference on Tropical Aeronautical Meterology*, Geneva, Switzerland.

Ridley, B. A., J. E. Dye, J. G. Walega, J. Zheng, F. E. Grahek, and W. Rison, 1996: On the production for active nitrogen by thunderstorms over New Mexico. *J. Geophys. Res.*,**101**, 20985-21005.

Ryzhkov, A., and D.S. Zrnic, 1995: Precipitation and attenuation measurements at a 10-cm wavelength. *J. Appl. Meteor.*, **34**, 2121-2134.

Sinha, A., and R. Toumi, 1997: Tropospheric ozone, lightning, and climate change. *J. Geophys. Res.*, **102**, 10667-10672.

Solomon, R., and M. Baker, 1998: Lightning flash rate and type in convective storms. *J. Geophys. Res.*, **103**, 14041-14057.

Taylor, W. L., 1985: Lightning activity and severe storm structure. *Geophys. Res. Lett.*, **11**, 545-548.

Tuck, A. F., 1976: Production of nitrogen oxides by lightning discharges. *Quart. J. R. Met. Soc.*,**102**, 749-755.

Uman, M. A., 1987: *the lightning discharge*. Academic Press Inc., 377pp.

Weisman, and J. Klemp, 1986: Structure and classification of numerically simulated convective storms in directionally varying wind shears. *Mon. Wea. Rev.*, **112**, 2479-2498.

Williams, E. R., 1985: Large-scale charge separation in thunderclouds. *J. Geophys. Res.*, **90**, 6013-6025.

Wang, Y., A. W. DeSilva, and G. C. Goldenbaum, 1998: Nitric oxide production by simulated lightning: dependence on current, energy, and pressure. *J. Geophys. Res.*,**103**, 19149-19159.